Proton emission imaging of the nuclear burn in inertial confinement fusion experiments

by

Joseph Loreto DeCiantis

B.A. Physics
State University of New York at Geneseo, 2002

Submitted to the Department of Nuclear Science and Engineering
In Partial Fulfillment of the Requirements for the Degree of

MASTER OF SCIENCE IN NUCLEAR SCIENCE AND ENGINEERING
AT THE
MASSACHUSETTS INSTITUTE OF TECHNOLOGY

JUNE 2005

Signature of Author: _____
Department of Nuclear Science and Engineering
April 1, 2005

Approved by: _____
Richard D. Petrasso
Senior Research Scientist, Plasma Science and Fusion Center
Thesis Supervisor

Approved by: _____
Ronald R. Parker
Professor of Nuclear Science and Engineering
Thesis Reader

Approved by: _____
Jeffrey A. Coderre
Associate Professor of Nuclear Science and Engineering
Chairman, Departmental Committee on Graduate Students

Proton emission imaging of the nuclear burn in inertial confinement fusion experiments

by

Joseph Loreto DeCiantis

Submitted to the Department of Nuclear Science and Engineering on April 01, 2005
In Partial Fulfillment of the Requirements for the Degree of Master of Science in Nuclear Science and Engineering

Abstract

A proton core imaging system has been developed and extensively used for measuring the nuclear burn regions of inertial confinement fusion implosions. These imaging cameras, mounted to the 60-beam OMEGA laser facility, use the penetrating 14.7-MeV protons produced from the fusion of deuterium and 3-helium to obtain spatial images of the nuclear burn. The technique relies on penumbral imaging, with symmetric or asymmetric reconstruction algorithms used to extract the source distribution. The hardware and design considerations required for the imaging cameras are described and the fidelity of the reconstructed burn profiles is verified. The spatial characteristics of the nuclear burn profile of directly driven capsule implosions were, for the first time, extensively studied. For thick plastic-shell capsules, with initial radii of ~ 430 μm, the characteristic burn radii were found to be ~ 30 μm. The effects of gas pressure, shell thickness, laser energy, laser smoothing, capsule size, and capsule composition on the burn radius were systematically examined, resulting in radii ranging from 20 μm to 80 μm. This new set of absolute burn profile measurements, in combination with other important implosion diagnostics, constitute a significant advance in that it imposes an exacting, integral test of the complex dynamics of imploding capsules.

Thesis Supervisor: Richard D. Petrasso
Title: Senior Research Scientist, Plasma Science and Fusion Center
Visiting Senior Scientist, Laboratory for Laser Energetics

Thesis Supervisor: Ronald R. Parker
Title: Professor of Nuclear Science and Engineering

Acknowledgments

I am greatly indebted to those around me, both here at MIT and at the University of Rochester. This work was made possible through their continued support and guidance. I am especially indebted to my research supervisor Richard Petrasso for giving me the opportunity to work in the High Energy Density Physics group. Throughout my stay here, he has supplied me with a wealth of insightful advise, encouragement, and direction; none of this research would have been possible without him. His great enthusiasm and ambition serve as a model for the rest of us. I am also grateful to the other scientists in the High Energy Density Physics group; they have all contributed greatly to my education. Throughout this research I have worked closely with Fredrick Séguin, whose constant guidance and input helped bring this project to completion. Hopefully, his rigorous approach to research has rubbed off on me! Thanks also to Johan Frenje for always keeping his door open and for his continued words of encouragement. I could always count on you to share a pot of coffee. Thanks also to Chikang Li, whose insightful questions and comments helped keep this project on track, and whose healthy appetite made our BBQs a success.

My gratitude also goes out to my peers and coworkers. You have all had positive impacts on my research, and have made my stay here enjoyable. Ryan, you were always there to answer questions and to help put together pieces of the puzzle. Mike, you always found time to help as I worked through problems on the board. Jocelyn, thanks for all your help with etching, scanning, and various administrative issues. Thanks also to Cliff, Magnus, Shinya, Brook, and Vincent. You all have had a positive influence on my stay at MIT.

I am grateful for assistance provided by the scientists and personnel at the Laboratory for Laser Energetics (LLE) located as the University of Rochester. Samuel Roberts and Candice Culligan were both instrumental in preparing for the experiments at LLE. Jacques Delettrez was kind enough to supply us with one-dimensional implosion simulations. Vladimir Smalyuk supplied the invaluable x-ray framing camera data, which Sean Regan assisted in analyzing. Additional conversations with Jim Knauer, Frederic Marshall, David Meyerhofer, and Craig Sangster have not gone overlooked! I appreciate all your time and help.

Finally, I would like to thank my family for their continued support. In particular, I cannot begin to express how indebted I am to my fiancée Amy; she is the brilliant light that makes my world shine! She has shown nothing but continued support and patience throughout our time apart. And of course, I owe everything to my parents, who put me here, and almost as much my brothers, who have served as great role models. My Boston friends also require praise, for they provided the outlet with which I could unwind. I owe Noah and Mic special thanks for dragging me from the office when I was obviously overworked. Thanks also to my climbing buddy, Matt, first for not dropping me, and second for all the adventures we've been through. The old Geneseo crew, both in Boston and elsewhere, has kept my spirits high for the past seven years.

Table of Contents

List of Figures

1. Introduction

Fusion occurs when two light nuclei, such as hydrogen and 3-helium, fuse together to form a heavier nucleus. Since the resultant nucleus contains about 0.4% less mass than the constituent nuclei, substantial energy is released. As is also well known, fusion is the process that powers the sun and the stars, and it is a potentially attractive source of power for meeting future energy demands: an essentially limitless supply of fuel can be extracted from the ocean, and harmful effects to the environment can in principle be minimized. Extensive research over past decades, in both magnetic and inertial confinement fusion (MCF and ICF), has been devoted to investigate the physics of fusion; the work presented here is concerned with research in ICF.[1,2]

In direct-drive ICF, a spherical capsule containing fuel is compressed and heated by direct illumination of laser beams focused on the capsule surface in a nominally uniform fashion. Due to the high deuterium-tritium (D-T) fusion cross section, a mixture D and T is the fuel of choice for ignition experiments and, eventually, for a first generation reactor. However, for diagnostic reasons and for ease of handling, hydro-equivalent surrogate fuels of D_2 or D^3He are often used in exploring implosion dynamics. The work presented here concentrates on capsules filled with deuterium and 3-helium (^{3}He) fuel.

The plasma processes and instabilities in ICF implosions have been studied and simulated for decades, but many issues remain. To that end, and to examine the integral effect of all implosion processes, such as drive efficiency, mix, and radiation and electron transport, we have developed a proton core imaging system (PCIS) to measure the spatial profile of the nuclear burn. Surface brightness images of the nuclear burn and radial burn

profiles (reactions per unit volume versus radius) for nominally symmetric implosions are obtained.

The work contained herein includes design and implementation of the hardware, verification of the fidelity of the reconstructed burn profiles, and, for a variety of implosion conditions, the first ever systematic examination of nuclear burn profiles. Instrumentation and reconstruction fidelity are described in Section 2, entitled "Proton core imaging of the nuclear burn in inertial confinement fusion implosions" (submitted to Review of Scientific Instruments).[3] Examination of the nuclear burn profile dependence on capsule and drive conditions is described in Section 3, entitled "Dependence of burn profiles on implosion conditions in inertial confinement fusion experiments" (submitted to Physics of Plasmas).[4] These latter studies examine the effects of ion temperature, radial convergence, and fuel-shell mix on the D^3He burn profiles.

As the work presented here uses several types of capsules, Fig. 1 illustrates two generic and frequently used capsules: thick-plastic shell and thin-glass shell capsules. Much additional information, intended to compliment the two papers, has been included as appendices. In addition, Appendix D contains suggestions for future experiments.

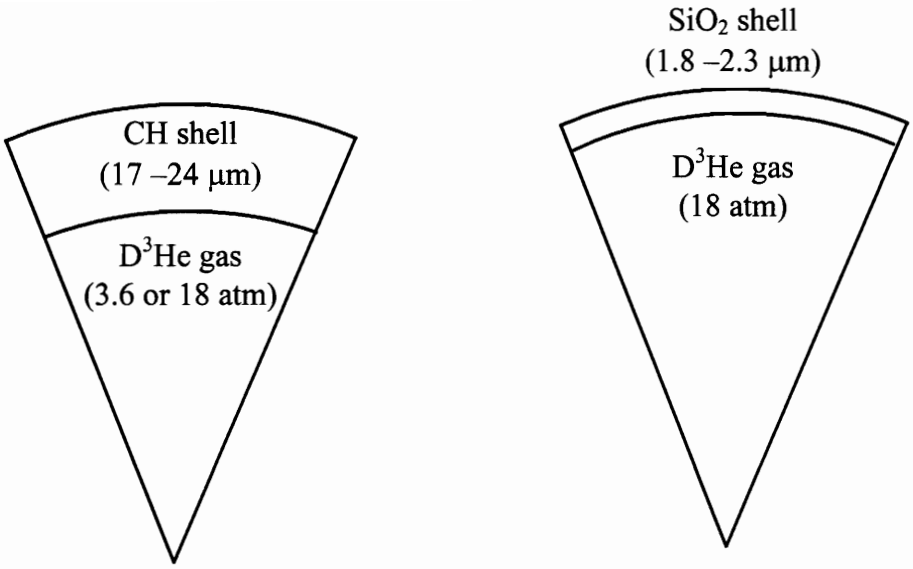

Figure 1 Thick plastic and thin glass capsules

FIG. 1. Both thick plastic (CH) shell and thin glass (SiO_2) shell capsules were used to study the size of the nuclear burn region. The capsules were either ~ 430 μm or 470 μm in radius and were typically filled with D^3He gas.

2. Proton core imaging of the nuclear burn in inertial confinement fusion implosions

J. L. DeCiantis, F. H. Séguin, J. A. Frenje, V. Berube, M. J. Canavan, C. D. Chen, S. Kurebayashi, C. K. Li, J. R. Rygg, B. E. Schwartz, R. D. Petrasso[a)]
Plasma Science and Fusion Center, Massachusetts Institute of Technology, Cambridge, Massachusetts, 02139

J. A. Delettrez, S. P. Regan, V. A. Smalyuk, J. P. Knauer, F. J. Marshall, D. D. Meyerhofer[b)], S. Roberts, T. C. Sangster, C. Stoeckl
Laboratory for Laser Energetics, University of Rochester, Rochester, New York, 14623

K. Mikaelian, H. S. Park, H. F. Robey
Lawrence Livermore National Laboratory, Livermore, California 94550

A proton core imaging system has been developed and extensively used for measuring the nuclear burn regions of inertial confinement fusion implosions. These imaging cameras, mounted to the 60-beam OMEGA laser facility, use the penetrating 14.7-MeV protons produced from D^3He fusion reactions to obtain spatial images of the nuclear burn. The spatial burn information is combined with temporal and spectral measurements of the D^3He burn to provide additional information about the implosions. The imaging technique relies on penumbral imaging with symmetric or asymmetric reconstruction algorithms used to extract the source distribution. The hardware and design considerations required for the imaging cameras are described. Experimental data and results are presented for a representative 20-μm thick plastic shell implosion with 18-atm of D^3He gas, for which the burn-weighted areal density was 62 ± 8 mg/cm^2. The burn profile (reactions per unit volume versus radius) was well fit by a Gaussian with an e folding of 31 ± 2.5 μm. For a variety of other implosions, burn radii ranged between 20 and 80 μm. To verify the fidelity of the reconstructed images, burn images from several implosions, along with calculations and simulations, were utilized.

a) Also Visiting Senior Scientist, Laboratory for Laser Energetics, University of Rochester.
b) Also Departments of Mechanical Engineering, Physics and Astronomy.

I. Introduction

The complex dynamics of imploding capsules, including such effects as mix, drive asymmetry, and radiation and electron transport, can be understood using images of nuclear burn. These images reflect the cumulative effects of the entire implosion process. This work discusses the technology and design for imaging the nuclear burn using the energetic (14.7 MeV) protons generated in inertial confinement fusion (ICF)[1,2] implosions. Burn images using neutron-emissions have been previously obtained from deuterium-tritium capsules for a limited number of implosions;[3-6] in addition, others have obtained images using 3-MeV protons[7-9] and 3.5-MeV alpha particles,[9] but only for a small number of thin-shell exploding-pusher type capsules. This article discusses the technology and hardware used to image the energetic 14.7-MeV proton emission from a variety of implosions. The energetic D^3He protons were generated by fusion of deuterium (D) and 3-helium (^3He) fuel ions. This technique allows us to obtain images from thick plastic-shell capsule implosion, through which less energetic charged particles would be ranged out. The proton-emission imaging cameras generate penumbral images[10] of the burn region, which are then deconvolved to obtain source information. Deconvolution is accomplished with a non-iterative technique using computation in the spatial domain, which has been extensively tested with simulated data generated by both Monte Carlo and analytic programs.[11]

The reconstruction procedure includes two separate algorithms for extracting burn information from the penumbral images. The first generates a two dimensional (2-D) surface-brightness image of the burn. In this manner, 2-D images have been used to

examine burn asymmetries resulting from imposed drive asymmetries.[12] The second algorithm generates a radial burn profile (reactions per unit volume) for nominally symmetric implosions. The work described here uses only the second technique; the burn profile that best describes the penumbral data is determined by allowing the profile shape to vary continuously between a hollow to a peaked Gaussian distribution while the radius is simultaneously adjusted.[11] In this manner, systematic studies involving a large number of implosions have been carried out to determine the effect of capsule and drive conditions on the burn profiles.[13] These studies are reported elsewhere.[13,14]

The structure of the paper is as follows: Sec. II describes the camera hardware, which consists primarily of an imaging aperture that is significantly larger than the source, and a detector pack comprised of several ranging filters and solid-state CR-39 charged-particle detectors. Sec. III presents raw experimental data obtained from an implosion, along with the corresponding deconvolved source emissivity. Sec. IV carefully evaluates the four most probable sources of image degradation, all of which are shown to be negligible. Sec. V discusses several compelling experimental demonstrations of the fidelity of the reconstructed images. Sec. VI summarizes the main results.

II. Hardware and design features

The proton core imaging system (PCIS) cameras have been designed and three independent cameras have been for orthogonal imaging. The principal design features are outlined here and then discussed in detail. Flexibility in magnification and filter assignments allows for imaging various implosion types. A dual detection scheme has

been implemented and proven valuable for verifying results and protecting against defective or damaged detectors. A modularized design minimizes the turn-around time between successive experiments. The integrated system has proven very effective and practical for obtaining burn images at the OMEGA laser facility.[15]

Three identical imaging cameras have been built, allowing for orthogonal imaging of D^3He-gas filled capsule implosions, an essential feature for studying the burn asymmetry (see Sec. V). Figure 1 shows a schematic of three proton-emission imaging cameras mounted on the OMEGA target chamber. Each camera is positioned within the OMEGA target chamber by a special diagnostic shuttle system. An isolated camera is shown in Fig. 2a. The fundamental camera hardware, consisting of an aperture and a single detector pack, has been emphasized (Fig 2a and b).

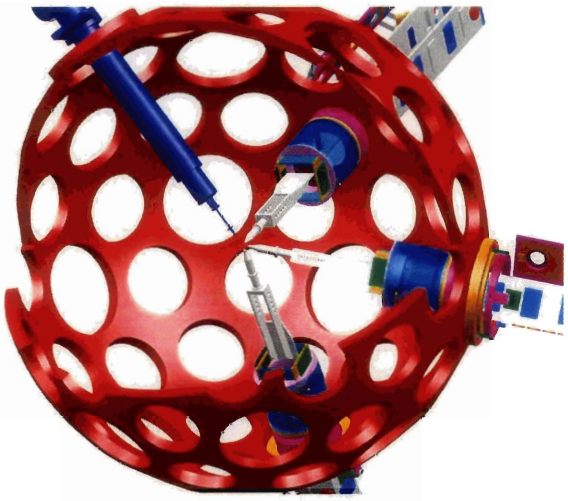

Figure 1 Three proton-emission imaging cameras mounted to the OMEGA chamber

FIG. 1. Schematic of the OMEGA target chamber with three cameras for imaging a capsule implosion. The capsule is positioned using the target positioning system located at 11 o'clock. The surrounding three structures (1, 4, and 5 o'clock) are the PCIS cameras, located approximately orthogonal to each other, a feature, discussed in the text, that is especially important for probing burn asymmetries and for establishing measurement accuracy.

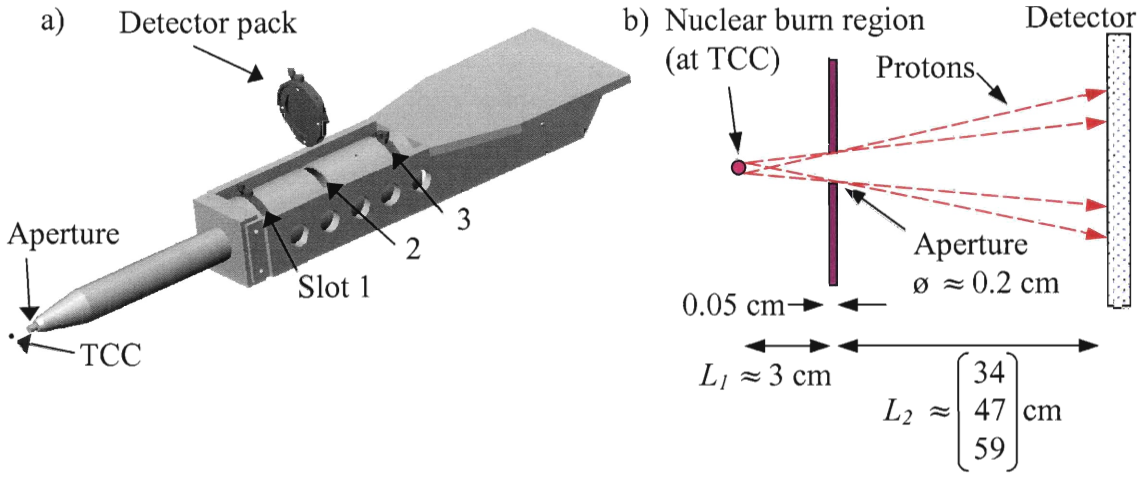

Figure 2 Schematics of the imaging camera

FIG. 2. (a) Illustration of the proton-emission imaging hardware. The capsule implosion is located at target chamber center (TCC), which is about 3 cm from the imaging aperture. A detector pack may be positioned in one of three available slots, providing a maximum geometric magnification (M) of 12.5x, 16x, or 20x with corresponding distances from the aperture of about 34, 47, and 59 cm. The aperture consists of a 0.2-cm hole in a 500-μm thick tantalum substrate. The total length of the instrument is 93 cm. (b) A line diagram clearly illustrates the dimensions, where M $\equiv L_2/L_1$.

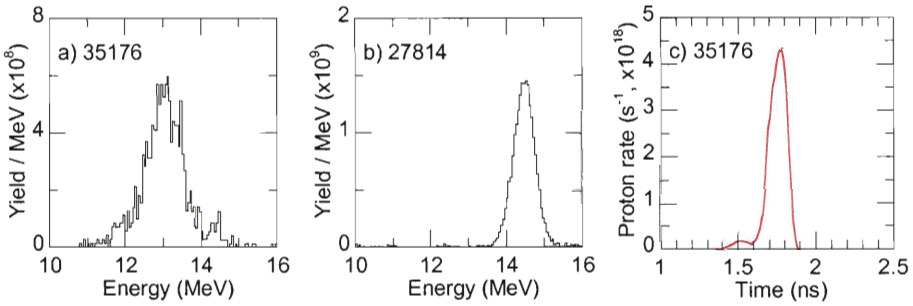

Figure 3 Representative proton spectra and temporal history

FIG. 3 For proton-emission imaging, filters are selected to properly reduce the incident proton energies down to an optimal detection efficiency range. For different implosion types, filter assignments must accommodate various proton spectra, as illustrated by the measured D^3He proton spectra obtained from implosions involving (a) a 20-μm thick CH capsule (shot 35176), and (b) a 2.3-μm glass capsule (shot 27814). (c) The corresponding D^3He burn history obtained from the proton temporal diagnostic for shot 35176 illustrates the shock-driven burn (~ 1.55 ns), and compression burn (~ 1.88 ns).

To maximize counting statistics, the aperture is usually positioned as close as possible to the implosion, located at target chamber center (TCC), as space limitations permit (~ 3 cm). The aperture is typically a 500 or 2000-μm diameter hole machined into a 500-μm thick tantalum (Ta) substrate. An accurate, clean, and burr-free edge for the aperture wall is obtained using electro-discharge machining. Prior to use, the aperture diameter is characterized to ± 2 μm using a microscope and a calibrated stepper motor. Measurements are taken along four separate axes, each separated by 45 degrees, to test eccentricity, and then on both sides to test for symmetry (the effect of tapered apertures will be discussed in Sec. IV).

The detector pack consists of a layered assembly of CR-39 detectors[16] and metallic foils held in an Aluminum (Al) support. The CR-39 detectors provide efficient and accurate detection of incident protons; when slowed down to a range between 0.5 and 8 MeV, the proton detection efficiency is essentially 100%[16] and the position of each incident proton is recorded with an accuracy of about 0.2 μm.[16] For imaging asymmetrically driven implosions,[12] the detector orientation is defined by a dowel pin.

The metallic foils act as ranging filters that are designed to reduce the energy of incoming energetic protons to the ~ 100% detection efficiency range. Representative D^3He proton spectra from two very different capsule implosions are shown in Fig. 3a (a 20-μm thick plastic-shell capsule) and 3b (2-μm glass-shell capsule). The corresponding mean proton energies were quite different, 13 MeV from the plastic-shell implosion and 14.5 MeV from the glass-shell implosion, and must be accounted for in the filtering assignments. For example, the plastic-shell implosion might be imaged using a single 800-μm thick Al filter, while a 1000-μm filter might be used for the glass-shell

implosion. However, rather than use a single filter to obtain a burn image, a series of filters and sheets of CR-39 are stacked to obtain multiple images from a single camera.

Front-back imaging of D^3He protons is obtained with a single camera when proper ranging filters are selected. As illustrated in Fig. 4a, two images of the D^3He burn are obtained when a thick filter is placed in front of two back-to-back sheets of CR-39. The filter and first sheet of CR-39 range down the energetic D^3He protons for optimal detection on the back of the first sheet (grey arrows) and again on the front of the second sheet of CR-39 (solid arrows). This front-back imaging approach provides an independent validation of the reconstruction algorithm, and protects against damaged CR-39 and CR-39 with anomalous intrinsic noise.[14]

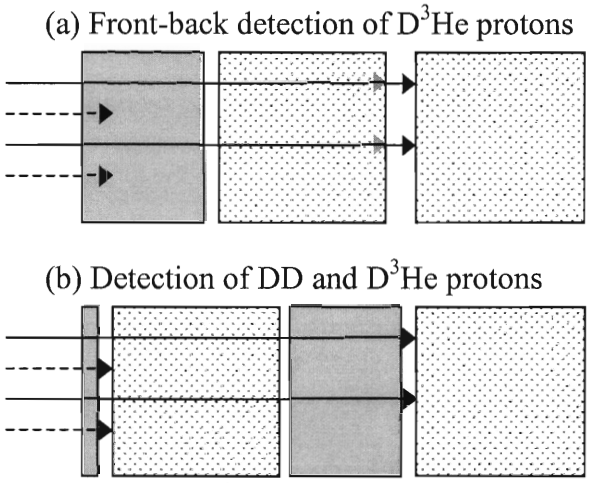

Figure 4 Illustration of camera filter assignments

FIG. 4. Illustration of filter assignments used to obtain two burn images with a single camera. (a) Front-back detection of D^3He protons (represented by solid lines) is obtained when a thick filter (~ 200-μm Al) is placed in front of two sheets of CR-39 detectors, ranging the energetic protons for optimal detection on the back of the first sheet, and front of the second sheet. This technique has proven extremely useful for validating the reconstruction algorithm, as well as protecting against defective CR-39. (b) An image of the D^3He burn, integrated over the entire burn, and an image of the DD burn, integrated only over the shock-burn (see Fig 3c), are simultaneously obtained when a thin filter (~ 20-μm Al) is placed in front while a thicker filter (~ 180-μm Al) is placed between the two detector sheets. The low energy, 3-MeV DD protons (dotted lines) are able to escape the capsule only at shock-bang time, and are discussed in Appendix B.

With an alternate filter assignment (Fig. 4b), an image of the DD shock burn and the D^3He burn, integrated over the entire implosion, may be obtained with a single camera (as seen in the D^3He burn history of Fig 3c, shock-bang corresponds to ~ 1.55 ns). If the first filter is sufficiently thin, the less energetic 3-MeV DD protons produced at shock-bang time are imaged on the first detector (at shock-bang time the areal density of the shell material is ~ 12 mg/cm^2, low enough to allow these particles to escape);[17,18] while the second filter is selected such that the energetic 14.7-MeV D^3He protons produced during the entire burn are imaged on the second detector.[14]

The CR-39 detectors begin to saturate if the incident proton density exceeds $7x10^5$ protons/cm^2. For this reason, the assembled detector pack may be positioned in one of three designated slots (shown in Fig. 2) allowing for increased dynamic range. The first slot provides a 12.5x geometric magnification (M), the second provides 16x, and the third provides 20x, providing efficient detection of protons for D^3He yields up to $3x10^{10}$.

Once past the aperture, the signal protons are enclosed within a conductive housing (Fig. 2). This enclosure prevents stray charged particles from reaching the detectors and shields signal protons from possible electric and magnetic fields. The front end of the camera housing is designed to allow the aperture to be inserted as close to the implosion as space limitations permit (~ 3 cm), maximizing the signal statistics available for burn image reconstructions.

The large, flat structure at the back end of the system (Fig. 2) secures the camera to the Ten-Inch Manipulators (TIMs) on the OMEGA target chamber. The TIMs are diagnostic shuttle systems used to position diagnostics near the implosion. There are six TIMs on the OMEGA target chamber, allowing for the use of multiple PCIS cameras.

The TIMs facilitate the installation, access, and removal of the cameras. Ease of access is essential since the aperture and detector pack of each camera must be replaced between every laser shot. Modularized aperture and detector packs have been implemented to ensure that the replacement time does not exceed the typical shot-to-shot time interval of the OMEGA laser.

III. A representative 20-μm plastic-shell implosion

The proton-emission imaging cameras have been used to examine many implosions at the OMEGA laser system; the majority of these involved direct illumination of warm plastic-shell capsules filled with a D^3He gas mixture. These capsules were usually driven by 60 beams of frequency tripled (0.35 μm) UV light, with a total laser energy of 23 kJ delivered in a 1-ns square pulse.[19] Individual beams underwent 1.0-THz 2-D smoothing by spectral dispersion and polarization smoothing applied through the use of birefringent wedges.[20]

Of the many thick-shell implosions that have been imaged, Fig. 5a shows a typical raw penumbral image from implosion 35176, (18-atm D^3He-gas filled capsule with a 20-μm thick plastic shell). The brightness of the image represents the number density of D^3He protons striking the CR-39 detector. From the center of an image, the absolute yields are calculated using the detected proton density. These yields are typically in agreement with yields obtained by the proton spectrometers.[16,21] A contour plot of the proton density is shown in Fig. 5b, where image smoothing has been implemented; the penumbral region is characterized by the steep gradient in proton density.

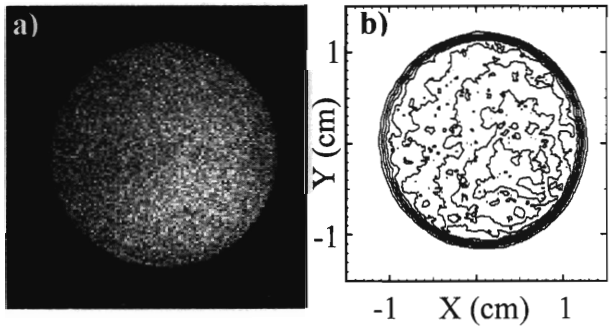

Figure 5 Encoded penumbral image and contour plot

FIG. 5. Raw, encoded image of the 14.7-MeV D^3He burn obtained with proton-emission imaging cameras for OMEGA laser shot 35176, where an 18-atm D^3He-gas-filled capsule with a 20-μm thick CH-shell was imploded. For this particular case, the imaging camera was mounted in TIM3. (a) Brightness of the raw image is proportional to the number of protons per unit area on the detector. (b) A contour plot of the data better illustrates the penumbral region, which contains the spatial information of the burn. The contour plot is smoothed to provide a clear illustration of the penumbra.

Structural information about the source is obtained by deconvolving the raw image using the method described in ref. 9, and the time-integrated radial burn profile (reactions per μm^3) of the implosion was determined. A few procedural steps involved in the data processing are outlined here. As illustrated in Fig. 6, from the azimuthally averaged proton density ($N(r)$) a radial derivative (dN/dr) is calculated. An azimuthally averaged radial derivative from implosion 35176 is shown in Fig. 7a. The solid line represents the best fit to the data with a reduced chi squared of 1.2. The fit corresponds to a D^3He burn profile with a Gaussian distribution

$$P_{burn}(r) = P_0 \exp\left[-(r / R_{burn})^2\right], \quad (1)$$

where r is the radius from the center of the implosion, P_0 is the proton emissivity per unit volume at $r = 0$, and R_{burn} is defined here as the burn radius. The R_{burn} for implosion 35176 is 31 μm. Figure 7a shows two additional fits to the raw data (dotted lines), each obtained by increasing the total chi squared by one. These alternative fits correspond to a

± 2.5 μm statistical uncertainty in the value of R_{burn}.[22] Figure 7b shows the radial burn profile that corresponds to the best fit (solid line) and the resulting error envelope (dotted lines).

The D^3He burn data from many nominally symmetric implosions were well characterized by Gaussian-shaped burn profiles. A range of R_{burn} from 20 – 80 μm has been measured,[13] the latter corresponding to an exploding pusher type capsule, demonstrating the applicability of this imaging technique to widely different implosion types.

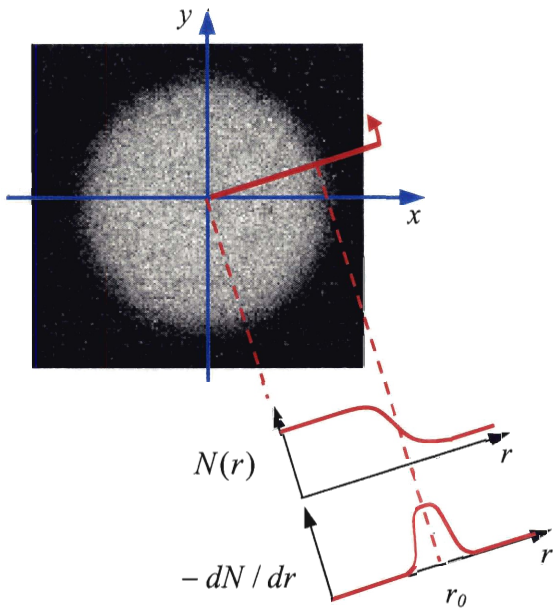

Figure 6 Obtaining N(r) and dN/dR from a penumbral image

Fig. 6. The azimuthal average of the number of proton tracks per unit area on the detector, *N(r)*, and the corresponding radial derivative, *dN/dr*.

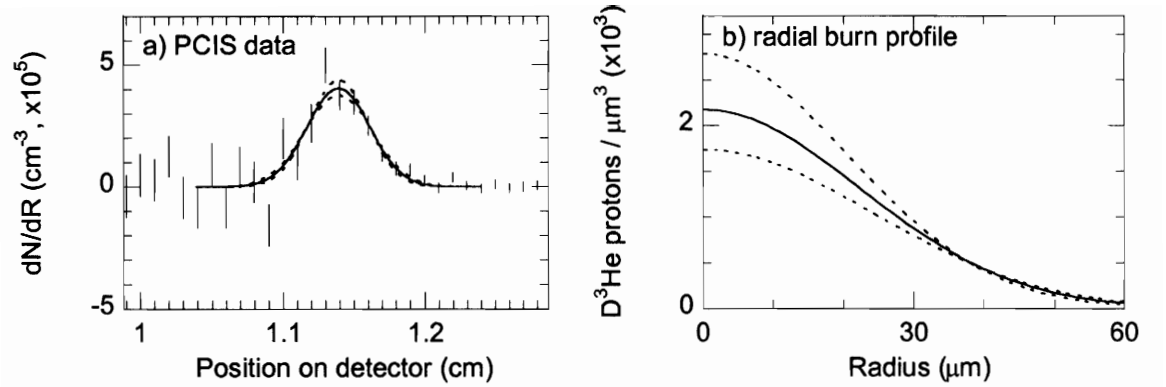

Figure 7 dN/dR and radial burn profile for shot 35176

FIG. 7. (a) Shown is the radial derivative of the azimuthally averaged detected proton density (dN/dr) as a function of detector radius. The data were obtained with one of three proton-emission imaging cameras from OMEGA laser shot 35176 (a 20-μm plastic-shell implosion with an 18-atm D^3He-gas fill). The statistical error bars are larger (smaller) towards the left (right) of the peak where dN/dr represents a small difference between two large (small) numbers. The solid line, representing the best fit to the data, corresponds to the (b) radial burn profile (D^3He reactions per unit volume). The burn image was best described by a Gaussian source distribution with $R_{burn} = 31$ μm. The total chi squared of the fit was increased by one, generating the error envelopes shown in (a) and (b) as dashed lines, and corresponding to statistical uncertainties of ± 2.5 μm. The best fit represents a reduced chi square of 1.24.

IV. Demonstration that possible sources of image broadening are unimportant

The following subsections describe four possible sources of image broadening that could compromise the fidelity of the reconstructed burn images. The protons, which are detected and used to generate the penumbral image, may experience trajectory shifts when traversing through electric and magnetic fields, and different materials. These materials include the capsule shell, the aperture substrate, and the ranging filters. If these trajectory shifts are severe enough, the resulting reconstructed image may be artificially broadened. To estimate the degree of image broadening, calculations and simulations were performed for four possible sources. The effect of each is assumed to be

independent of the others and all effects are added in quadrature. They are presented in order of occurrence, beginning from the location of D^3He proton production, and ending at the detector.

A. Scattering in the compressed capsule

The protons detected by the imaging cameras are likely to experience some scattering whenever matter is encountered. From the time of proton production to detection, there are three possible scattering sources. The first significant material encountered is the remnants of the shell that surround and compress the heated fuel region (see Fig. 8). Since the majority of implosions imaged with PCIS involved 20-μm thick CH-plastic shells, this type of capsule will be examined. At the time of peak proton production, the shell material remaining after the ablation phase consists of a highly dense (~ 20 g/cc), low temperature (~ 500 eV) plasma.[23,24] Spectral analysis of D^3He fusion protons has shown that the shell material, with a corresponding ρR of ~ 60 mg/cm^2, is responsible for a downshift of a couple MeV from the 14.7-MeV birth energy (Fig. 3a).[25,26] Although proton (or in general ion) slowing down is associated with drag of the background electrons, some small amount of scattering will occur off the ions. To estimate the amount of this scattering, and its effect on the broadening of the point response function (prf), two separate calculations were performed.

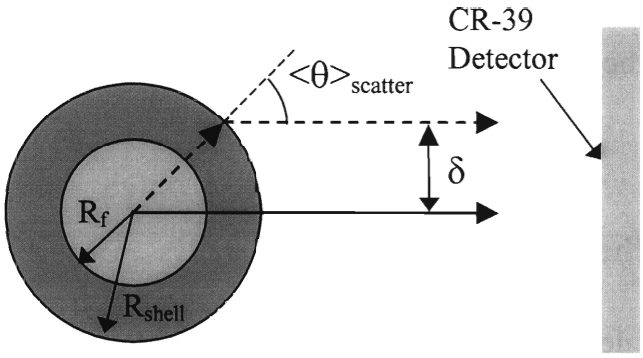

Figure 8 Proton scattering in the shell material

FIG. 8. Illustration of the assumed geometry for estimating the degree of proton scattering in shell material. The radius of the fuel region, Rf, was taken to be 45 μm; the outer radius of the shell, Rshell, was 80 μm. Two proton paths originating from a point source are illustrated. The solid line represents the path taken by unscattered protons; the dotted line represents the worst-case path of scattered protons. The average scattering angle, $\langle\theta\rangle_{scatter}$, was estimated for both cold material and a fully ionized CH plasma shell. The results were, respectively, ~ 1 and 2 degrees, producing a corresponding source broadening, δ of ~ 1 μm and 3 μm. Both are negligible compared to the typical measured burn radius of ~ 30 μm.

In the first calculation, the shell material was treated as a cold, dense solid. The Monte Carlo code TRIM[27] was used to simulate the slowing down and scatter of 14.7-MeV protons in the cold shell material. The shell was treated as a 50-50 atomic mixture of carbon and hydrogen with a density of 20 g/cc and a thickness of 35 μm (a ρR of 70 mg/cm^2). The calculated average transmitted energy was 12.2 MeV, in reasonable agreement with experimental observations (Fig. 3a). The average scattering angle was found to be 0.9 degrees. Assuming the fuel-shell interface is at a radius of 45 μm and all scattering occurs on the outside edge of the shell, a worst-case amount of source broadening was estimated to be ~ 1 μm (see Fig. 8). This is insignificant compared to an R_{burn} of 31 μm.

In the second, more realistic calculation, the compressed shell material was treated as hot plasma at a temperature of 500 eV.[23,24] At this temperature and density, the

shell atoms are fully ionized.[28] With minor modifications to Rutherford's scattering formula,[29] the mean squared angle of the scattered particles is given by

$$\left\langle \theta^2 \right\rangle \cong 2\pi N_i \left(\frac{2zeZe}{pv} \right)^2 (\ln \Lambda) \cdot t \tag{2}$$

where N_i is the ion species density in the background plasma, t is the shell thickness, and Ze is the charge of the scattering material; ze is the charge of the incident particle, with momentum p, and speed v; and ln Λ is the Coulomb logarithm. The mean scattered angle was calculated for 12-MeV protons passing through 35 μm of 500 eV, 20 g/cc CH plasma with a Coulomb logarithm of approximately 13.[23,24] (An initial energy of 12 MeV and a ρR of 70 mg/cm^2 were selected to over-estimate the effect.) The calculations gave an average scatter angle of ~ 2 degrees, broadening the prf by ~ 3 μm. (A similar calculation was performed for scattering in the fuel region, but the effect was much smaller.) A 3-μm broadening of the prf has negligible impact on the measured radius of a source with a 31 μm burn radius.[30]

B. Trajectory shifts due to electric fields

During the laser pulse of a direct drive implosion, hot electrons are blown off the capsule and may redeposit themselves on surrounding structures, temporarily establishing electric fields. The purpose of this section is to examine the effect a potential difference between the capsule and the aperture has on proton trajectories, and ultimately on the prf of the instrument. Although the effect is complicated by the structure of the OMEGA target chamber and the dynamics of the implosion, these calculations look at simplified geometries to produce an order of magnitude estimate of the effect.

A program was developed to track the trajectory of 14.7-MeV protons emitted from a point source, through a negatively charged aperture substrate, and to the CR-39 detector plane. A diagram of the geometry is shown in Fig. 9a. The aperture was positioned 3.3 cm from the source, and the detector plane was positioned an additional 33 cm past the aperture. The figure illustrates one possible effect of a charged aperture, where a proton path is indicated for two scenarios: for the case of a charged aperture (dashed line), and the case of an uncharged aperture (solid line).

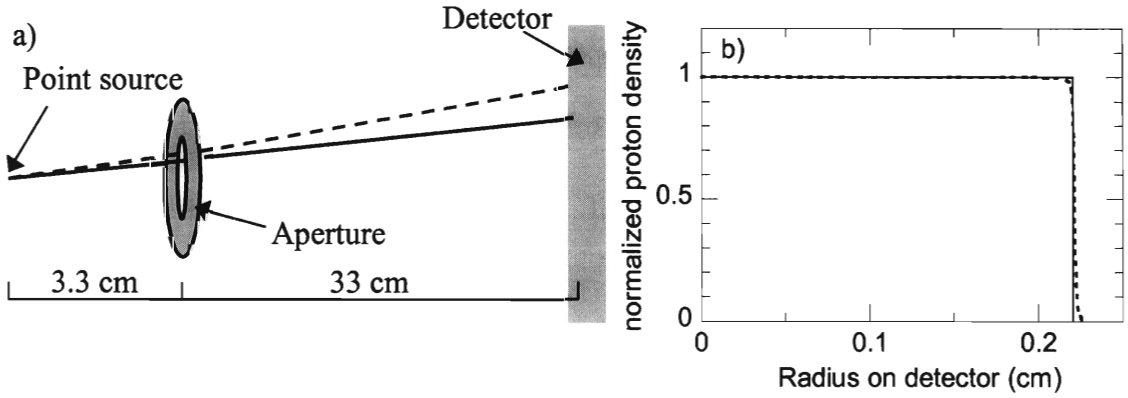

Figure 9 Proton trajectory shifts due to aperture charging

FIG. 9. (a) Illustration of the effect of electric fields on proton trajectory. The dashed line schematically represents the proton path when a 200 μm aperture carries a potential of 1 MV relative to the source (an over estimate of realistic conditions), while the solid line represents the proton path when no potential is present. Calculations were performed to estimate the image broadening of a point source. (b) The simulated proton density striking the detector for the case of no potential (solid line) and a 1-MV potential (dashed line) was determined. The result was a slight outward shift of the image, and a broadening of the point source by ~ 1 μm. This broadening is small compared to a typical burn radius of ~ 30 μm. [See Figure A1 for more a closer examination of the broadening of the prf.]

The aperture substrate was modeled by a one-cm radius disk carrying a uniform-negative charge such that the potential between the source and this disk was one megavolt. The magnitude of the potential was chosen to over-estimate the experimental conditions. Experiments indicate the capsule itself may carry a charge of approximately

a megavolt during the laser pulse, after the hot electrons are blown-off, but the potential quickly dissipates once the laser pulse is terminated.[31,32] For the PCIS experiments, the proton production occurs several hundred picoseconds after laser pulse is terminated, providing a significant period of time in which the potential is known to have rapidly decayed.

Calculations were performed for a 200-μm radius aperture located in the center of the 1-cm radius disk. Protons were launched through the aperture in all allowable directions. The code calculated particle forces and trajectories on a time scale corresponding to a 5-μm step in the linear dimension using a standard integration for the velocity and a 2nd order Runge-Kutta integration for the radial position. Simulations were performed with the electric field symmetric on both sides of the aperture, as well as with the field turned off between the aperture and the detector, modeling the limit of a perfectly conductive cavity enclosing the instrument. Particle trajectories were individually tracked and charged particle interactions were not included, as the particle density in the experiments is small. The simulated proton density striking the detector is shown in Fig. 9b for the case of symmetric fields. The solid line represents the proton density when no net potential exists between the source and the aperture, and the dashed line represents the proton density for a 1-MV potential.

The purpose of this study was to estimate the effect of a potential difference between the aperture and the capsule on the prf of the camera. For both symmetric and asymmetric fields, the prf was found to be broadened by only ~ 1 μm. (Additional simulations were also performed for a 500-μm radius aperture, as well as for a 0.1-MV potential. None of the studies produced a significant broadening of the image.)

C. Scattering in aperture walls

One advantage of proton-emission imaging is that a thin aperture substrate is sufficient to stop D^3He protons, providing a well defined aperture edge. The apertures commonly used consist of a 2000-μm diameter cylindrical hole in a 500-μm thick Ta substrate. The 14.7-MeV protons would be completely stopped by ~ 400 μm of Ta. Protons that travel through less Ta may be stopped in the ranging filters located in the detector pack. Ideally, no detected protons would have scattered in the Ta. However, since no aperture is perfectly tapered to match the trajectories of incoming protons, some protons will strike the inner walls of the aperture and scatter through a thinner section of Ta, as illustrated in Fig. 10a. If the section is thin enough, protons may exit the opposite side, travel to the detector pack, pass through the ranging filters, and be detected on the CR-39. Since scattered proton trajectories are unknown, no information about the source is gained; instead the desired signal is broadened.

Simulations were performed to estimate the degradation of the camera prf by proton scattering in the Ta substrate utilizing the Monte Carlo program TRIM[27] to evaluate the slowing down and scatter of charged particles in matter. The source was treated as a 12-MeV monoenergetic point source of protons, chosen to approximate the observed mean energy of D^3He protons after escaping a 20-μm CH capsule implosion. TRIM was used to determine the amount of scatter produced by discrete thicknesses of Ta; since the aperture wall presents a continuous range of thicknesses to protons, some assumptions were made to transform the 1-D TRIM output into the 2-D geometry of the aperture. Instead of modeling the continuous range of thicknesses, a series of seven discrete thickness steps was used. Depending on where the proton entered the aperture

wall, the encountered material was approximated by one of seven Ta sheets, ranging in thickness from 10 μm to 150 μm. (Any proton encountering more than 150 μm of Ta would be stopped by the ranging filters.) Several million protons were tracked through each discrete thickness. Upon exiting the Ta material, the energy and trajectory of each proton was recorded.

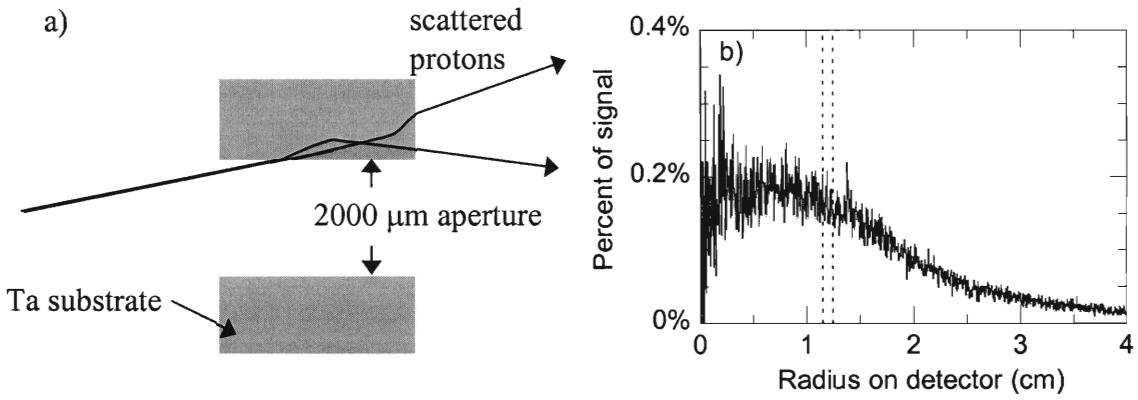

Figure 10 Proton scattering in the aperture substrate

FIG. 10 (a) Illustration of a magnified cross sectional view of an aperture, defined as a 2000-μm diameter hole in a 500-μm thick tantalum substrate. Not shown are the source and the detector, located 3 cm to the left and 33 cm to the right, respectively. As seen in the figure, the geometry dictates that protons may encounter less than 500 μm of Ta. If the amount of Ta encountered is sufficiently thin, the protons will exit the tantalum and may broaden the image. (b) Illustrated is the simulated ratio of the scattered proton density to the unscattered signal proton density on the detector. The dotted lines represent the approximate location of an image penumbra from a ~ 30 μm source. The calculated broadening of the point source was << 1 μm.

These trajectories, along with the system geometry, were used to predict whether scattered protons would strike the detector plane. The system geometry mimicked the actual experimental hardware; modeling of the three main components, the source, the aperture, and the detector was included. The geometry was similar to that seen in Fig. 2b, where the distance from TCC to the aperture was taken to be 3 cm, and the distance from the aperture to the detector was 33 cm. The aperture was modeled by a 2000-μm diameter hole centered in a 500-μm thick Ta disk. Based on this geometry and the recorded trajectories from TRIM, the scattered protons reaching the detector pack were isolated from those that did not.

Each proton deflected towards the detector pack then encountered additional filtering before reaching the detector. The filtering, placed directly in front of the detector, was assumed to be 20 μm of Al followed by 1000 μm of Mylar and an additional 100 μm of Al. Mylar was substituted for CR-39 due to similarities in their chemical composition and stopping properties. The proton was assumed detected if the energy was great enough to allow passage through these additional filters.

Thus, a record of the detection locations of all the scattered protons with an appropriate trajectory and energy was created. The ratio of the scattered proton density to unscattered signal proton density as a function of the detector radius is shown in Fig. 10b; the dotted lines indicate the approximate location of the image penumbra from a ~ 30-μm source. The simulations showed that the scattered protons represent less than 0.3% of the detected protons in the penumbral region, and that the density of scattered protons is fairly uniform. Since the derivative of the proton density ultimately determines

the size and shape of the source,[11] the small amplitude, fairly uniform background would have little effect. Broadening of the prf was found to be << 1 μm.

D. Scattering in filters

Upon reaching the detector pack, protons pass through several ranging filters that are designed to reduce the incident proton energy for optimal detection efficiency. Along with the desired loss of energy, the protons will experience lateral straggling, another possible source of spatial broadening.

The Monte Carlo code TRIM[27] was again used, this time to track 12-MeV protons from a point source through 20 μm of Al, 1000 μm of Mylar, and a final 100 μm of Al. The lateral positions for protons exiting the filters were recorded and fit by a Gaussian distribution with an ~ 30-μm e folding radius. This translated to a broadening in the prf of 30/M, where M is the geometric magnification of the camera; for a 12.5x magnification, this corresponds to ~ 3 μm broadening.

E. Net broadening

The net result of these independent broadening effects can be estimated for OMEGA laser shot 35176, where the measured R_{burn} is 31 ± 2.5 μm. Taking the four sources of broadening discussed, the error in R_{burn} is given by:

$$error \approx \sqrt{31^2 + \left(3^2 + 1^2 + 0^2 + 3^2\right)} - 31 \approx 0.3\,\mu\text{m} \qquad (3)$$

The net effect is insignificant compared to the statistical uncertainty of ± 2.5 μm.

V. Fidelity of the reconstructed images

The following subsections describe systematic tests that demonstrate the fidelity of the reconstructed burn images. The tests are based on a variety of carefully selected implosions that have been studied with the proton-emission imaging cameras. In Sec. A, system consistency and implosion symmetry are experimentally demonstrated when three repeatable measurements of R_{burn} are obtained, each from an independent PCIS camera imaging the same symmetrically driven implosion. Sec. B shows that the reconstructed burn profiles are independent of changes in the system magnification and the aperture size. Sec. C presents data suggesting that ambient fields do not affect the system response.

A. Repeatability of the measured burn profiles

The first experimental test of the fidelity of the reconstructed burn images was performed by examining the repeatability and accuracy of the measured burn profiles. Representative results are shown in Fig. 11a for shot 36730, an implosion of a 17-μm plastic-shell capsule filled with a mixture of 6 atm of D_2 and 12 atm of ^3He gas. The symmetrically driven implosion was imaged with three separate PCIS cameras, fielded in TIMs 2, 3, and 4. (TIM3 is located 109 degrees from TIM2, and TIM4 is 101 degrees from TIM2 and 79 degrees from TIM3.) Each camera produced an independent measurement of R_{burn}. The filtering was selected for front-back detection of D^3He protons, providing two measurements from each camera. The repeatability of the system and the symmetry of the implosion are demonstrated in the R_{burn} results shown in Fig. 11a, where the measured burn size from all three cameras was the same. The

horizontal dotted line represents the mean value; the error bars were calculated in the manner discussed in Sec. III. (Note: these data are subsequently referred to in the following sections where the geometric magnifications, M, are discussed.)

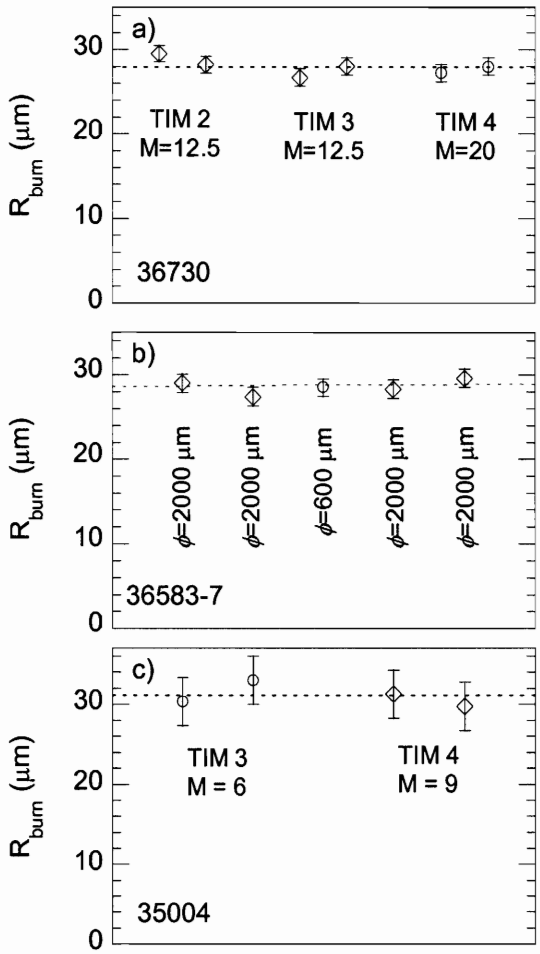

Figure 11 Representative experimental data illustrating systematic tests

Fig. 11. R_{burn} data are shown with the average measurement value (dotted line) for a series of experiments. (a) A 17-μm-thick plastic-shell implosion with an 18-atm D^3He gas-fill (laser shot 36730) was imaged by three nearly orthogonal imaging cameras, located in TIM 2, 3, and 4. The geometric magnification (M) of each camera is shown. The data illustrate the accuracy and repeatability of the measurement. (b) A single camera imaged a series of 19-μm thick plastic-shell implosions with a gas fill of 10.5 atm D_2 and 6 atm ^3He. The aperture diameter (ø) used for each camera is indicated, thus illustrating that R_{burn} was unaffected by the change in aperture size (c) A 20-μm thick plastic-shell implosion with an 18-atm D^3He gas fill was imaged by two cameras, placed in TIM 3 and 4. The difference in M for the two cameras produced no change in the measured R_{burn}. (The errors, which are strongly correlated to the D^3He yield, are generated from the chi squared analysis illustrated in Fig. 6. A front-back detection scheme in a) and c) generated two images, and two values of R_{burn} for each camera.)

B. Response to geometric changes

Since the reconstruction algorithm incorporates the geometric setup of the camera, the final measurement of R_{burn} should be independent of any geometric changes. The response of the system to known changes in geometry is demonstrated through two sets of experiments. In the first set, the aperture diameter was dramatically altered while other camera parameters remained unchanged. Five successive capsules were imploded, beginning with laser shot 36583. (Results are shown in Fig. 11b for capsules ~ 860 μm in diameter, with a 19-μm plastic shell and a D_2 10.5-atm and ^3He 6-atm gas fill.) For each implosion, one TIM was equipped with a PCIS camera. For the first two implosions, the PCIS camera was equipped with a 2000-μm diameter aperture. On the third implosion the aperture diameter was 600 μm. The remaining two implosions were again imaged with 2000-μm apertures. The dotted line in Fig. 11b represents the mean value of the data. All results, including that obtained with a 600-μm aperture, were in agreement with the mean value of 28.6 μm. These results demonstrate that aperture size does not affect the measured R_{burn}.

In a second set of experiments, changes in the geometric magnification (M) are used to demonstrate that R_{burn} is independent of system geometry. For these experiments, R_{burn} was shown to be unaffected by a change in L_1 (Fig 2b), the distance from TCC to the aperture, (shot 35004) and by a change in L_2, the distance from the aperture to the detector (shot 36730). The results are presented in Fig 11c and 11a, respectively. No significant change in R_{burn} was observed from camera to camera; R_{burn} was not dependent on system magnification. (In shot 35004, L_1 was 5.4 cm for the camera in the TIM3 port,

and 3.7 cm for the camera in TIM4. In shot 36730, L_2 was 36.6 cm for the cameras in TIM2 and TIM3, and 58.6 cm for the camera in TIM4. Shot 35004 was the implosions of a 20-μm plastic-shell capsule filled with a mixture of 6 atm of D_2 and 12 atm of ^3He)

C. Response to ambient fields

Several plastic shell implosions were used to look for possible systematic errors associated with stray fields. In the first experiment, two cameras were fielded for laser shot 35004. As previously discussed, the two cameras were set up identically except for a 1.7-cm change in L_1. If fields were significantly influencing protons in the region between the capsule and the aperture, we would expect to see a difference in the measured R_{burn} from these two cameras. The results shown in Fig. 11c report essentially the same R_{burn} for both cameras, suggesting that there are no serious field effects in the region before the aperture.

In the second experiment, a change in the distance between the aperture and detector, an area surrounded by a conductor, was used to demonstrate that stray fields are not seriously affecting R_{burn}. For shot 36730, three cameras were set up identically except for a 22 cm difference in L_2 for the TIM 4 camera. If fields were affecting the protons between the aperture and detector, we would expect to see a difference in measured values of R_{burn}. As seen in Fig. 11a, no significant difference was observed in results from the TIM4 camera, suggesting that there are no serious field effects in the region behind the aperture.

A recent experiment[33] also provides evidence that fields do not dramatically alter the trajectory of D^3He protons in the region past the aperture. In this test, a steel grid (50-μm diameter wires, with 100 wires per inch) was placed directly in front of the

imaging aperture. Examination of the proton-emission image revealed no distortions in the grid-induced pattern. This qualitative evidence again supports the evidence that fields are not significantly altering the trajectories of 14.7-MeV D^3He protons.

VI. Discussion

Spatial measurements of fusion burn are essential for understanding the complex dynamics of imploding capsules, including such effects as mix, drive asymmetry, and radiation and electron transport. Such burn images and absolute profiles provide one of the best integral tests of our understanding of the complex dynamics of these implosions. To this end, we have built three proton core imaging cameras for imaging D^3He burn through energetic 14.7-MeV protons; these cameras have been extensively used to study a wide range of capsule implosions for a variety of drive conditions, from which characteristic burn radii from 20 to 80 μm were measured. (Detailed, systematic studies of these implosions as functions of capsule gas pressure, shell thickness, laser energy and smoothing, and capsule type are reported elsewhere,[13] as are images of asymmetric burn regions resulting from laser drive asymmetry.[12]) This paper focuses on the imaging hardware, the nature of the imaging data and processing for symmetric burn, and various experimental and theoretical tests that demonstrate repeatability, self consistency, and freedom from distortion in the reconstructed burn profiles.

Acknowledgements

The authors express their gratitude to the OMEGA engineers and operations crew who supported these experiments. In addition, we would like to personally thank Candice Culligan, and Jocelyn Schaeffer for their continuous help.

References

1. J. Nuckolls, L. Wood, A. Theissen *et al.*, Nature (London) **239**, 139 (1972).
2. S. E. Bodner, D. G. Colombant, J. H. Gardner *et al.*, Phys. Plasmas **5**, 1901 (1998).
3. D. Ress, R. A. Lerche, R. J. Ellis *et al.*, Rev. Sci. Instrum. **59**, 1694 (1988).
4. R. A. Lerche, D. Ress, R. J. Ellis *et al.*, Laser Part. Beams **9**, 99 (1991).
5. C. R. Christensen, D. C. Wilson, C. W. Barnes *et al.*, Phys. Plasmas **11**, 2771 (2004).
6. L. Disdier, R. A. Lerche, J. L. Bourgade *et al.*, Rev, Sci. Instrum. **75**, 2134 (2004).
7. Y. -W. Chen, M. Yamanaka, N. Miyanaga *et al.*, Opt. Commun. **73**, 227 (1989).
8. M. Nakai, M. Yamanaka, H. Azechi *et al.*, Rev. Sci. Instrum. **61**, 3235 (1990).
9. A. P. Fews, P. A. Norreys, F. N. Beg *et al.*, Phys. Rev. Lett. **73**, 1801 (1994).
10. K. A. Nugent and B. Luther-Davies, Opt. Commun. **49**, 393 (1984).
11. F. H. Séguin, J. L. DeCiantis, J. A. Frenje *et al.*, Rev. Sci. Instrum. **75**, 3520 (2004).
12. F. H. Séguin *et al.*, (to be submitted Phys. Plasmas).
13. J. L. DeCiantis *et al.*, (submitted Phys. Plasmas).
14. J. L. DeCiantis, MS Thesis, Massachusetts Institute of Technology (2005).
15. T. R. Boehly, D. L. Brown, R. S. Craxton *et al.*, Opt. Commun. **133**, 495 (1997).
16. F. H. Séguin, J. A. Frenje, C. K. Li *et al.*, Rev. Sci. Instrum. **74**, 975 (2003).
17. J. A. Frenje, C. K. Li, F. H. Séguin *et al.*, Phys. Plasmas **11**, 2798 (2004).
18. R. D. Petrasso, J. A. Frenje, C. K. Li *et al.*, Phys. Rev. Lett. **90**, 095002 (2003).
19. A series of burn images have been obtained from thin glass implosions involving less than 23 kJ of laser energy,[13] several thick plastic shell implosions involving 18 kJ and

30 kJ of laser energy,[12,14] and a few implosions involving different shaped laser pulses.[14]

20. T. R. Boehly, V. A. Smalyuk, D. D. Meyerhofer *et al.*, J. Appl. Phys. **85**, 3444 (1999).
21. For shot 35176, the D^3He yield obtained from the penumbral image was a ~ 35% lower than the yield measured by the proton spectrometers. This difference was due to too little filtering placed in front of the CR-39, thus reducing the detection efficiency.
22. There are also uncertainties involved in determining the shape of the source, but they are generally small in comparison to the uncertainties in determining the width. For example, for the data in Sec. III, a uniform shaped source corresponds to a reduced chi squared of 2.0.
23. C. K. Li and R. D. Petrasso, Phys. Plasmas **2**, 2460 (1995).
24. C. K. Li and R. D. Petrasso, Phys. Rev. Lett. **70**, 3059 (1993).
25. C. K. Li, D. G. Hicks, F. H. Séguin *et al.*, Phys. Plasmas **7**, 2578 (2000).
26. F. H. Séguin, C. K. Li, J. A. Frenje *et al.*, Phys. Plasmas **9**, 3558 (2002).
27. SRIM, a code for calculations of the Stopping and Ranging of Ions in Matter, Jan. 1 2004, Version 2003.26 (J. F. Ziegler and J. P. Biersack).
28. D.E. Post, R.V. Jensen, G.B. Tarter *et al.*, Atomic Data and Nuclear Data Tables **20**, No. 5 (1977).
29. J. D. Jackson (1999). Classical Electrodynamics (3). New York, NY: John Wiley & Sons, Inc.

30. A 3-μm broadening of the prf for an R_{burn} of 31 μm would translate to an error in R_{burn} of only 0.16 μm. ($error \approx \sqrt{31^2 + 3^2} - 31 \approx 0.16\,\mu m$)

31. D.G. Hicks, C. K. Li, F. H. Séguin *et al.*, Phys. Plasmas **8**, 606 (2001).

32. D.G. Hicks, C. K. Li, F. H. Séguin *et al.*, Phys. Plasmas **7**, 5106 (2000).

33. C. K. Li (to be submitted).

3. Dependence of burn profiles on implosion conditions in inertial confinement fusion experiments

J. L. DeCiantis, F. H. Séguin, J. A. Frenje, C. K. Li, J. R. Rygg, C. D. Chen, B. E. Schwartz, R. D. Petrasso[a)]
Plasma Science and Fusion Center, Massachusetts Institute of Technology, Cambridge, Massachusetts, 02139

J. A. Delettrez, S. P. Regan, V. A. Smalyuk, V. Yu. Glebov, J. P. Knauer, F. J. Marshall, D. D. Meyerhofer[b)], S. Roberts, T. C. Sangster, C. Stoeckl
Laboratory for Laser Energetics, University of Rochester, Rochester, New York, 14623

K. Mikaelian, H. S. Park, H. F. Robey
Lawrence Livermore National Laboratory, Livermore, California 94550

Abstract

Radial profiles of nuclear burn in directly driven capsule implosions have been extensively studied for the first time using a proton-core imaging system sensitive to energetic 14.7-MeV protons from the fusion of deuterium and 3-helium. Several types of implosion experiments, conducted at the OMEGA laser facility, were found to affect the spatial profiles. Characteristic burn radii of thick CH-shell capsules, with initial radii of ~ 430 μm, were about 30 μm, but for the entire range of implosions, the burn radii varied between 20 and 80 μm. To explore the effect on the size of the burn region, gas pressure, shell thickness, laser energy, laser smoothing, capsule size, and capsule composition were systematically varied. Reducing the D^3He fill pressure from 18 to 3.6-atm in 20-μm thick CH shells resulted in the burn radius changing from 29.1 ± 0.3 μm to 22.8 ± 0.7 μm, a reduction largely attributed, not to increased convergence, but to increased fuel-shell mix for the more unstable 3.6 atm implosions. Increasing the shell thickness from 17 to 24 μm for 18 atm fills, resulted in the burn radius increasing from 27.8 ± 0.4 μm to 31.3 ± 1.0 μm, a modest increase in burn radius largely attributed to the slightly smaller convergence of the more massive, thicker-shell capsules. Results from hard x-ray images (4-5 keV) were observed to closely track the nuclear measurements. The set of absolute burn profiles, in combination with other important implosion diagnostics, constitute a significant advance by providing an exacting, integral test of the complex dynamics of imploding capsules.

a) Also Visiting Senior Scientist, Laboratory for Laser Energetics, University of Rochester.
b) Also Departments of Mechanical Engineering, Physics and Astronomy.

I. Introduction

Detailed nuclear burn images of imploding inertial confinement fusion (ICF)[1-3] capsules are required to fully assess the complicated dynamics, including such effects as mix and drive efficiency. They provide a compelling integral test of all the processes involved in an implosion. In the direct-drive approach to ICF, a spherical capsule containing the fuel is compressed and heated by direct illumination of laser beams focused on the capsule surface in a nominally uniform fashion.[2] Hydrodynamic instabilities affect the performance of these implosions,[2-10] ultimately determining the size, symmetry, and yield of the nuclear burn region. This article presents the first comprehensive studies of the D^3He burn profiles for numerous direct-drive implosions with diverse capsule and drive conditions. Burn profiles and yields are obtained from energetic 14.7-MeV protons from the fusion of deuterium (D) and 3-helium (^{3}He).[11] In addition, complementary data from x-ray images,[12-15] proton spectrometers,[16-21] and clean 1-D simulations[22,23] are used. Neutron-emission images using deuterium-tritium filled capsules have been previously reported, but for a more limited scope of implosions.[8,24]

Section II describes the drive conditions, general aspects of the penumbral image burn-reconstruction algorithm, and the relevant diagnostics. Section III provides additional details about the reconstruction algorithm and an analysis of two distinctly different implosions that have dramatically different burn regions. Similarities and differences in nuclear burn and x-ray images are discussed; important connections between burn profiles, areal density (ρR), and yield measurements are established; and comparisons between clean 1-D simulations and the burn profiles are made. Section IV

summarizes the results obtained when capsule and drive conditions were systematically altered to modify the burn region. In particular, the dependence of the burn radius on shell thickness, gas pressure, laser energy, laser smoothing, and shell type were investigated for a large set of implosions. Section V summarizes the results and future work. (For a detailed discussion of the imaging hardware and exacting tests of the fidelity of the reconstructed images, see references 11, 25, and 26.)

II. Experimental conditions and overview

The experiments described here were performed on the OMEGA[27] laser system at the Laboratory for Laser Energetics, University of Rochester. OMEGA is a 60-beam, frequency-tripled UV light (0.35 μm) laser capable of delivering up to 30 kJ of laser energy in a variety of pulse shapes. The individual laser beams were smoothed with distributed phase plates (DPPs),[28] two-dimensional smoothing by spectral dispersion with a bandwidth of 1.0 THz,[29] and polarization smoothing using birefringent wedges.[30] Both SG3 and SG4 DPPs were used in the experiments described here; the different DPPs produce different beam intensity profiles.[31-33] In this work, only 1-ns square laser pulses were used to directly illuminate the capsule. The beam-to-beam energy imbalance was typically less than 4% rms.

To explore the range of burn regions associated with different kinds of symmetrically driven implosions, and to reveal the complicated physics, such as mix, drive efficiency, and core distortions, a wide variety of implosions were examined. Unless otherwise noted, all implosions involved 20 - 23 kJ of laser energy and SG4 DPPs. Capsules with 1.8 to 2.3 μm thick glass (SiO_2) shells, filled with 18-atm D^3He

gas, and capsules with 17 to 24 μm thick plastic (CH) shells, filled with 3.6 or 18 atm D^3He gas, were imploded. The glass-shell implosions used the SG3 DPPs. Initial capsule radii were nominally 470 μm for the SG3 DPPs and 430 μm for SG4 DPPs.

The primary nuclear reaction diagnosed is

$$D+^3He \rightarrow ^4He(3.6MeV) + p(14.7MeV)\,. \tag{4}$$

The proton core imaging system (PCIS) cameras imaged the time-integrated D^3He proton emission, while proton spectrometers measured the time-integrated proton energy spectrum, from which the areal density, ρR, was determined.[16-21]

Energetic nuclear-burn protons were detected using up to three, nearly orthogonal penumbral imaging cameras.[11,25,26] Symmetric or asymmetric reconstruction algorithms were applied to the penumbral images.[11,26] For the symmetrically driven implosions discussed in this paper, only the symmetric algorithm is used.[34] The result of this analysis leads to an absolute radial burn profile (reactions per unit volume) and the corresponding burn size (R_{burn}), representing a single e folding of the profile.

Each proton-emission imaging camera consists of a round imaging aperture that is significantly larger than the size of the D^3He burn region, and a detector pack comprised of several ranging filters and CR-39 charged-particle detectors.[25,17] The distances of the implosion to the imaging aperture, and the imaging aperture to the detector pack (L_1 and L_2, respectively) determine the geometric magnification $M \equiv L_2 / L_1$. Aperture diameters of 600 μm and 2000 μm were used, with geometric magnifications between 8x and 20x. The energetic protons that pass through the aperture are detected with ~ 100% efficiency in the CR-39, as long as the detector has filtering that slows incoming protons down to the CR-39 sensitivity range of about 0.5 to 8 MeV.

Pinhole cameras were used to obtain 4 - 5 keV x-ray emission images.[12-14] The images correspond to approximately to the time of peak-proton production and were taken at 12x magnification, with a ~ 40 ps gating at about 58 ps intervals.[14] At the time of peak-proton production, the detected x rays are primarily produced from 4 – 5 keV bremsstrahlung radiation emitted from heated inner surface of the shell material.[7,35]

Up to five proton spectrometers[17] were used to obtain time-integrated measurements of the D^3He proton spectrum from which the total burn-averaged areal density (<ρR>) was determined.[16] For these experiments the measured <ρR> comprises both the shell <ρR> and the fuel <ρR>, but is usually dominated by the shell.[17,21,36]

III. Examples of nuclear burn region analysis

The symmetric reconstruction algorithm fits the data with a family of functions that correspond analytically to a family of local burn profiles that can vary continuously from hollow to Gaussian.[11] On the basis of chi-squared minimization, most data were best described by Gaussian profiles

$$P_{burn}(r) = P_0 \exp\left[-(r/R_{burn})^2\right], \tag{5}$$

where r is the radial distance from the center of the implosion, P_0 is the proton emissivity per unit volume at $r = 0$, and R_{burn} is defined as the burn radius.[11,25]

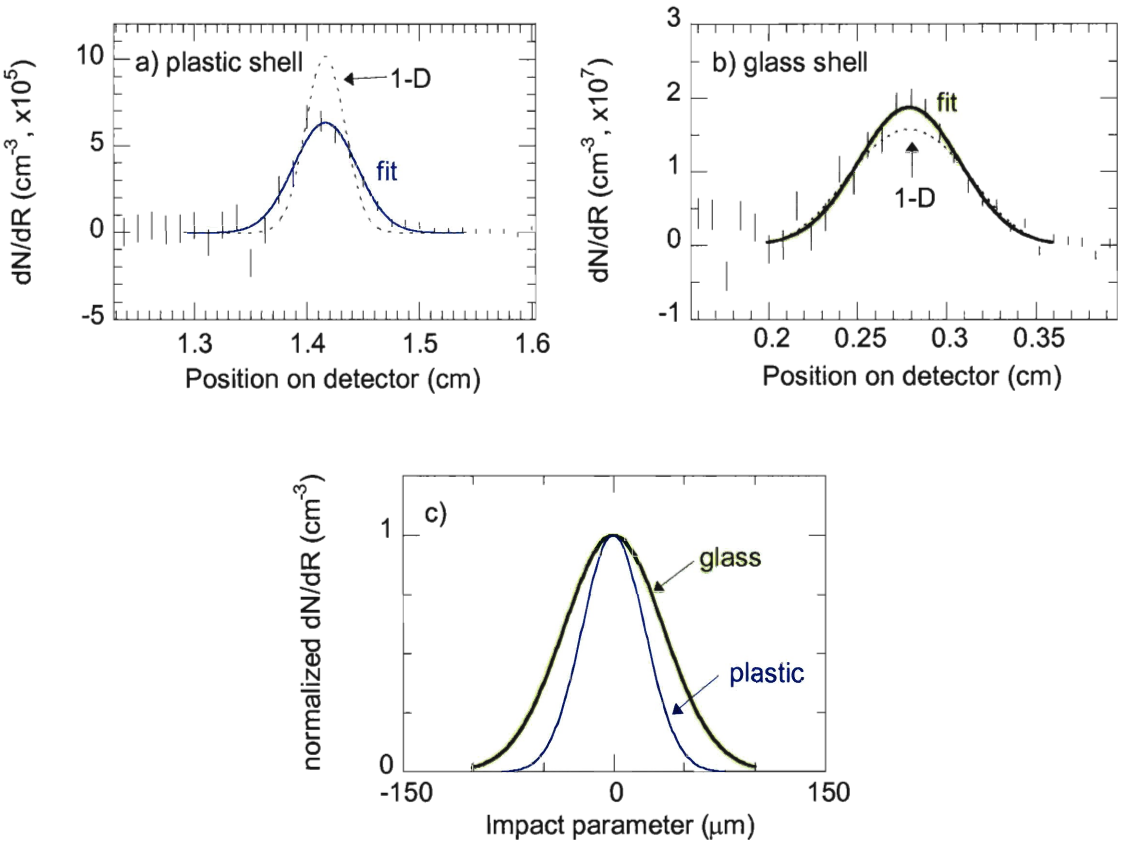

Figure 1 Raw penumbral data from plastic and glass shell implosions

FIG. 1. Illustration of differences in burn regions obtained from two very different implosions: (a) a 20-μm thick plastic-shell capsule (shot 38036), and (b) a 2-μm glass-shell capsule (shot 27456). To clearly show the penumbra of the PCIS image, the data are presented as the radial derivative (dN/dR) of the azimuthally averaged proton density on the detector. The best fits to the data were determined, as described in the text (solid lines), and correspond to Gaussian shaped burn profiles. (c) A direct comparison of burn sizes is shown by plotting the data as a function of the impact parameter relative to the center of the source. In this plot, the heights of the two curves were normalized to be equal at the center. The burn profile width for the glass data (bold line, $R_{burn} = 51 \pm 1.5$ μm) was much broader than the plastic data (line, $R_{burn} = 31 \pm 2$ μm). 1-D calculations are shown for each implosion (dashed lines); reasonable agreement is seen with the glass data, while a significantly narrower burn was calculated for the plastic implosion. Both capsules were filled with 18-atm D^3He gas and irradiated by a 1-ns square laser pulse. The plastic (glass) data were obtained with a 10x (8x) geometric magnification, a 2000 μm (600 μm) diameter aperture, and 23 kJ (12 kJ) of laser energy. The reduced chi squared of the fit to the plastic data was 1.5, and 1.9 for the glass. The 1-D simulations were performed using a flux limiter of 0.06.

The ability to infer R_{burn} provides a direct and useful means to systematically study the spatial extent of the burn region for various implosions, as we illustrate with two very different implosions. Figure 1 shows data from implosions of a 20-μm thick plastic shell (shot 38036, Fig. 1a) and a 2-μm thick-glass shell (shot 27456, Fig. 1b) capsule. The plotted data represent the radial derivative (dN/dr) of the azimuthally-averaged penumbral image values (proton tracks per unit area on the detector). The values of this derivative are proportional to line integrals through the surface brightness of the D^3He burn.[11,25] The error bars represent statistical measurement uncertainties. For each data set, a best fit (solid line) was found, and a symmetric deconvolution was performed to determine R_{burn}. The two fits in Fig. 1c show a significant difference in burn region size. Deconvolution results in $R_{burn} = 31 \pm 2$ μm for the plastic shell implosion, and $R_{burn} = 51 \pm 1.5$ μm for the glass-shell implosion. The fits correspond to a reduced chi squared of 1.5 and 1.9, respectively.

Fusion burn profiles and x-ray pinhole images provide valuable, complementary spatial information about capsule implosions. However, as they have different sensitivities to plasma processes and parameters, a comparison needs to be done cautiously. PCIS probes the nuclear reaction rate

$$RR = N_D N_{3He} \langle \sigma v \rangle_{D3He}, \tag{6}$$

where N_D and N_{3He} are the D and ^{3}He ion number densities, and $<\sigma v>$ is the reaction rate for the D-^{3}He reaction. In contrast, x-ray images are dominated by bremsstrahlung from the heated inner surface of the shell material,[12,14,35] and therefore are most sensitive to the fuel-shell interface. In addition, PCIS images are time integrated over the entire burn, while the x-ray images are gated with a 40-ps window.[14] With these considerations in

mind, and taking an azimuthal average of the x-ray and proton emission brightness profiles,[37] Fig. 2a compares the results of these two diagnostics. The location of the fuel-shell interface was estimated to be at $R_{xray} = 32 \pm 5$ μm, where the x-ray brightness profile peaks before rapidly decreasing with radius (dotted line).[12] (The 5-μm uncertainty is typical for all x-ray data examined here.) The R_{burn} obtained from a proton-emission imaging camera was 31 ± 2.5 μm. The agreement between the two different measurements is quite reasonable. In later discussions and figures we will establish that, for a variety of implosions, the x-ray and nuclear burn profile data respond in a similar fashion to changes in the experimental conditions.

The proton spectrometers measure both the yield of the D^3He reactions and the yield-weighted total $\langle \rho R \rangle$[17,21,36] through the downshift from the 14.7 MeV birth energy.[16-20] Important to this analysis, PCIS and spectrometers typically give the same D^3He yield to within the observed proton-yield asymmetry of 15 - 20% rms.[17]

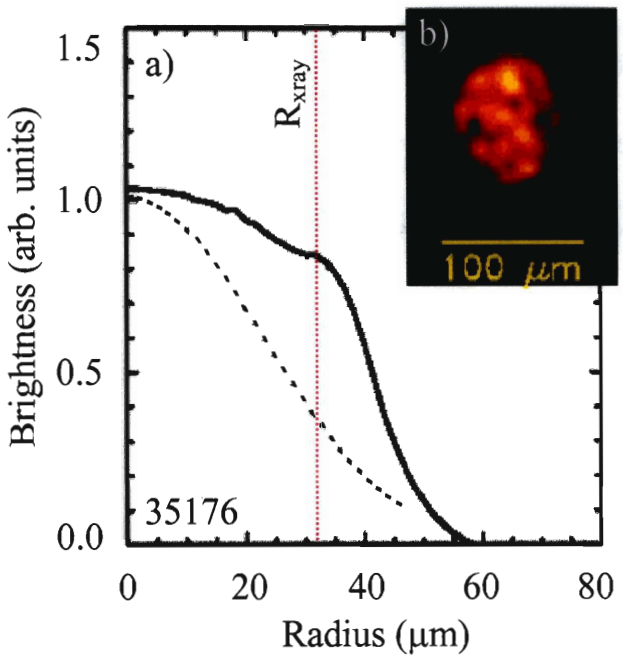

Figure 2 Comparison of x-ray and proton-emission profiles

FIG. 2. (a) Comparison of azimuthally averaged brightness-profiles from an x-ray emission image (solid line) and a proton emission image (dashed line) taken from shot 35176 (an 18-atm D^3He-gas filled, 20-μm plastic-shell implosion). The fuel-shell interface is estimated to be where the x-ray brightness-profile peaks before rapidly decreasing with radius, at $R_{xray} = 32 \pm 5$ μm (red dotted line). R_{burn} from a proton-emission imaging camera was determined to be 31 ± 2.5 μm, consistent with the x-ray data. (b) The corresponding 2-D x-ray pinhole camera image. The 4 - 5 keV x-ray image was taken at the time of peak-proton production with 12x magnification and ~ 40-ps gating. The image display has a logarithmic intensity scaling.

To further elucidate the implosion dynamics, comparisons of the burn data are made to clean 1-D simulations.[22,23] Post-processed 1-D simulated data are normalized to the experimental yield and convolved with the PCIS response function in order to directly compare dN/dR of the experimental data to the simulations (Fig. 1a and 1b, dashed line). As Fig. 1a shows, the 1-D curve for the plastic shell implosion is substantially narrower than the data, while that for the thin-glass shell is much closer, but somewhat broader (Fig. 1b). For numerous CH implosions, the 1-D simulations were narrower than the data

(see also Fig. 3c described below). The difference is not clearly understood at this time, although fuel-shell mix and instabilities in the implosion dynamics are the suspected sources. A thorough search of possible systematic errors leading to artificially broadened image data has not revealed any errors that could account for this discrepancy.[25,38] The role of hydrodynamic instabilities is expected to be substantially smaller in glass-shell implosions,[39] which could account for the closer agreement between simulation and data found in all such cases (see Fig. 3c). Since the post-processed 1-D dN/dR curves are typically Gaussian in shape, the corresponding 1-D R_{burn} will be used to compare to the measured R_{burn}. [The 1-D R_{burn} is not strongly affected by the electron conduction flux limiter used in 1-D simulations, as shown in Fig. A4.]

IV. Systematic studies of R_{burn} on laser energy, laser smoothing, capsule thickness, capsule pressure, and capsule type

Correlations between R_{burn} and the capsule and drive conditions allow an elucidation of some basic implosion dynamics. Systematic studies that examine the dependence of R_{burn} on laser drive energy, on laser smoothing, on capsule wall thicknesses, on capsule type, and on capsule pressure are presented here. These external parameters are often strongly correlated to one or more fundamental quantities and processes, such as ion temperature, capsule convergence, fuel density, and fuel-shell mix. For that reason, whenever possible, attempts were made to change only one external parameter at a time in experiments.

Figure 3a shows the effect of increasing laser energy, for 1-ns square pulses, when irradiating thin glass-shell implosions (Fig. 3a, open diamonds). As the energy was

increased from 6 kJ to 23 kJ, R_{burn} increased from about 30 μm to 80 μm. In contrast, R_{burn} is about 30 μm for 19 – 20 μm CH shells irradiated with 23 kJ of energy, (all capsules at 18-atm D^3He gas). The change in average ion temperature, $\langle T_{ion} \rangle$,[40,41] likely dominates the change in R_{burn} for the glass-shell implosions, as illustrated in Fig. 3b where the data of 3a is replotted as a function of $\langle T_{ion} \rangle$. Increases in $\langle T_{ion} \rangle$ should result in larger R_{burn}, since the D^3He reactivity is extremely sensitive to the ion temperature.

Figure 3c replots the data of 3a along with the corresponding R_{burn} from 1-D simulations (triangles); for the glass shells, reasonable agreement is found, but as mentioned earlier, for the plastic shells there is a significant disparity.

The effects upon R_{burn} of changing the D^3He fill pressure for CH shell implosions were systematically studied (Fig. 4). Figure 4a shows R_{burn} for 18 atm (3.6 atm) gas filled capsule implosions as solid diamonds (open diamonds), plotted as a function of the corresponding measured $\langle \rho R \rangle$. R_{burn} is consistently larger for the 18 than 3.6 atm data and, when plotted as the average measurement value[43] of all implosions shown in Fig. 4a, Fig. 4b is obtained; the plotted values are

$$\langle R_{burn} \text{ (18 atm)} \rangle = 29.1 \pm 0.3 \text{ μm}, \quad (7)$$

$$\langle R_{burn} \text{ (3.6 atm)} \rangle = 22.8 \pm 0.7 \text{ μm} \quad (8)$$

where the error reflect only the statistical uncertainties and do not include possible systematic errors.

Figure 4b shows the corresponding values of R_{xray} for which we have data (blue X for 18 atm and red X for 3.6 atm). The same trend, including the absolute values and the absolute change, is seen in both R_{burn} and R_{xray}. Figure 4c compares values of R_{burn} and $\langle \rho R \rangle$ from 1-D simulations (solid blue triangles for 18 atm and open red triangle for 3.6 atm) to the data, showing significant discrepancies.[44]

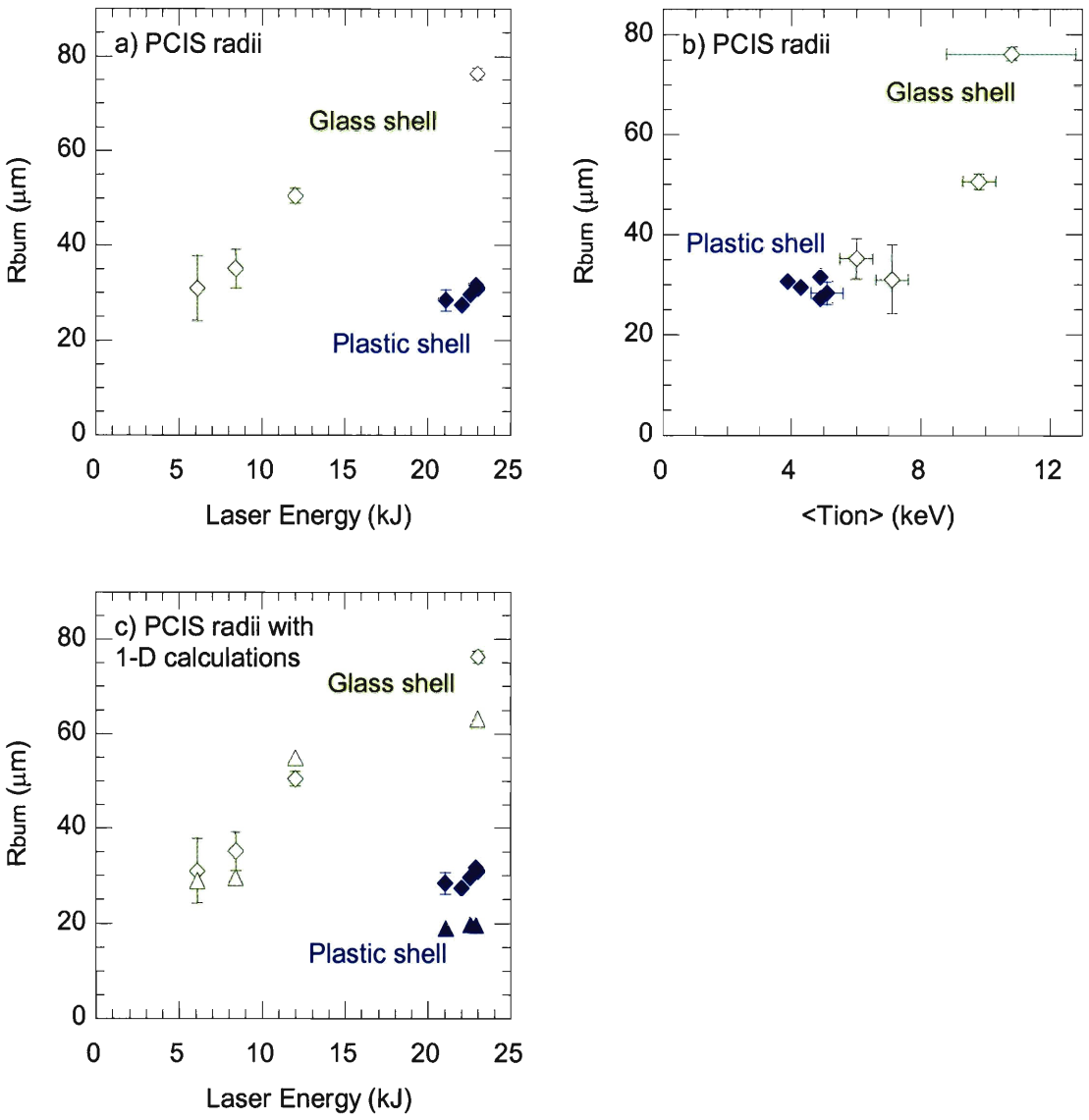

Figure 3 Burn radii for various laser-drive energies

FIG. 3. (a) For the thin-glass-shell exploding pusher type implosions (open diamonds), increasing the laser energy results in a dramatically larger D^3He burn size (R_{burn}). In contrast, for the thick CH-shell compressive implosions at 23 kJ laser energy (solid diamonds),[42] R_{burn} is about 30 μm. The ion temperature was strongly correlated with R_{burn}, as shown in (b) where the data has been replotted versus the burn-averaged ion temperature ($<T_{ion}>$) obtained with neutron time-of-flight systems. (c) The data are displayed with the corresponding R_{burn} from 1-D simulations (triangles). For the glass shells, reasonable agreement is found, but for the plastic shells there is a significant disparity. [See Fig. A2 for a comparison of the measured D^3He proton spectra for these experiments, and Fig A3 for additional thin glass data]

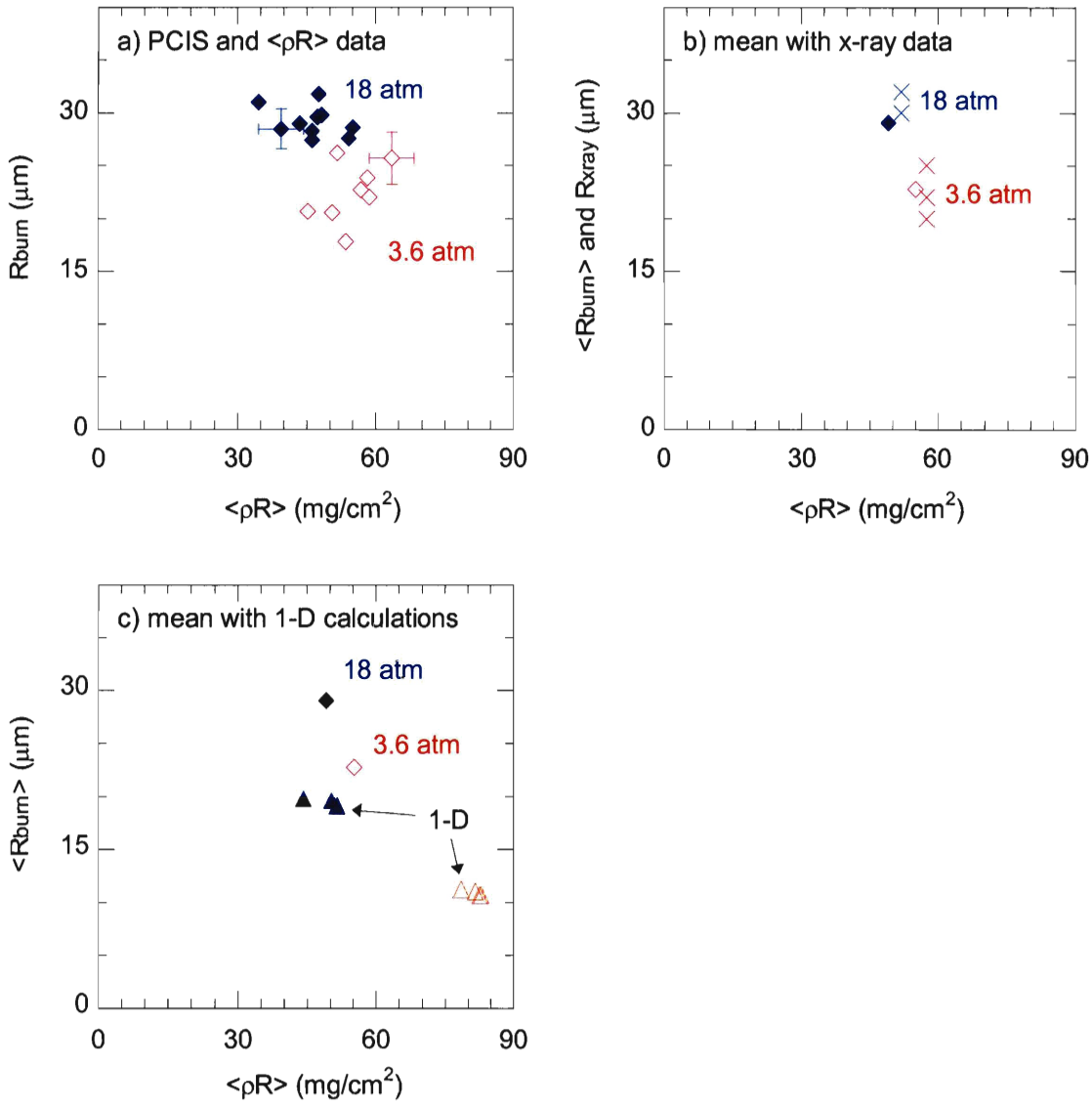

Figure 4 Burn radii for different gas fill pressures

FIG. 4. (a) A significant difference in the D^3He burn size (R_{burn}) is shown for implosions of 19 - 20 μm plastic-shell capsules filled with 18 atm (closed diamonds) and 3.6 atm (open diamonds) of D^3He gas. R_{burn} is plotted as a function of the areal density (<ρR>) measured from proton energy downshifts. (b) The averages of data in (a) are displayed with fuel-shell interface estimates (R_{xray}) for the 18-atm (blue X) and 3.6-atm (red X) implosions, demonstrating reasonable agreement in the absolute values and the absolute change of both R_{burn} and R_{xray}. (c) When the average data are displayed with the 1-D calculated R_{burn} (triangles), the same trend is present, but the absolute values and change are different. Examining the <ρR> from these two implosions types, and from consideration of the work by C.K. Li *et al.*,[4] we hypothesis that an increased fuel-shell mix (associated with the 3.6 atm fills) results in a reduction of, and an increased scatter in, R_{burn}.

The combined results shown in Fig. 4 agree quite well with data published by C.K. Li *et al.*[4] that examined DT gas-filled plastic-shell implosions of various gas-fill pressures. For implosions and gas fills similar to the ones examined here, Li *et al.* concluded that as the pressure was reduced from ~ 18 to 3 atm, the experimental radial convergence was only slightly affected, in distinct contrast to 1-D calculations. In Fig. 4c we see only a slight increase in $\langle\rho R\rangle$, from 49 ± 1 to 55 ± 2 mg/cm^2, as the pressure was changed from 18 to 3.6 atm (solid and open diamonds), while the 1-D simulations for these implosions (solid and open triangles) show a dramatic increase from 49 to 81 mg/cm^2. Li *et al.* argued that an increase in fuel-shell mix occurred for the low-pressure implosions, precluding the increase in ρR predicted by 1-D simulations. This is consistent with the present data, with reduction in R_{burn} for the 3.6 atm data due to an increase of fuel-shell mix. More mix may cause the outer region to preferentially cool as relatively high-Z material (CH) is mixed into the fuel, thus enhancing radiative losses.[35] This temperature drop in the outer mixed regions, coupled with the very strong temperature dependence of the D^{3}He reaction, suppresses the nuclear burn in the mix region, reducing the width of the burn region and R_{burn}. If an isobaric constraint is imposed, enhanced mixing of the outer region also results in fuel dilution and a consequential reduction of R_{burn}. Finally, it is worth speculating that the unstable nature of mix may help explicate the increased scatter of R_{burn} in the 3.6 atm data (Fig. 4a, while the sigma in the 18 atm data is only 1.4 μm, the sigma in the 3.6 atm data is much larger at 5.7 μm), nicely illustrating a decrease in overall stability and repeatability of the implosions.

An important goal of the OMEGA program is to improve the single and overlapping beam uniformity of the laser. To that end, the older SG3 DPPs were recently replaced with the SG4 DPPs, for which the nonuniformities for l modes ~ 5 to 30 were improved.[31-33] To adjust for a reduction in the new spot size, the capsule sizes were also reduced from ~ 470 to 430 μm. Figure 5 shows the effect of these changes upon R_{burn} for several shots, plotted as function of $<\rho R>$. R_{burn} is larger for the SG3 (open-diamonds) than for the SG4 (solid-diamonds) data, and when plotted as the average measurement value[43] of all implosions shown in Fig. 5a, Fig. 5b is generated; this gives

$$<R_{burn}\ (SG3)> = 35.4 \pm 0.7\ \mu m, \tag{9}$$

$$<R_{burn}\ (SG4)> = 29.1 \pm 0.3\ \mu m. \tag{10}$$

As the convergence, determined from the $<\rho R>$,[4] is about the same for the SG3 and SG4 implosions, this suggests that the reduction in R_{burn} for SG4 is largely a consequence of the smaller initial capsule radius.

In Fig. 5b, the corresponding values of R_{xray} show the same trend (orange X for SG3 and blue X for SG4).[45] A similar trend (Fig. 5c) is also seen in comparing 1-D R_{burn} simulations (open triangles for SG3, solid triangles for SG4) to the data ($<R_{burn}>$), but now the absolute change and scale factors are quite different.

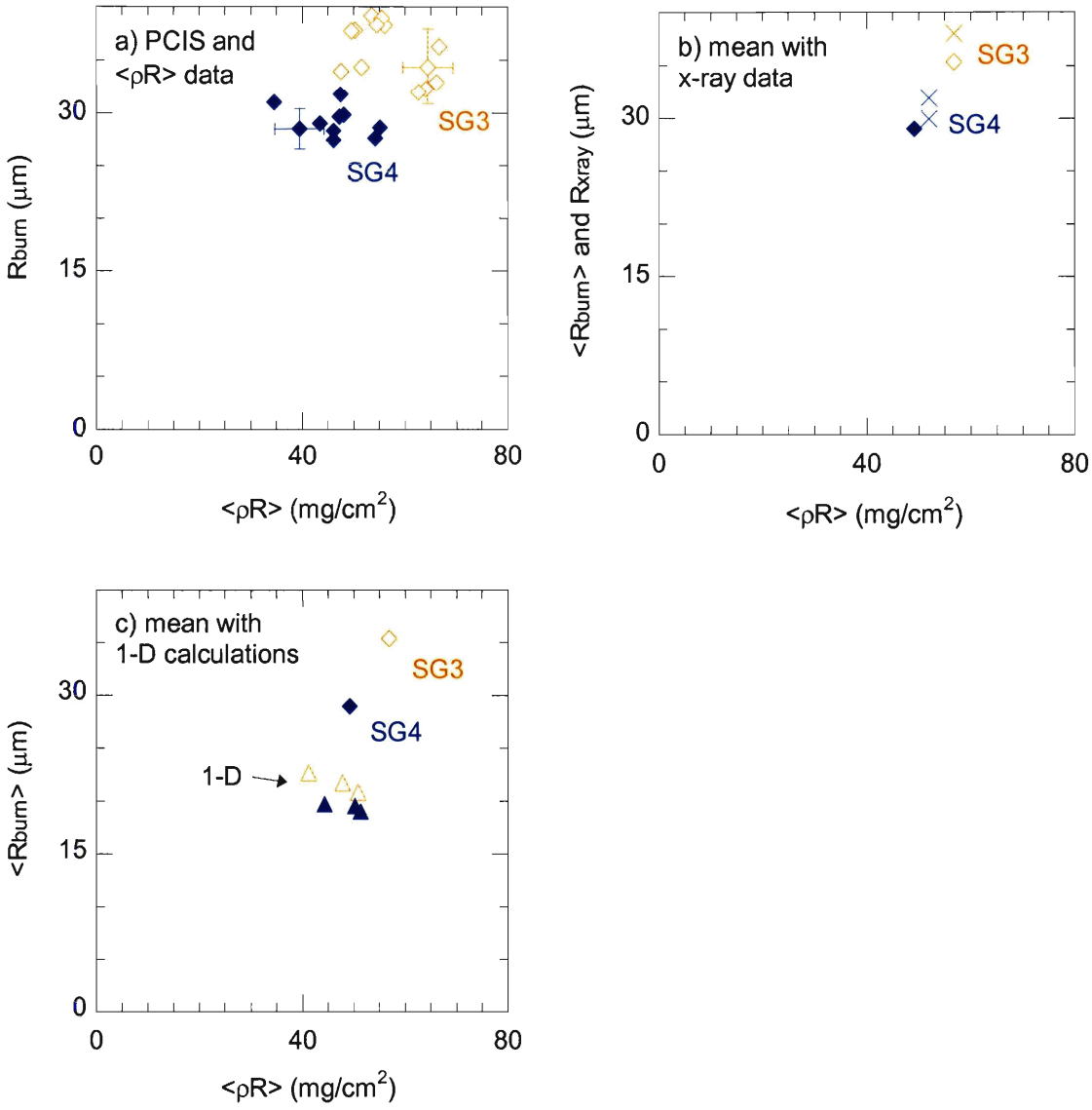

Figure 5 Burn radii for different capsule sizes (SG3 and SG4)

FIG. 5. (a) Consistently smaller D^3He burn radii (R_{burn}) are produced with SG4 targets and phase plates (solid diamonds) than with SG3 (open diamonds). R_{burn} is plotted as a function of the areal density (<ρR>) for implosions involving 18 atm D^3He-gas filled capsules with 19 - 20 μm thick plastic shells. (b) The average burn data in (a) are displayed with fuel-shell interface estimates (R_{xray}) from SG3 (orange X) and SG4 (blue X) implosions,[45] demonstrating agreement in the absolute values and the absolute change of R_{burn} and R_{xray}. (c) When the average data are displayed with the 1-D calculated R_{burn} (triangles), the same trend is present, but the absolute values and change are different. We assume that the reduction in R_{burn} from the SG3 to SG4 implosions is largely dominated by the reduction in initial capsule radius from ~ 470 to 430 μm.

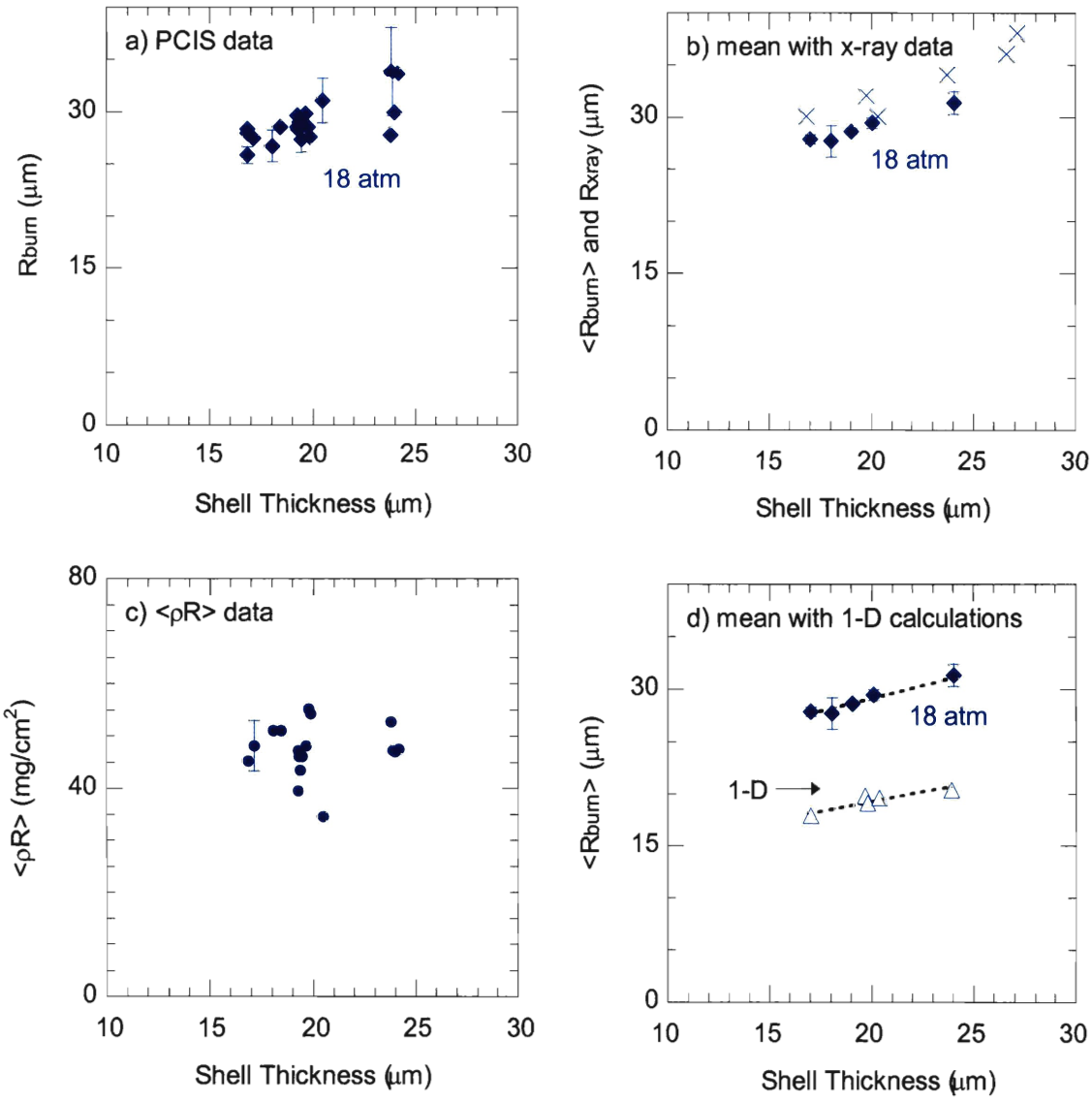

Figure 6 Burn radii for various plastic shell thicknesses

FIG. 6. (a) D^3He burn radius (R_{burn}) dependence on mix and convergence[2-10] is examined through a series of implosions involving capsules with 18 atm D^3He-gas fills and a variable shell thickness. (b) The resulting trend is more obvious when the R_{burn} data are averaged over similar capsule thicknesses (diamonds). The fuel-shell interface estimates (R_{xray}, X) from these implosions, and others, demonstrate reasonable agreement in the absolute values and the absolute change of R_{burn}. (c) The areal densities (<ρR>), taken from the same implosions (circles), were fairly constant over the different shell thicknesses. (d) When the average R_{burn} data are displayed with the 1-D calculated R_{burn} (triangles), the same trend is present, but the now the absolute values and changes are different. The effects of convergence and mix on implosions processes will be further investigated when measurements, such as these, are successfully contrasted to 2-D and 3-D simulations.

The shell thickness is known to have an effect upon mix and convergence.[4-9,10] Figure 6a shows this effect upon R_{burn} (diamonds). The trend of this data is more fully revealed by averaging the data over capsules with similar shell thickness (Fig. 6b). As illustrated, R_{burn} increases slowly as the shell thickness increases from 17 to 24 μm, giving

$$\langle R_{burn}\ (17\ \mu m)\rangle = 27.8 \pm 0.4\ \mu m, \tag{11}$$

$$\langle R_{burn}\ (20\ \mu m)\rangle = 29.4 \pm 0.5\ \mu m, \tag{12}$$

$$\langle R_{burn}\ (24\ \mu m)\rangle = 31.3 \pm 1.0\ \mu m. \tag{13}$$

The convergence for the larger mass capsules is slightly smaller, as reflected in the fact that $\langle \rho R \rangle$ of those capsules are about the same (Fig. 6c);[4] the larger burn radii for the thicker 24-μm capsules reflect the smaller convergence. [See Fig. A7 for the estimated convergence ratios obtained from these implosions.]

R_{xray}, also plotted in 6b (blue X), shows a similar trend to the PCIS results. R_{burn} for 1-D simulations shows the same trend (triangles, Fig. 6d), but the absolute value, as remarked earlier, is much smaller.

V. Summary

In summary, we have presented the first systematic measurements of the size of the nuclear burn profiles for a wide variety of implosion conditions. We have undertaken comprehensive studies examining the dependence of the burn size on shell thickness, gas pressure, laser energy, laser smoothing, and capsule type. These measurements are an important advance since imaging the nuclear burn represents an integral test of all the implosion processes, such as mix and drive efficiency. In our studies we have demonstrated that reducing the D^3He fill pressure from 18 to 3.6 atm in 20-μm CH shells

resulted in the burn radius changing from 29.1 ± 0.3 μm to 22.8 ± 0.7 μm, a reduction in radius largely attributed to increased fuel-shell mix for the more unstable 3.6-atm implosions. Increasing the shell thickness from 17 to 24 μm for 18-atm fills, resulted in the burn radius increasing from 27.8 ± 0.4 μm to 31.3 ± 1.0 μm, a modest increase in burn radius largely attributed to the slightly smaller convergence of the more massive, thicker-shell capsules. Changing the phase plates, with increased laser smoothing for $l \sim 5$ to 30 modes, resulted in the burn radius decreasing from 35.4 ± 0.7 μm to 29.1 ± 0.3 μm; however, this reduction is largely attributed, not to increased capsule convergence, but to the smaller initial radii of the capsules used with the new phase plates. The next step towards investigating the complex dynamics involved in these implosions is to contrast these types of results with detailed 2-D and 3-D simulations.

Acknowledgments

The authors express their gratitude to the OMEGA engineers and operations crew who supported these experiments. In addition, we would like to personally thank Michael Canavan, Candice Culligan, and Jocelyn Schaeffer for their continuous help.

References

1. J. Nuckolls, L. Wood, A. Theissen *et al.*, Nature (London) **239**, 139 (1972).
2. J. D. Lindl, *Inertial Confinement Fusion: The Quest for Ignition and Energy Gain Using Indirect Drive* (Springer-Verlag, New York, 1998).
3. S. Atzeni and J. Meyer-Ter-Vehn (2004). The Physics of Inertial Fusion. New York, NY: Oxford University Press Inc.
4. C. K. Li, F. H. Séguin, J. A. Frenje *et al.*, Phys. Rev. Lett. **89**, 165002 (2002).
5. D. D. Meyerhofer, J. A. Delettrez, R. Epstein *et al.*, Phys.Plasmas **8**, 2251 (2001).
6. R. B. Radha, J. Delettrez, R. Epstein *et al.*, Phys. Plasmas **9**, 2208 (2002).
7. S. P. Regan, J. Delettrez, F. J. Marshall *et al.*, Phys. Rev. Lett. **89**, 085003 (2002).
8. C. R. Christensen, D. C. Wilson, C. W. Barnes *et al.*, Phys. Plasmas **11**, 2771 (2004).
9. D. C. Wilson, C. W. Cranfill, C. R. Christensen *et al.*, Phys Plasmas **11**, 2723 (2004).
10. P. B. Radha, V. N Goncharov, T. B. Collins *et al.*, Phys. Plasmas **12**, 032702 2005).
11. F. H. Séguin, J. L. DeCiantis, J. A. Frenje *et al.*, Rev. Sci. Instrum. **75**, 3520 (2004).
12. S. P. Regan, J. A. Delettrez, R. Epstein *et al.*, Phys. Plasmas **9**, 1357 (2002).
13. D. Ress, L. B. DaSilva, R. A. London *et al.*, Rev. Sci. Instrum. **66**, 579 (1995).
14. V. A. Smalyuk, T. R. Boehly, L. S. Iwan *et al.*, Rev. Sci. Instrum. **72**, 635 (2001).
15. F. J. Marshall, J. A. Delettrez, R. Epstein e*t al.*, Phys. Plasmas **7**, 2108 (2000).

16. F. H. Séguin, C. K. Li, J. A Frenje *et al.*, Phys. Plasmas **9**, 3558 (2002).

17. F. H. Séguin, J. A. Frenje, C. K. Li *et al.*, Rev. Sci. Instrum. **74,** 975 (2003).

18. F. H. Séguin, C. K. Li, J. A. Frenje *et al.*, Phys. Plasmas **9**, 2527 (2002).

19. C. K. Li, F. H. Séguin, J. A. Frenje *et al.*, Phys. Plasmas **10**, 1919 (2003).

20. R. D. Petrasso, J. A. Frenje, C. K. Li *et al.*, Phys. Rev. Lett. **90**, 095002 (2003).

21. C. K. Li, D. G. Hicks, F. H. Séguin *et al.*, Phys. Plasmas **7**, 2578 (2000).

22. M. C. Richardson, P. W. McKenty, F. J. Marshall *et al.*, in *Laser Interaction and Related Plasma Phenomena*, edited by H. Hora and G. H. Miley (Plenum Press, New York, 1986), Vol. 7, pp. 421-448

23. J. Delettrez, R. Epstein, R. C. Richardson *et al.*, Phys. Rev. A **36**, 3926 (1987).

24. L. Disdier, R. A. Lerche, J. L. Bourgade *et al.*, Rev, Sci. Instrum. **75**, 2134 (2004).

25. J. L. DeCiantis *et al.*, (submitted to Rev. Sci. Instrum.).

26. F. H. Séguin *et al.*, (to be submitted Phys. Plasmas).

27. T. R. Boehly, D. L. Brown, R. S. Craxton *et al.*, Opt. Commun. **133**, 495 (1997).

28. Y. Lin, T. J. Kessler, and G. N. Lawrence, Opt. Lett. **20**, 764 (1995).

29. S. Skupsky, R. W. Short, T. Kessler *et al.*, J. Appl. Phys. **66**, 3456 (1989).

30. T. R. Boehly, V. A. Smalyuk, D. D. Meyerhofer *et al.*, J. Appl. Phys. **85**, 3444 (1999).

31. The laser intensity, I, of each beam is described by the super-Gaussian function $I(r) \propto \exp\left[-(r/\delta)^n\right]$ where r is the radius from beam center, and δ is the decay width. For SG3 phase plates $n \sim 3$ and $\delta \sim 300$ μm, while for the more recent

SG4 phase plates, $n \sim 4$ and $\delta \sim 350$ μm. The SG4 phase plates are designed to produce a more uniform laser illumination for low l modes 5 to 30.

32. F. J. Marshall *et al.*, (submitted).

33. S. P. Regan *et al.*, (to be submitted).

34. Symmetry has been demonstrated in two ways: by obtaining the same burn radius from three nominally orthogonal images of the same implosion,[25] and by observing symmetry in 2-D reconstructions of the penumbral image.[11,26]

35. Bremsstrahlung radiation is proportional to $n_e n_i Z_i^2 \exp(-E/kT)/\sqrt{T}$, where n_e and n_i are the electron and ion densities, Z_i is the nuclear charge, E is the photon energy, k is Boltzman's constant, and T is the ambient electron temperature.[7]

36. C. K. Li, F. H. Séguin, D. G. Hicks *et al.*, Phys. Plasmas **8**, 4902 (2001).

37. For any Gaussian shaped burn profile, the corresponding brightness profile is also a Gaussian with the same e folding.

38. Calculations showed insignificant image broadening associated with proton scattering in the capsule, aperture, and detector filters, while experiments showed no indication of errors with the choice of aperture and magnification. Neither experiments nor simulations revealed any serious field effects.[25]

39. M. D. Rosen and J. H Nuckolls, Phys. Fluids **22**, 1393 (1979).

40. V. Y. Glebov, C. Stoeckl, T. C. Sangster *et al.*, Rev. Sci. Instrum. **75**, 3559 (2004).

41. $<T_{ion}>$ represents the burn averaged ion temperature obtained from the neutron time-of-flight systems.[40]

42. No proton-emission images have been obtained from low energy symmetric implosions of thick CH shells.

43. The plotted R_{burn} and $<\rho R>$ results for individual implosions already represent a mean value of the measurements obtained from that implosion; there were as many as 6 measurements of R_{burn}[25] and 5 of $<\rho R>$ for each implosion. When the mean value is calculated for an implosion type, all of these measurements are weighted equally. The error bars do not included possible systematic errors

44. 1-D simulations predict that the 3.6-atm capsules will experience a higher convergence and a higher $<\rho R>$ than the 18-atm capsules, which explains the reduction in the 1-D R_{burn}. However, since Fig. 4c does not show a significant difference in the $<\rho R>$ measurements for the 3.6-atm and 18-atm implosions,[4] we suspect convergence is not responsible for the observed R_{burn} decrease.

45. The SG3 R_{xray} data point was taken from a hydro equivalent 15-atm D_2 gas fill implosion (shot 22546).[7] The substitution is reasonable, since similar R_{xray} results are obtained from hydrodynamically equivalent D_2 and D^3He gas implosions [See Fig. A5].[46]

46. J. L. DeCiantis, MS Thesis, Massachusetts Institute of Technology (2005).

Appendix A. Additional figures

In an effort to maintain a reasonable length for the articles presented in Sections 2 and 3, some non-critical information was omitted for publication. For completeness, some of this material has been included here as Appendix A. The information is arranged in a series of figures meant to supplement the material of Section 2 and 3. Appropriate references to these figures were inserted in text.

Note: All plots included in this document are imbedded KaleidaGraph files. Additional information, including the shot number of each data point are accessible.

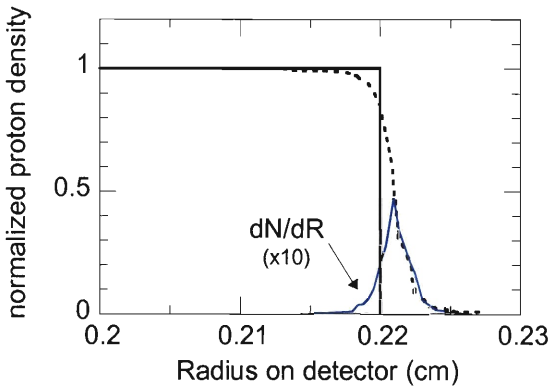

Figure A1 Calculated dN/dR for aperture charging

FIG. A1. The simulated proton density (N) striking the detector as a function of detector radius (R) for the case of no potential (solid bold line) and a 1-MV potential (dashed line) between the capsule and the aperture. The width of the derivative (dN/dR, solid line) from the 1-MV potential was used to determine the broadening of the point source. The resultant broadening at the detector was ~ 11 μm, which corresponds to a ~ 1 μm broadening of the point response function for structure at the capsule (since the geometric magnification is M = 10).

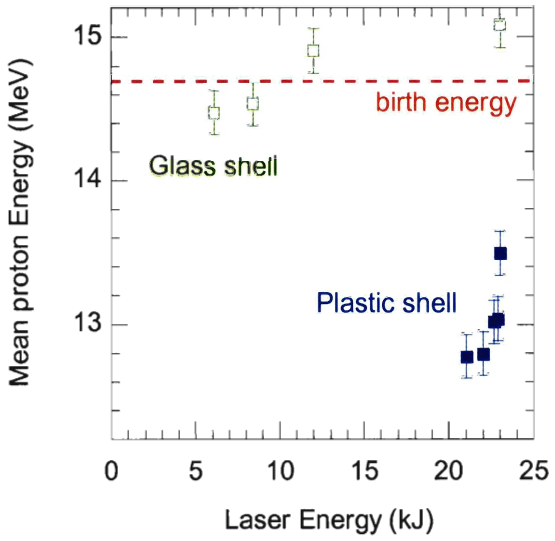

Figure A2 Mean proton energies for glass and plastic-shell implosions

FIG. A2. The 14.7-MeV D^3He protons experience ~ 2-MeV downshift in energy for 20-μm thick plastic-shell implosions (solid squares), and about ± 0.2-MeV shift in energy for thin ~ 2-μm glass-shell implosions (open squares). Peak proton production occurred after the laser pulse was terminated for all implosions except for the 12 kJ and 23 kJ glass-shell implosions. For these two implosions, the protons produced during the laser pulse experience an up-shift in energy due to capsule charging. The large energy downshift for the plastic capsules is attributed to an areal density of ~ 70 mg/cm^2.

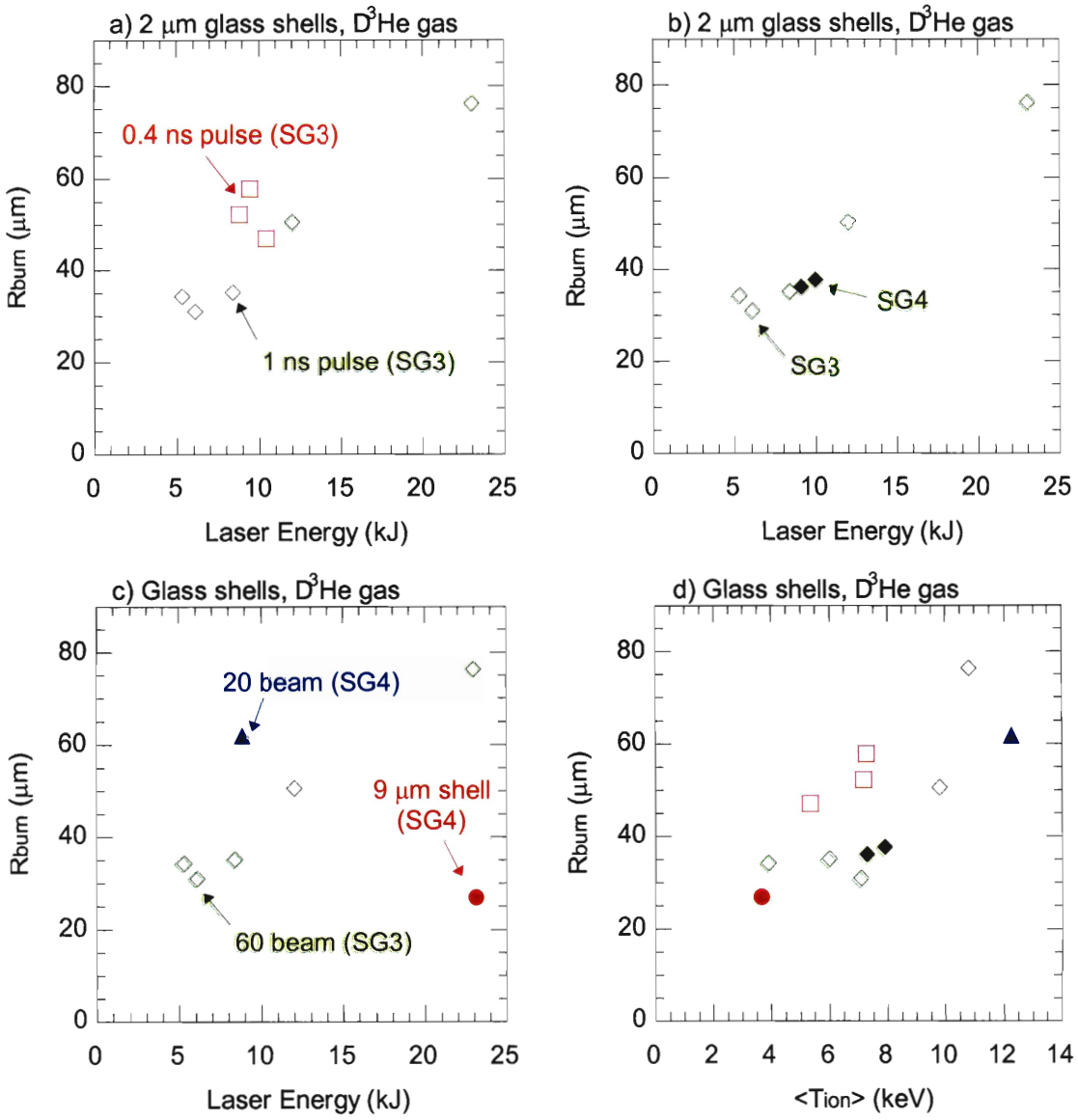

Figure A3 Various glass shell-implosion data

FIG. A3. The D^3He burn sizes (R_{burn}) for thin-glass shell implosions are dependant on various capsule and drive conditions (various SG3 implosions are indicated with hollow markers, and SG4 with solid markers). (a) 2-μm glass-shell implosions driven by 400-ps square laser pulses (open squares) resulted in larger R_{burn} than implosions driven with similar laser energy but delivered in 1-ns square pulses (open diamonds). (b) R_{burn} results from SG4 implosions (solid diamonds) are displayed with the SG3 data (open diamonds). (c) A 2-μm glass-shell implosion, driven by 20 beams with SSD off (solid triangle), and a 9-μm thick glass-shell implosion (solid circle) are also included. (d) The data have been replotted versus the burn-averaged ion temperature ($<T_{ion}>$), illustrating an increase in R_{burn} with temperature.

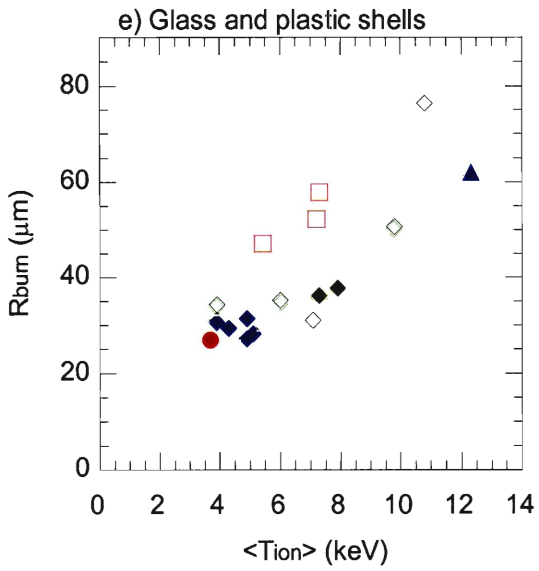

FIG. A3. (e) R_{burn} from a series of 20-μm thick plastic-shell implosions, driven by a 23 kJ 1-ns laser pulse (solid blue diamond), and a variety of glass-shell implosions, are plotted versus the measured ion temperature.

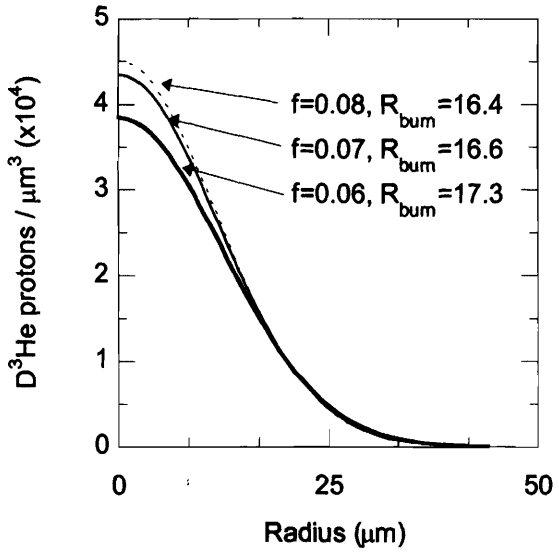

Figure A4 Simulated burn profiles for flux limiters 0.06, 0.07, and 0.08

FIG. A4. The D^3He burn sizes extracted from 1-D simulations are not strongly dependant on the electron conduction flux limiter. Three flux limiters (f) were used to simulate OMEGA implosion 36586 (a 19.2-μm plastic-shell capsule filled with a mixture of 10.5-atm D_2 and 6-atm ^3He gas). The 1-D simulated burn profiles were normalized to the experimental D^3He yield of 1.4×10^9 and fit with a Gaussian to determine the 1-D R_{burn}. A significant change in the flux limiter from 0.06 to 0.08 resulted in only a modest decrease in R_{burn} from 17.3 to 16.4 μm, while the 1-D yield increased considerably from 2.7×10^9 to 1.7×10^{10}.

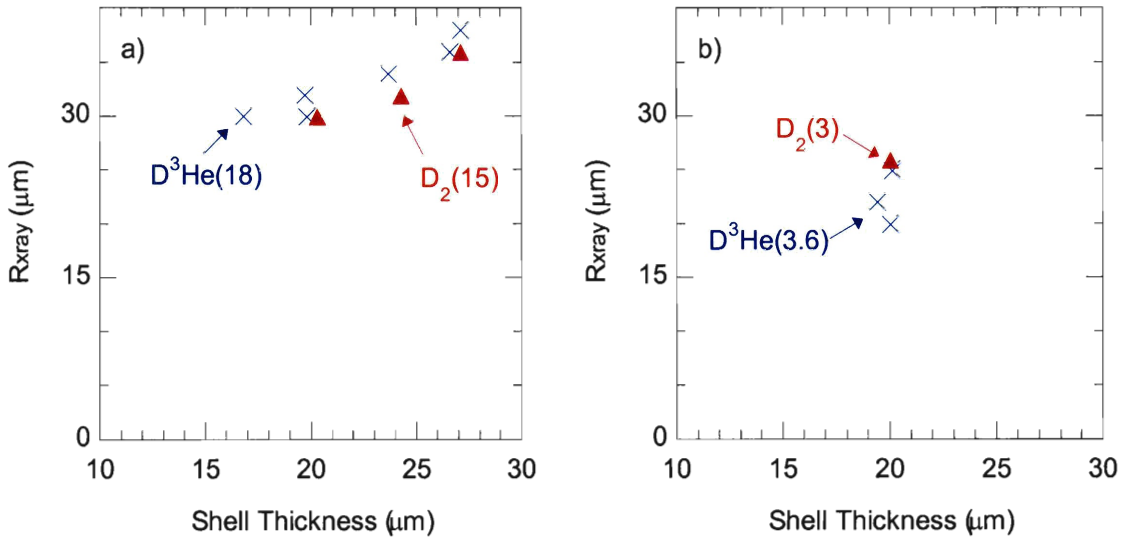

Figure A5 R_{xray} results from D_2 and D^3He gas fill capsules

FIG. A5. The fuel-shell interface estimates (R_{xray}) obtained from implosions involving D_2 gas filled capsules (solid triangle) and hydrodynamically-equivalent D^3He-gas-filled capsules (X) are in agreement for implosions involving (a) capsules with different plastic shell thicknesses (18-atm D^3He gas fill and a 15-atm D^2 gas fill), and (b) for 20-μm thick plastic-shell capsules (3.6-atm D^3He gas fill and a 3-atm D^2 gas fill). The typical measurement uncertainty for R_{xray} is ± 5 μm.

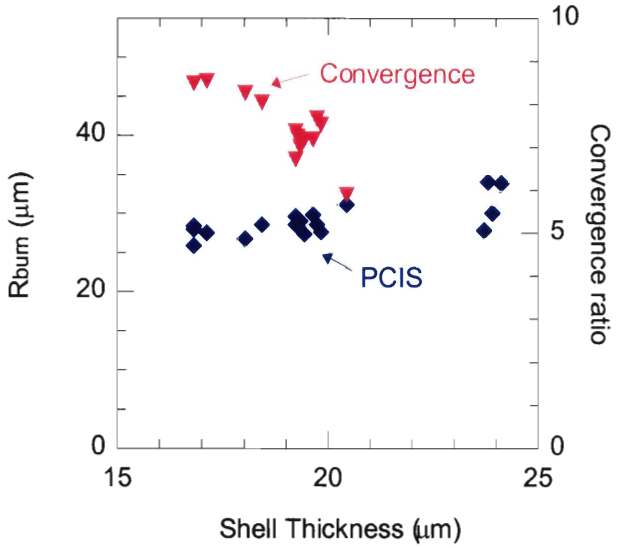

Figure A6 Convergence for plastic-shell implosions

FIG. A6. Larger burn profiles are a result of the decreasing convergence of thicker plastic-shell capsules. The calculated convergence ratios (C_r) obtained from <ρR> data as a function of the shell thickness is displayed on the secondary y-axis (triangles) ($C_r \approx \sqrt{\langle \rho R \rangle / (f(\rho R)_i)}$, where f is the fraction of shell remaining after the ablation phase, and $(\rho R)_i$ is the initial areal density.)[5] The D^3He burn size (R_{burn}, diamonds) obtained from the same implosions increases with decreasing convergence. f is calculated from the mass ablation rate,[1] and corresponds to approximately 11 μm of ablated shell material for all shell thicknesses. In ref. 5, C. K. Li *et al.* takes f ~ 1/3, based on results from planar burn-through experiments.

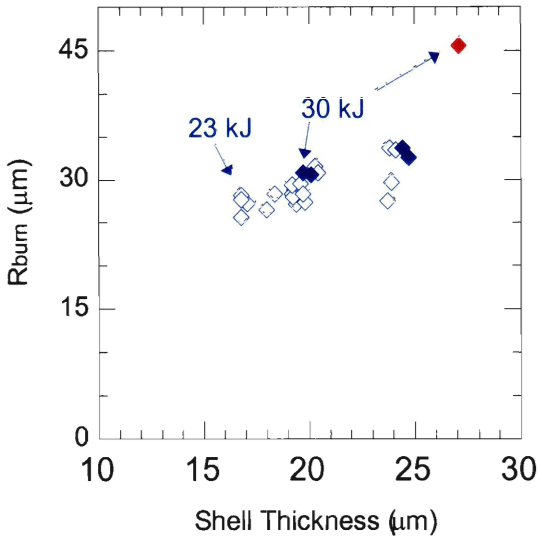

Figure A7 Burn radii obtained from CH capsules driven with 30 kJ of energy

FIG. A7. Similar D^3He burn sizes (R_{burn}) were obtained for implosions involving plastic-shell capsules driven by 23 kJ (open diamonds) and 30 kJ (solid diamonds) of laser energy. The increased laser energy was achieved by turning off the SSD drivers (a 2-D smoothing of the beams by spectral dispersion). The 27-μm red data point was generated by summing 3 consecutive implosions,[6] and may contain additional systematic errors associated with capsule positioning uncertainties for the three successive implosions. (All capsules were filled with ~ 18-atm of D^3He gas, driven by a 1-ns square pulse, and used the SG4 DPP).

Appendix B. Penumbral images made with different species of charged particles

Imaging capabilities are being developed to extend beyond the standard D^3He burn profiles obtained from D^3He gas fill capsule implosions. The detection scheme discussed in Section 2 is capable of generating penumbral images using any charged particle species that escapes from the implosion, and preliminary images have been obtained using 3-MeV DD protons, 3.6-MeV D^3He alphas, $\leq$ 14.1-MeV elastically scattered protons, and 12.6 - 17.5 MeV secondary D^3He protons. A series of representative penumbral images obtained from different implosion types is discussed here. These results are a reflection of attempts to extend the range of imaging capabilities. The setups and results from these implosions are further summarized in Appendices E and F.

Imaging thin-glass shell implosions

Penumbral images have been obtained from thin-glass implosions using 3.0-MeV DD protons, 3.6-MeV D^3He alphas, and 14.7-MeV D^3He protons. The $<\rho R>$ of these implosions was small compared to that of plastic-shell implosions. As a result, the less energetic charged particles were able to escape the capsule. (See Fig. A2 for the energy loss of D^3He protons escaping from plastic and glass-shell implosions). Penumbral images obtained using D^3He alphas, DD protons, and D^3He protons are shown in Fig. B1 for shot 38539. All three images were obtained simultaneously using the same camera; the low energy D^3He alphas and DD protons were detected on the first sheet of CR-39, while the high energy D^3He protons were detected on the second sheet of CR-39 (See Fig. 4a of Section 2).

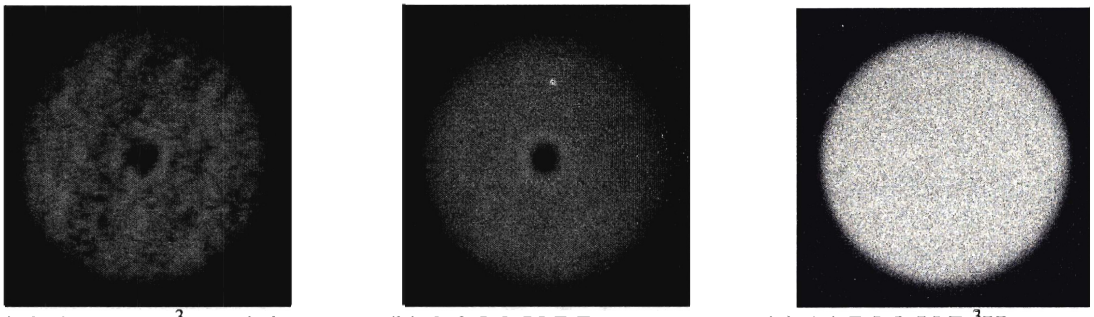

(a) 3.6-MeV D^3He alphas (b) 3.0-MeV DD protons (c) 14.7-MeV D^3He protons

Figure B1 Penumbral images using DD p, and D^3He α, and p (thin glass)

FIG. B1. Penumbral images obtained from one camera using (a) 3.6-MeV D^3He alphas, (b) 3.0-MeV DD protons, and (c) 14.7-MeV D^3He protons (shot 38539). Image distortions decrease from left to right with a decreasing time-of-flight of the detected particles. It is also important to note that the alphas have a higher atomic number.
Note: Mesh data was also obtained for this implosion.

The penumbral images shown in Fig. B1 (a) and (b) both exhibit areas of anomalously low signal in the center of the image, while the same feature is not present in image (c). Although it was shown in Section 2 that fields should not be affecting the energetic D^3He protons, weak electromagnetic fields may be present and only strong enough to alter the trajectory of the slower DD protons and D^3He alphas. These fields may be a result of low energy (< 1-MeV) ions that are ablated off of the capsule surface during the laser pulse. The observed effects increase with the time-of-flight and atomic number of the particle, resulting in the greatest amount of distortion for image (a), and the least distortion for image (c).

The observed image distortions were accompanied by an artificial broadening of the source, as illustrated by a direct comparison of R_{burn} obtained from image (a) and image (c). Since both (a) and (c) are penumbral images of the D^3He nuclear burn, separate deconvolutions should result in the same D^3He burn size. However image (a) resulted in R_{burn} = 93 μm, while image (b) resulted in R_{burn} = 62 μm (see Appendix E and F). If the types of tests discussed in Section 2 are carried out for the low energy particles,

we may be able to identify the cause of, and possible correct for, the image broadening associated with the DD protons and D^3He alphas.

Imaging the DD shock burn for thick-plastic shell implosions

Figure B2 shows penumbral images obtained from thick plastic-shell implosions using 3.0-MeV DD protons that only escape during the shock-driven burn. Images (a) and (b) correspond to implosions involving a D^3He and D_2 gas fill, respectively. Unfortunately, the statistics of the first image were very poor. The second image, however, has much better statistics and contains several interesting qualities. The ring of high detection density seen in the upper left of the image corresponds to an area of the CR-39 without a direct line of sight to the implosion; this indicates that the particles detected in this region had curved trajectories. Also, the main image was non-uniform, containing a pitted and finely striated structure. Further analysis and experiments are needed discover the physics responsible for the formation of these patterns.

(a) 37839 (b) 37134

Figure B2 Penumbral images of the DD shock burn

FIG. B2. Penumbral images of the DD shock burn from implosions of a (a) D^3He gas filled 18-μm plastic shell and (b) D_2 gas filled 20-μm plastic shell.

Imaging the shell of thick-plastic shell implosions

Penumbral images have been obtained for the first time using elastically scattered (knock-on) protons. These knock-on protons are primarily generated in the compressed

shell material when 14.1-MeV DT neutrons collide with ambient plasma ions. Although this penumbral imaging technique does not directly image the nuclear burn, it may provide valuable insights into the size of the DT burn and the distribution of the shell. From conservation of momentum and energy, the most energetic protons are forward scattered while the lower energy protons are scattered at large angles, as illustrated in Fig. B3a. (The observed spectra of the knock-on protons are rather broad, with a peak energy of 14.1-MeV.)[7] Images obtained using the highest energy knock-on protons would best reflect the size of the burn, while images obtained using the lower energy protons would favorably image the extent of the shell material. Our first attempts at imaging the shell resulted in the penumbral image shown in Fig. B3b. As reported in Appendix F, the preliminary results are suggestive of both a hollow source for the low energy knock-on protons (Fig. B3c) and a centrally peaked source. Future experiments will further examine these types of implosions.

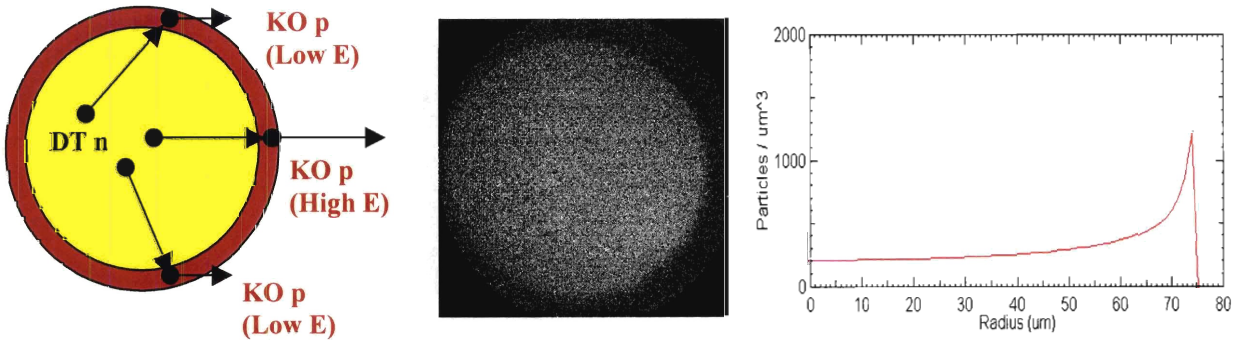

(a) (b) 37232 (c) inferred source

Figure B3 Imaging knock-on protons

FIG. B3 (a) Diagram illustrating knock-on protons (KO p) resulting from elastic collisions between 14.1-MeV DT neutrons and shell ions. The relative energies of the KO protons are indicated. (b) A penumbral image constructed from low energy knock-on protons (~ 3.5 MeV – 5 MeV) and (c) the corresponding reconstructed source profile are suggestive of a hollow source profile. However, the left edge of the penumbral image was lost due to camera miss pointing, therefore reducing the available statistics and increasing the uncertainty of the shape of the inferred source profile.

Imaging the secondary D^3He burn in D_2 gas fill implosions

Penumbral images have been recently obtained using energetic secondary protons generated from implosions of D_2-gas filled capsules.[8] These protons are created by two sequential reactions:

$$D + D \rightarrow n(2.45MeV) + {}^3He(0.82MeV), \tag{14}$$

followed by

$${}^3He(\leq 0.82MeV) + D \rightarrow \alpha(6.6 - 1.7MeV) + p(12.6 - 17.5MeV). \tag{15}$$

A fraction of ^{3}He ions created in reaction (14) react with D ions through reaction (15), producing secondary D^3He protons. The secondary D^3He burn images generated can be used to estimate the size of the DD burn. Figure B4 shows a penumbral image obtained from shot 37134, involving a D_2 gas filled 20-μm plastic shell. The shape of the reconstructed burn profile was not well defined because of poor statistics; sample results are presented in Appendix F.

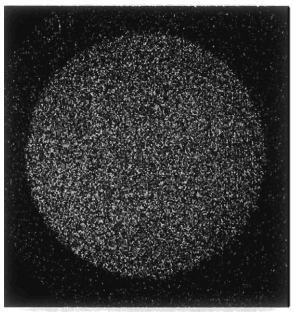

37134

Figure B4 Penumbral image obtained using secondary D^3He protons

FIG. B4. Penumbral image of the secondary D^3He burn from implosion 37134, involving a D_2-gas filled 20-μm plastic-shell implosion.

Appendix C. Extracting data from CR-39

For proton-emission imaging to be successful, charged particles must be efficiently and accurately detected. The CR-39 nuclear track detectors have proven very useful for this purpose, and are routinely used to record the location of hundreds of thousands of protons from a single implosion. The basic technique for extracting the required information is outlined here; a detailed description is presented elsewhere.[9]

The nuclear track detectors are sheets of CR-39 plastic ($C_{12}H_{18}O_7$) that undergo localized damage when a charged particle passes through. The damage sites are in the form of broken molecular bonds and free radicals. After exposure to the charged particles, the plastic is etched in a 6 molar sodium hydroxide solution, which acts to enlarge the damage sites. The size of each damage site, or track, is proportional to the energy deposited by the charged particle, as well as the etch duration. After etching, the tracks are large enough to be examined with the aid of a microscope. Examples of etched tracks are shown in Fig. C1a and c, where magnified surface images of CR-39 are shown.

When the particles are incident normal to the CR-39 surface, as in these experiments, the resultant tracks are circular. If incidence is not perpendicular, then the tracks will be elliptical. In order to extract information about the incident particles, software has been developed to record the position, size, optical contrast, and eccentricity of every track located in the exposed CR-39 surface. As shown in Fig. C1b, these parameters may be used to isolate signal tracks from intrinsic CR-39 background and also to distinguish between different types of particles. The position of each track is recorded to within an accuracy of approximately 0.2 μm.

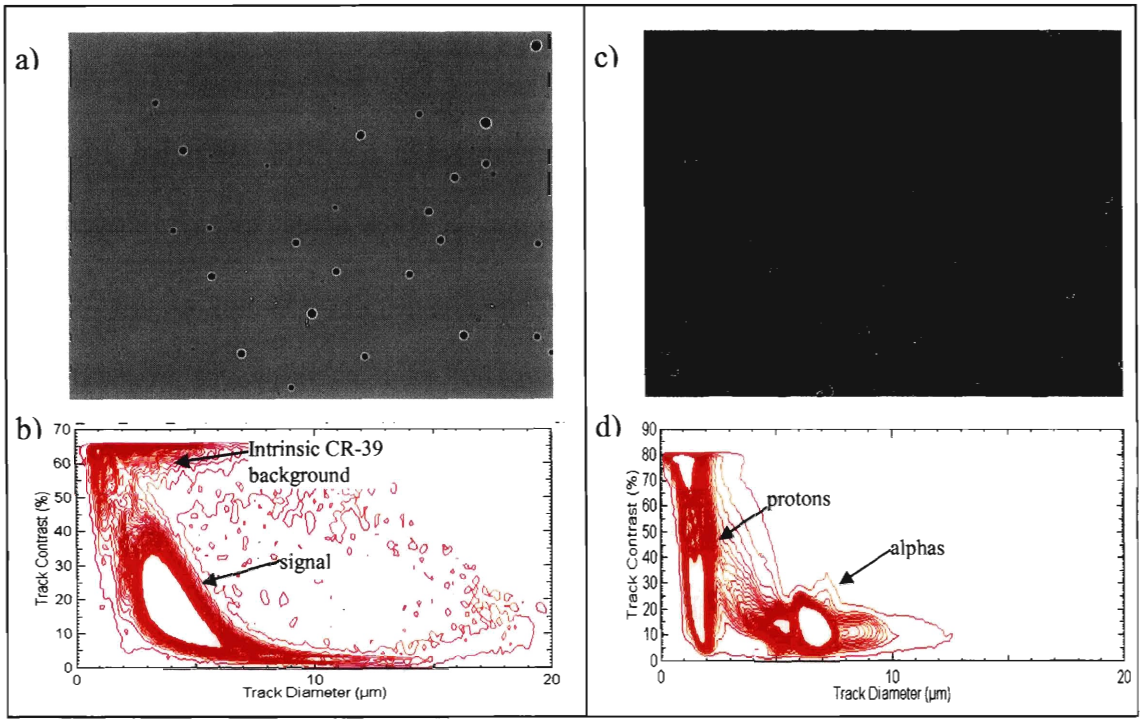

Figure C1 Extracting data from the CR-39 nuclear track detectors

FIG. C1. Different track diameters are seen in the surface images of CR-39 from a D^3He gas filled (a) 20-μm plastic-shell implosion 38036, and (c) thin-glass implosion 38539. (Image dimensions are ~ 300 x 230 μm.) After characterizing all the tracks in the signal area (~ 15 cm^2), a contour plot of the number of tracks vs. optical contrast and track diameter is generated for each case. (b) Tracks from 14.7-MeV D^3He protons are isolated from the intrinsic CR-39 background by examining tracks larger than 2 μm in diameter and less than 50% in contrast. (d) Tracks from DD protons (0.8 – 2.6 μm diameter) and D^3He alphas (5 – 8 μm diameters and < 30% contrast) are present. Also, DD triton tracks may possibly be present at ~ 5 μm. The CR-39 from shot 38036 was etched for 6 hrs, and the CR-39 from shot 38539 was etched for 1.5 hrs. Note that "Track Contrast" as plotted is defined as 100% - the optical contrast.

Proper filtering is required to reduce the energy of incident particles down to levels that result in efficient detection by the CR-39, as discussed in Section 2. For a given type of particle, lower incident energies (down to ~ 1 MeV) result in larger diameter tracks with lower optical contrast. Since the CR-39 intrinsic background is typically characterized by very small diameter tracks with low optical contrast, proper filtering is selected to produce distinguished signal tracks, as shown in Fig. C1b.

Sample filter assignments for different implosions and particle species are presented in Appendix G. These figures can be used as a reference for future experiments. An example of insufficient filtering is included to illustrate how signal tracks might overlap with the intrinsic CR-39 background.

For the case of D^3He-proton emission imaging experiments, the CR-39 is placed a known distance behind the imaging aperture, as shown in Section 2 (Fig. 2). In these experiments, the critical information extracted from the CR-39 is the location of incidence for each D^3He proton. The cumulative D^3He-proton detection locations make up the penumbral image, such as the one shown in Section 2 (Fig. 5). The penumbral image may then be deconvolved to generate the 2-D surface brightness image of the source, or the radial burn profile.

Appendix D. Future work and unsolved problems

Comparison to simulations and neutron-emission images

The reconstructed burn profiles are essential for examining the integrated effects of implosion dynamics. We have demonstrated the fidelity of the burn profiles, and their dependence on processes such as fuel-shell mix and capsule convergence. The next steps will be to compare the measured burn profiles to results from 2-D and 3-D simulations, and to experimental neutron-emission images.[10,11]

Expansion of imaging capabilities beyond the primary D^3He protons

The vast majority of the burn profiles have been generated using primary D^3He protons, although we are working towards expanding the scope of implosion types that can be examined using the penumbral imaging technique previously discussed.

The first images recently have been obtained using DT knock-on protons. The penumbral image obtained from shot 37232, presented in Appendix B, was generated using the low energy knock-on protons, and can be used to estimate the extent of the compressed shell during the period of neutron production. Although the results were suggestive of a hollow source, the data were not conclusive. Future experiments will need to adjust the filter assignments and geometric magnification in order to optimize the quality of the penumbral image. (For future experiments, when large numbers of DT neutrons are produced, tantalum filters should be implemented to reduce neutron-induced noise in the CR-39.)[12]

The first penumbral images of the secondary D^3He burn have also been recently obtained. Future experiments will explore the secondary D^3He burn characteristics, which may then be used to infer properties of the primary DD burn.

Anomalous Images

The anomalous penumbral images associated with low energy charged particles require further examination. As was shown in Fig B1 and Fig B2 of Appendix B, the images obtained using 3.0-MeV DD protons and 3.6-MeV D^3He alphas were more susceptible to distortion than images obtained using 14.7-MeV protons. Future experiments, exploiting the increased sensitivity of these particles, may reveal the underlying cause.

Discrepancy in the image magnification

The observed radius of the penumbral image is slightly larger than the expected size based on the camera geometry. As shown in the Fig. D1, the expected radius of the penumbral image should be at R = 1.35 cm, which would correspond to a geometrically determined source magnification of M_g = 12.5x. However, the measured radius of the penumbral image was actually at R = 1.43 cm. The observed radius could be used to infer a source magnification of M_i = 13.3x. The percent difference of the inferred magnification to the geometric magnification is shown in Fig. D1b for a collection of ~ 100 images. Images generated using 500-μm apertures are shown to exhibit a larger discrepancy than those obtained using 2000-μm apertures. (The uncertainties in the camera dimensions are typically < 0.1 cm, and do not account for the observed discrepancies.)

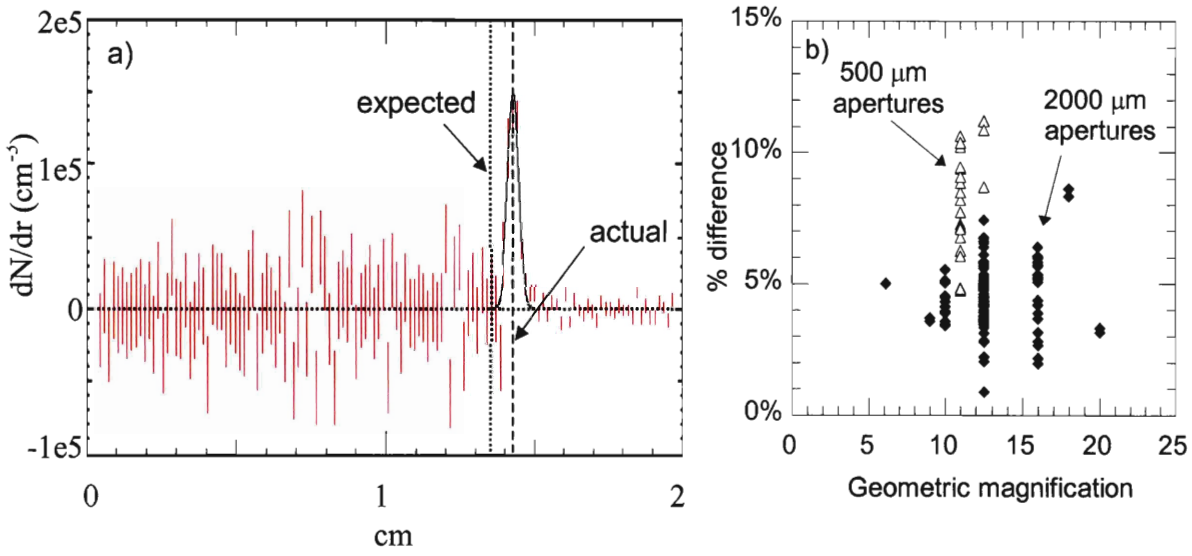

Figure D1 Image magnification discrepancy

FIG. D1. (a) The observed radius of the penumbral image is slightly larger than expected. (shot 38029, TIM2). Shown is the radial derivative (dN/dr) of the azimuthally averaged detected proton density as a function of detector radius (R). Based on a 12.5x geometric source magnification (M_g) and a 0.1 cm radius aperture (r_a), the center of the penumbra should be at $R = r_a(M_g+1) = 1.35$ cm (vertical dotted line); instead, it was at $R = 1.43$ cm (vertical dashed line), corresponding to a magnification of 13.3x. (b) The percent difference of the inferred magnification to geometric magnification is shown for numerous experiments involving both 500-μm diameter apertures (open triangles) and 2000-μm diameter apertures (solid diamonds). The smaller apertures are associated with a larger discrepancy.

An experiment has also been completed examining this magnification discrepancy for various species of particles. Three separate penumbral images were simultaneously obtained from a thin-glass implosion (shot 38539) using the 3.6-MeV D^3He alpha particles, 3.0-MeV DD protons, and 14.7-MeV D^3He protons. As shown in Fig. D2, the inferred magnification was different for the three images, which were obtained by the same camera with the same system geometry. Also interesting is that the discrepancy in magnification is larger for the slower particles, suggestive of possible field or scatter effects. Future experiments and calculations will examine this magnification discrepancy.

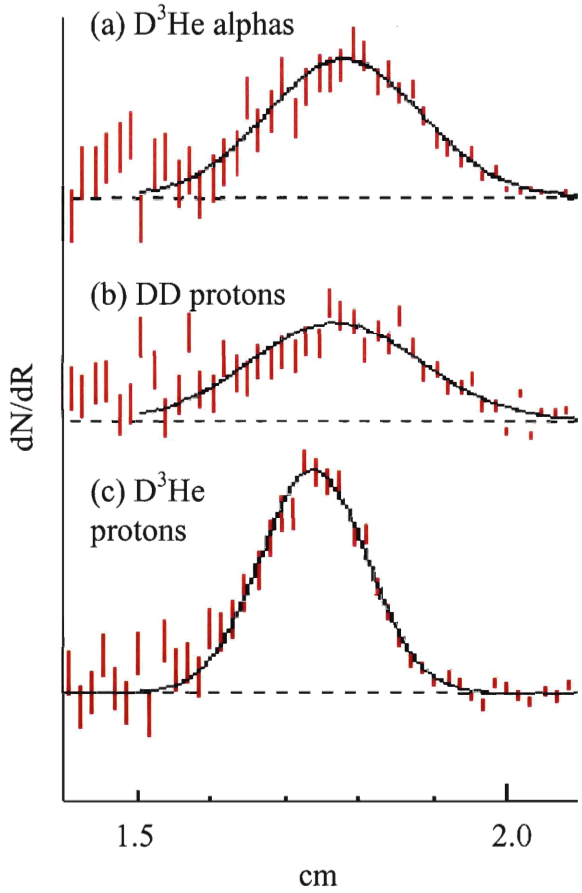

Figure D2 The observed image magnification for three different particles

FIG. D2. The difference between the inferred magnification (M_i) and the geometric magnification (M_g) is greater for less energetic particles. The radial derivative (dN/dr) of the azimuthally averaged detected proton density as a function of detector radius (R) obtained using (a) 3.6-MeV D^3He alphas, (b) 3.0-MeV DD protons, and (c) 14.7-MeV D^3He protons from shot 38539. The center of the penumbra were at R = 1.78, 1.77, and 1.74 cm respectively, corresponding to M_i = 16.7x, 16.6x, and 16.3x. The camera was positioned with a 16x geometric magnification. The three particle species were detected simultaneously with the same imaging camera.

It should be pointed out that all analyses presented in this paper have been carried out using the geometrically determined magnification and not the magnification inferred from the radius of the penumbral image (M_i). As was shown in Section 2, this technique produced consistent results for a wide range of system geometries including changes in the aperture diameter, the distance from the implosion to the aperture, and the distance from the aperture to the detector. This suggests that the source of the observed

discrepancy in the radius of the penumbral image may not be associated with image broadening.

Asymmetric penumbral regions

The penumbral data frequently exhibit asymmetric penumbras, such as the one shown in Fig. D3. As shown in the figure, two separate regions (A and B) have been called out. The data in region A is steeper than the data in region B. For a symmetric implosion, the penumbral should be radially symmetric about the peak value. The cause of the asymmetry has not yet been isolated. We believe that this asymmetry, the magnification differences mentioned above, and the anomalously low signal areas seen in the center of the thin-glass shell penumbral images may all be interrelated. As mentioned previously, the ions that are ablated from the capsule surface during the laser pulse may be generating fields strong enough to cause such effect. Future experiments and calculations should be performed to examine this possibility.

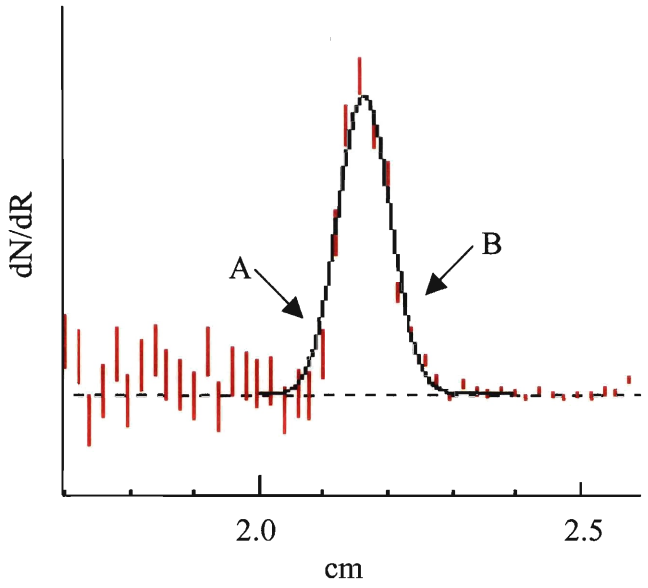

Figure D3 An asymmetric penumbra

FIG. D3. The penumbral image from shot 36730 is asymmetric. As shown, region A is steeper than region B.

Non-uniform proton detection densities

The proton detection density should be uniform in the center of the penumbral image, which corresponds to the area on the CR-39 that is exposed to the entire proton source. Occasionally, this region is not uniform. Figure D4 shows a representative example of a non-uniform, azimuthally averaged proton density (N) as a function of the position from the center of the image. The density is expected to be flat up until the onset of the penumbral region, located at ~ 1.3 cm, but instead the density decreases with increasing radius. In addition, there is a small unexpected minima at 1.3 cm. (Figure D4 also shows some signs of an asymmetric penumbra: the transition at 1.35 cm is more abrupt than at 1.45 cm.)

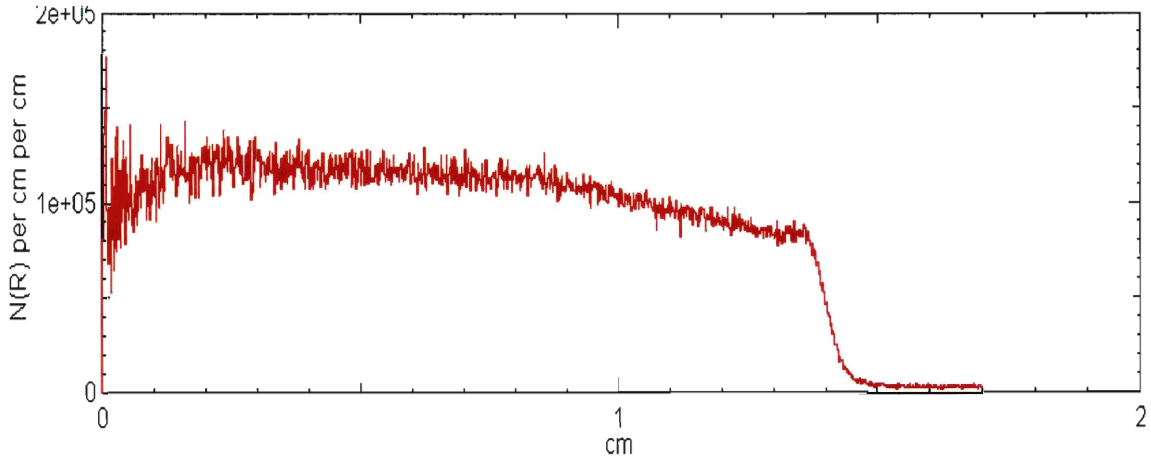

Figure D4 Non-uniform proton density

FIG. D4. The azimuthally averaged proton detection density as a function of the radius from the center of the image. The data was taken from shot 36723, CR-39 P53. In the region from R = 0 cm to R = 1.3 cm, the proton density is larger for smaller radii than for larger radii.

Software updates

Future improvements will be made to the analysis software used to generate the reconstructed burn profiles. Currently, the software takes an 360 degree azimuthal average of the proton detection density on the CR-39. However, more selective software

would be extremely useful when a penumbral image includes localized areas that should be omitted from the analysis. A specific example where analysis would be greatly improved is for the DT knock-proton penumbral image shown in Fig. B3b and in Appendix F (shot 37232). In this case the left edge of the image was lost for radii > 2.25 cm; this required that all of the data at R > 2.25 cm be excluded from the analysis. New analysis software would allow us to include roughly 80% of the image for R > 2.25 cm., greatly increasing the available statistics for a proper source reconstruction.

Imaging the shock and compression burn using D^3He protons

Future experiments will attempt to individually image the D^3He shock and compression burn profiles for 27-μm thick plastic-shell capsule implosions. The contrast versus diameter plot for shot 37646 (Appendix G) illustrates a clear separation in track diameters for the shock and compression protons. Currently. the system is limited by the available statistics, and reconstructing two separate burn profiles is not possible. However, by replacing the aperture with a specially designed grid, the camera sensitivity will be greatly increased,[13] and this experiment may be possible.

This page intentionally left blank

Appendix E. Compilation of experimental results

A table summarizing the proton-emission imaging experiments is included here for reference. The experiments were first sorted by the phase plates used (SG4 or SG3). The standard D^3H proton penumbral images were then sorted by shell thickness, and finally by fill pressure. Penumbral images obtained using particles other than the primary D^3He protons were placed and the end. The SG3 experiments were sorted in a similar fashion, except for the glass shell data, which was placed on the same page as the SG4 glass data. All data presented in this document were processed using the digital-camera scanning system (expect for CR-39 C134, shot 26081).

Phase Plates	Shell thickness and type	Gas fill (atm)	Other
SG4	17 μm thick CH shells	D^3He(18 and 20)	
SG4	18 μm thick CH shells	D^3He(20)	
SG4	18 μm thick CH shells	D^3He(10)	
SG4	19 μm thick CH shells	D^3He(16.5)	
SG4	20 μm thick CH shells	D^3He(18)	
SG4	20 μm thick CH shells	D^3He(3.6)	
SG4	24 μm thick CH shells	D^3He(18)	
SG4	24 μm thick CH shells	D^3He(16.5)	
SG4	27 μm thick CH shells	D^3He(18)	
SG4	20, 24, and 27 μm CH	D^3He(18)	30 kJ, SSD off
SG4	20, and 24 μm CH	D_2(15 and 20)	2^{ndary} D^3He protons
SG4	20, 24, and 27 μm CH	DT(15)	Knock-on protons
SG4	20 μm thick CH shells	D^3He(various)	Camera mispointing
SG4	17, and 20 μm CH	D^3He(18 and 20)	Asymmetric drive
SG4	2, 3, and 9 μm SiO2	D^3He(18 and 20)	DD & D^3He particles
SG3	2, and 3 μm SiO2	D^3He(18) and D_2(15)	DD & D^3He particles
SG3	20 μm thick CH shells	D^3He(18)	
SG3	20 μm CH with Ti layer	D^3He(18)	
SG3	24 and 27 μm CH	D^3He(18)	
SG3	20 μm thick CH shells	D_2(15)	2^{ndary} D^3He protons

Definition of headings

Date	Date of the experiment
Shot #	OMEGA shot number
Capsule parameters	Gas fill (pressure in atm), shell type [thickness in μm], and capsule diameter (μm) (additional notes have been included for some implosions)
Laser pulse shape	Nominal shape of the laser pulse sg1018 is a 1-ns square pulse alpha 402 is a 400-ps shaped pulse alpha 501 is a 500-ps shaped pulse alpha 501p is a 500-ps shaped pulse with a picket SDD off: no smoothing by spectral dispersion (SSD)
Laser energy	Total measured laser energy delivered to the capsule (kJ)
Geo. Mag	Magnification of the source (from camera geometry)
CR-39 to TCC	Distance from target chamber center to detector pack (cm)
nTOF Y_{DD}	The DD yield (x 10^{10}) (measured with the neutron time-of-flight systems)
nTOF Ti	Neutron-burn averaged ion temperature (measured with the neutron time-of-flight systems)
WRF Y_{D3HE}	The D^3He yield (x 10^8), measured by proton spectrometers
Aperture Diameter & ID	Aperture diameter (μm) and identification
Port #	Location of the camera on the OMEGA target chamber
1st Filter	The first layer in the detector pack (thickness in μm) Al: Aluminum filter Ta: Tantalum filter My: Mylar filter
2nd CR-39 ID	The second layer in the detector pack (CR-39 with the identification number)
CR-39 width	Thickness (μm) of previously mentioned CR-39
Y_{DD} or Y_{D3He}	Yield (x 10^8) obtained from the reconstructed burn profile (corresponds to DD shock yield if 1st filter ≤25 μm, and the total D^3He yield if the 1st filter > 25 μm.)
R_{burn}	R_{burn} (μm) extracted from the penumbral image (corresponds to the second layer of detector pack) (from DD shock profile if 1st filter ≤25 μm, and D^3He profile if the 1st filter > 25 μm.)
3rd Filter	The third layer in the detector pack (thickness in μm) Al: Aluminum filter Ta: Tantalum filter My: Mylar filter
4th CR-39 ID	The forth layer in the detector pack (CR-39 with the identification number)
Y_{D3He}	Yield (x 10^8) obtained from the reconstructed burn profile
R_{burn}	D^3He R_{burn} extracted from the penumbral image (4th layer)

Date	Shot #	Capsule parameters: Gas (atm), shell wall (μm), diameter (μm)	Laser Pulse Shape	Laser Energy (kJ)	Geo. Mag	CR-39 to TCC (cm)	nTOF Y_{DD} (xe10)	nTOF T_i (keV)
17 μm CH shells (SG4 phase plates)								
05/06/04	36020	D2(6.6)3He(13.4)CH[17.1] 852	sg1018	18.0	12.5 12.5 12.5	39.6 39.6 39.6	1.17	3.8
05/06/04	36021	D2(6.6)3He(13.4)CH[16.8] 849	sg1018	18.9	12.5 12.5 12.5	39.6 39.6 39.6	1.16	4.3
07/08/04	36723	D2(6)3He(12)CH[16.8] 868.6	sg1018	22.7	12.5 12.5 12.5	39.6 39.6 39.6	2.12	4.8
07/08/04	36730	D2(6)3He(12)CH[16.8] 868.6	sg1018	22.0	12.5 12.5 20	39.6 39.6 61.5	2.02	4.4
18 μm CH shells (SG4 phase plates)								
10/26/04	37839	D2(6.3)3He(13.7)CH[18.4] 853	sg1018	20.8	16 16	49.8 49.8	1.31	3.6
10/26/04	37840	D2(6.3)3He(13.7)CH[18] 850	sg1018	20.9	16 16	49.8 49.8	1.26	3.6
18 μm CH shells, with a 10 atm fill (SG4 phase plates)								
10/26/04	37842	D2(3.3)3He(6.7)CH[18.3]	sg1018	21.1	12.5 12.5	39.6 39.6	0.99	4.9
10/26/04	37844	D2(3.3)3He(6.7)CH[18.4] 854	sg1018	20.8	12.5 12.5	39.6 39.6	0.97	4.9
19 μm CH shells (SG4 phase plates)								
06/24/04	36583	D2(10.5)3He(6)CH[19.3] 859.6	sg1018	22.6	12.5	39.6	8.68	4.0
06/24/04	36584	D2(10.5)3He(6)CH[19.4] 857.8	sg1018	22.7	12.5	39.6	8.30	4.0
06/24/04	36585	D2(10.5)3He(6)CH[19.2] 858.4	sg1018	22.6	12.5	39.6	8.76	4.2
06/24/04	36586	D2(10.5)3He(6)CH[19.2] 860.4	sg1018	22.4	12.5	39.6	7.83	3.7
06/24/04	36587	D2(10.5)3He(6)CH[19.2] 852.4	sg1018	22.5	12.5	39.6	8.10	4.1
20 μm CH shells (SG4 phase plates)								
02/12/04	35004	D2(6)3He(12)CH[19.6] 877.2	sg1018	22.7	6.1 9	38.6 36.8	1.55	4.3
02/23/04	35168	D2(6)3He(12)CH[19.8] 880.6 SSD Off	sg1018 SSD off	22.0	10 10	36.5 36.5	1.01	4.9
02/23/04	35176	D2(6)3He(12)CH[19.7] 871.4	sg1018	21.1	10 10	36.5 36.5	1.05	5.1
10/06/04	37642	D2(6)3He(12)CH[20.3] 877.6	sg1018	22.9	16 16	49.8 49.8	1.05	4.9
11/09/04	37987	D2(6)3He(12)CH[20.1] 854.2	sg1018	23.0	16 16	49.8 49.8	1.23	3.7
11/09/04	37995	D2(6)3He(12)CH[20.3] 855.6	sg1018	22.8	16	49.8	1.30	4.9
11/11/04	38035	D2(6)3He(12)CH[20] 853	sg1018	22.7	12.5	39.6	1.66	3.8
11/11/04	38036	D2(6)3He(12)CH[20.4] 858	sg1018	23.0	12.5	39.6	1.35	3.9

Shot #	WRF Y_{D3He} (xE8)	Aperture Diameter & ID (μm)	port #	1st Filter (μm)	2nd CR-39 ID	CR39 width (μm)	$Y_{DD\ or}$ Y_{D3He} (xe8)	R_{burn}	3rd Filter (μm)	4th CR-39 ID	Y_{D3He} (xe8)	R_{burn}
36020	6.55	2008 T2-43	3	200 Al	P4	1062			50 Al	P11	4.65	26.7
		2007 T2-44	4	200 Al	P7	1060			50 Al	P13	3.48	30.6
		2009 T2-45	5	200 Al	P30	1055			50 Al	P14	4.73	25.1
36021	6.71	2003 T2-47	3	200 Al	P31	1063			50 Al	P17	4.66	25.4
		2000 T2-48	4	200 Al	P34	1066			50 Al	P20	3.59	26.3
		2004 T2-49	5	200 Al	P38	1021			50 Al	P21	4.51	29.0
36723	--	2000 T2-51	2	200 Al	P53	1093	16.6	30.1	25 Al	P70	14.1	28.0
		2001 T2-52	3	200 Al	P98	1110	13.8	26.0	25 Al	P90	15.3	26.2
		5x600 13	4	200 Al	P56	1041	16.2	30.4	25 Al	P88	16.7	29.5
36730	--	2005 T2-53	2	200 Al	P68	1117	15	29.5	25 Al	P81	12.5	28.2
		2001 T2-54	3	200 Al	P32	1095	15.6	26.7	25 Al	P87	14.9	28.0
		2000 T2-55	4	200 Al	P96	1084	13.2	27.2	25 Al	P57	14.1	28.2
37839	4.75	2007 T2-42	3	7.5 Ta	3P18	1092			200 Al	3P36	5.01	26.8
		1998 T2-70	6	7.5 Ta	3P67	1068			200 Al	3P69		30.2
37840	5.81	2011 T2-77_1	3	200 Al	3P35	1092			12.5 Al	3P84	3.31	24.5
		2003 T2-47	6	200 Al	3P59	1055			12.5 Al	3P33	4.47	29.0
37842	6.97	2010 T2-1b	3	200 Al	1P49	1034			25 Al	1P21	4.2	24.8
		2000 T2-3b	6	200 Al	1P73	1034			25 Al	1P101	5.07	26.8
37844	7.02	2000 T2-4b	3	200 Al	1P67	1031			25 Al	1P81	5.46	23.0
		2000 T2-6b	6	200 Al	1P53	1036			25 Al	1P40	3.53	23.1
36583	10.00	2000 T2-35	1	200 Al	P5	1081	11.2	29.1	none	P10	10.7	28.9
36584	9.98	1995 T2-36	1	200 Al	P6	1079	11.8	27.4	none	P19	11.4	27.4
36585	14.30	5X625 2.2	1	200 Al	P15	1083	16.7	28.3	none	P73	16	28.8
36586	14.00	2010 T2-37	1	200 Al	P16	1090	9.6	28.0	none	P75	9.2	28.6
36587	11.30	2013 T2-38	1	200 Al	P36	1089	10.1	29.9	none	P82	10.7	29.3
35004	9.71	2006 T2-5	3	104 Al	PD2	1052	6.54	28.2	20 Ta	PD60	6.67	31.1
		2002 T2-10	4	104 Al	PD4	1052	8.39	29.2	20 Ta	PD58	3.72	27.6
35168	5.62	1996 T2-3	3	175 Al	CC247	1043	4.32	26.3	25 Al	PD44	3.38	27.8
		2001 T2-4	4	175 Al	PD30	1030	4.77	27.3	25 Al	PD19	4.67	29.1
35176	5.57	2000 T2-14	3	175 Al	PD10	1046	4.27	25.9	25 Al	PD31	4.36	27.8
		2000 T2-15	4	175 Al	PD9	1055	4.21	31.1	25 Al	PD54	3.63	29.5
37642	4.72	2007 T2-53	2	200 Al	3P31	1086			10 Al	3P21	3.32	31.0
		1999 T2-57	4	200 Al	3P71	1085	4.36	30.9	10 Al	3P25	3.16	33.3
37987	5.69	2002 T2-22b	3	200 Al	3P10	1048	--	--	10 Al	3P50	--	--
		2001 T2-11b2	4	--	none	--	--	--	850 Al	3P97	--	--
37995	5.53	2014 T2-16b	3	200 Al	3P90	1040	--	--	10 Al	3P108	--	--
38035	7.43	2002 T2-33b	2	--	none	--	--	--	850 Al	1P142	6.1	24.9
38036	8.12	2001 T2-12	2	200 Al	1P28	1081			10 Al	1P42	8	31.0

Date	Shot #	Capsule parameters: Gas (atm), shell wall (μm), diameter (μm)	Laser Pulse Shape	Laser Energy (kJ)	Geo. Mag	CR-39 to TCC (cm)	nTOF Y_{DD} (xe10)	nTOF T_i (keV)
20 μm CH shells, with a 3.6 atm fill (SG4 phase plates)								
02/23/04	35167	D2(1.2)3He(2.4)CH[19.4] 869 SSD Off	sg1018 SSD Off	22.5	10 10	36.5 36.5	0.29	5.4
02/23/04	35170	D2(1.2)3He(2.4)CH[19.9] 873	sg1018	21.2	10 10	36.5 36.5	0.30	4.8
07/21/04	36875	D2(1.2)3He(2.4)CH[20] 854	sg1018	22.6	12.5	39.6	0.26	5.2
07/21/04	36876	D2(1.2)3He(2.4)CH[20] 856	sg1018	22.8	12.5	39.6	0.22	5.7
10/06/04	37635	D2(1.2)3He(2.4)CH[20.1] 857	sg1018	22.9	12.5	39.6	0.18	4.0
11/11/04	38029	D2(1.2)3He(2.4)CH[20] 860	sg1018	22.5	12.5	39.6	0.31	3.5
11/11/04	38030	D2(1.2)3He(2.4)CH[20.1] 857	sg1018	22.7	12.5	39.6	0.33	3.5
11/11/04	38031	D2(1.2)3He(2.4)CH[19.4] 860	sg1018	22.3	12.5	39.6	0.41	3.6
24 μm CH shells (SG4 phase plates)								
10/06/04	37643	D2(6)3He(12)CH[23.9] 860.8	sg1018	23.0	12.5 12.5	39.6 39.6	0.46	4.5
10/06/04	37645	D2(6)3He(12)CH[23.8] 880.6	sg1018	22.6	12.5 12.5	39.6 39.6	0.41	3.9
11/11/04	38032	D2(6)3He(12)CH[24.1] 857	sg1018	23.0	12.5	39.6	0.61	4.3
11/11/04	38033	D2(6)3He(12)CH[23.7] 880	sg1018	22.6	12.5	39.6	0.61	3.1
01/11/05	38525	D2(6)3He(12)CH[24] 855	sg1018	22.1	12.5	39.6	0.62	3.7
24 μm CH shells, with altered gas ratio (SG4 phase plates)								
01/11/05	38527	D2(10.5)3He(6)CH[24.3] 869.6	sg1018	22.5	12.5	39.6	3.00	3.6
01/11/05	38528	D2(10.5)3He(6)CH[24.3] 868.6	sg1018	22.6	12.5	39.6	3.13	3.1
27 μm CH shells (SG4 phase plates)								
10/06/04	37646	D2(6)3He(12)CH[26.6] 875.2	sg1018	22.9	12.5 12.5	39.6 39.6	0.24	2.6
10/06/04	37648	D2(6)3He(12)CH[27.6] 861.2	sg1018	22.9	12.5 12.5	39.6 39.6	0.22	3.2
30 kJ of laser energy, with SSD off (SG4 phase plates)								
07/21/04	36883	D2(6)3He(12)CH[19.8] 851.6	sg1018 SSD off	30.4	16 16	49.8 49.8	1.02	4.1
07/21/04	36885	D2(6)3He(12)CH[19.7] 857.4	sg1018 SSD off	30.1	16 16	49.8 49.8	1.22	4.8
07/21/04	36886	D2(6)3He(12)CH[24.7] 865.4	sg1018 SSD off	30.1	12.5	39.6	0.65	4.1
07/21/04	36887	D2(6)3He(12)CH[24.4] 870.8	sg1018 SSD off	29.8	12.5	39.6	0.76	4.8
07/21/04	36888	D2(6)3He(12)CH[27.1] 864.2	sg1018 SSD off	30.2	12.5	39.6	0.31	3.5
07/21/04	36889	D2(6)3He(12)CH[27] 861	sg1018 SSD off	29.3	12.5	39.6	0.33	4.3
07/21/04	36890	D2(6)3He(12)CH[27.1] 862.2	sg1018 SSD off	30.0	12.5	39.6	0.36	5.0

Shot #	WRF Y_{D3He} (xE8)	Aperture Diameter & ID (μm)	port #	1st Filter (μm)	2nd CR-39 ID	CR39 width (μm)	$Y_{DD\ or}$ Y_{D3He} (xe8)	R_{burn}	3rd Filter (μm)	4th CR-39 ID	Y_{D3He} (xe8)	R_{burn}
35167	2.25	2000 T2-1	3	175 Al	CC243	1045	1.45	22.3	25 Al	PD49	1.19	22.4
		1998 T2-2	4	175 Al	PD3	1055	1.56	19.3	25 Al	PD18	1.58	24.0
35170	2.38	1996 T2-11	3	175 Al	CC252	1054	1.45	24.8	25 Al	PD50	1.28	23.7
		2003 T2-13	4	175 Al	PD26	1038	0.855	27.5	25 Al	PD11	1.23	27.0
36875	2.80	1999 T2-71	4	200 Al	3P4	967	1.67	24.2	none	P92	1.49	23.5
36876	3.12	1998 T2-72	4	200 Al	3P5	1016	2.93	17.4	none	P84	1.69	18.3
37635	1.35	2008 T2-41	4	200 Al	3P83	1066			10 Al	3P13	0.86	26.2
38029	1.98	2010 T2-2b	2	200 Al	1P93	1063			10 Al	1P141	1.4	20.6
38030	2.51	2007 T2-46	2	200 Al	1P148	1077			10 Al	1P160	2.3	20.7
38031	2.17	2007 T2-35b	2	200 Al	1P124	988			10 Al	1P82	2	22.7
37643	1.89	2002 T2-64	2	150 Al	3P34	1090			25 Al	3P16	1.33	29.3
		2005 T2-65	4	150 Al	3P30	1084	1.87	29.3	25 Al	3P14	1.84	31.3
37645	0.99	2004 T2-66	2	150 Al	3P70	1079			25 Al	3P9	0.94	34.8
		2002 T2-67	4	150 Al	3P12	1029			25 Al	3P27	0.78	32.9
38032	1.53	2001 T2-24	2	150 Al	1P34	1076			10 Al	1P147	1.4	33.7
38033	1.36	2000 T2-25	2	150 Al	1P99	1066			10 Al	1P51	0.9	27.8
38525	1.93	2003 T2-36c	1	150 Al	1P140	1006			25 Al	1P154		
38527	2.60	2005 T2-39c	1	150 Al	1P29	1074			25 Al	1P56		
38528	3.49	2001 T2-15b	1	150 Al	1P88	1056			25 Al	1P25		
37646	0.43	2003 T2-68	2	150 Al	3P41	1019			25 Al	3P76		
		2001 T2-69	4	150 Al	3P47	1027			25 Al	3P52		
37648	0.57	sum	2	sum	sum	sum	sum	sum	sum	sum	sum	sum
		sum	4	sum	sum	sum	sum	sum	sum	sum	sum	sum
36883	9.48	1993 T2-81	2	200 Al	P60	1038	7.11	30.6	none	P91	7.08	31.1
		1998 T2-74	4	200 Al	P78	1193	6.28	31.8	none	P83	5.6	29.7
36885	9.51	1992 T2-82	2	200 Al	P55	1045	6.59	28.3	none	P79	3.82	35.8
		1994 T2-83	4	200 Al	P45	1076	7.32	30.7	none	P76	7.42	29.1
36886	2.36	1997 T2-75	2	150 Al	P99	1085	2.91	32.7	12.5 Al	P77	2.8	32.7
		2002 T2-76	4	150 Al	P69	1100	3.29	33.3	12.5 Al	P72	3.18	32.3
36887	4.80	1994 T2-77_2	2	150 Al	P95	1100	4.72	34.4	12.5 Al	P67	4.8	34.0
		1995 T2-80	4	150 Al	P62	1033		--	12.5 Al	P85	4.06	33.4
36888	1.32	1995 T2-84	2	150 Al	P54	1100	3.29	48.6	12.5 Al	P71	3.52	50.4
		1992 T2-85	4	150 Al	P94	1033	3.95	42.5	12.5 Al	P93	3.86	41.2
36889	0.94	sum	2	sum	sum	sum	sum	sum	sum	sum	sum	sum
		sum	4	sum	sum	sum	sum	sum	sum	sum	sum	sum
36890	1.40	sum	2	sum	sum	sum	sum	sum	sum	sum	sum	sum
		sum	4	sum	sum	sum	sum	sum	sum	sum	sum	sum

Date	Shot #	Capsule parameters: Gas (atm), shell wall (μm), diameter (μm)	Laser Pulse Shape	Laser Energy (kJ)	Geo. Mag	CR-39 to TCC (cm)	nTOF Y_{DD} (xe10)	nTOF T_i (keV)
D2 fills (SG4 phase plates)								
01/15/04	34683	D2(15)CH[19.5] 883	alpha402	15.4	11	36.2	1.46	3.3
01/15/04	34684	D2(15)CH[19.6] 877.2	alpha402	16.6	11	36.2	2.35	3.7
01/15/04	34685	D2(15)CH[19.8] 872.6	alpha402	16.3	11	36.2	2.16	3.2
01/15/04	34686	D2(15)CH[19.2] 877.4	sg1018	18.8	11	36.2	14.90	4.1
01/15/04	34688	D2(15)CH[19.1] 949.2	sg1018	20.6	10	36.5	17.80	4.0
01/15/04	34689	D2(15)CH[20.2] 941.4	sg1018	22.1	10	36.5	15.20	3.9
01/15/04	34690	D2(15)CH[24.5] 873	sg1018	22.4	11	36.2	7.39	3.3
01/15/04	34691	D2(15)CH[24.8] 862.6	sg1018	22.4	11	36.2	6.02	3.9
01/15/04	34692	D2(15)CH[24.5] 870	sg1018	19.8	11	36.2	5.29	3.4
06/17/04	36509	D2(15)CH[25.9] 867.9	alpha501	18.2	12.5	39.6	2.48	3.0
07/08/04	36731	D2(20)CH[20.4] 869.8 (incorrect fill pressure)	sg1018	22.6	12.5 12.5 12.5	39.6 39.6 39.6	13.50	4.9
07/08/04	36732	D2(20)CH[20.4] 874.8 (incorrect fill pressure)	sg1018	22.3	12.5 12.5 12.5	39.6 39.6 39.6	16.80	3.6
08/12/04	37134	DD(15)CH[19.6] 856.2	sg1018	23.4	12.5	39.6	16.20	3.8
DT fills (SG4 phase plates)							(Y_{DT})	
08/12/04	37135	DT(15)CH[19] 873	sg1018	23.3	16	49.8	1730	--
08/19/04	37229	DT(15)CH[27.2] 863.4	sg1018	23.2	16	49.8	26.10	--
08/19/04	37230	DT(15)CH[27.7] 862.4	sg1018	23.8	16	49.8	8.66	--
08/19/04	37231	DT(15)CH[26.9] 867.8	sg1018	23.7	16	49.8	33.50	--
08/19/04	37232	DT(15)CH[19] 864	sg1018	23.3	19	49.8	167.00	--
08/19/04	37233	DT(15)CH[24.7] 867.4	sg1018	23.6	16	49.8	70.90	--
20 μm CH shells, with variable fills - miss pointed (SG4 phase plates)								
11/09/04	37988	D2(3.3)3He(16.4)CH[19.7] 867	sg1018	22.6	12.5	39.6	0.45	4.9
11/09/04	37989	D2(3.3)3He(16.3)CH[19.8] 870	sg1018	22.7	12.5 12.5	39.6 39.6	0.59	4.6
11/09/04	37990	D2(3.3)3He(16.3)CH[19.9] 869	sg1018	22.3	12.5	39.6	0.59	4.6
11/09/04	37991	D2(3.1)3He(16.3)CH[19.7] 867	sg1018	22.6	12.5	39.6	0.55	4.7
11/09/04	37992	D2(0.75)3He(19.8)CH[19.7] 872	sg1018	22.5	12.5	39.6	0.04	4.8
11/09/04	37993	D2(0.75)3He(19)CH[19.5] 871	sg1018	22.7	12.5	39.6	0.04	4.2
11/09/04	37994	D2(0.75)3He(19.6)CH[19.8] 871	sg1018	23.0	12.5	39.6	0.04	4.7
11/09/04	37995	D2(6)3He(12)CH[20.3] 855.6	sg1018 sg1018	22.8	16 16	49.8 49.8	1.30	4.9
11/09/04	37996	D2(0.75)3He(19)CH[20.2] 869	sg1018	22.2	12.5	39.6	0.37	5.1

Shot #	WRF Y_{D3He} (xE8)	Aperture Diameter & ID (μm)	port #	1st Filter (μm)	2nd CR-39 ID	CR39 width (μm)	$Y_{DD\ or}$ Y_{D3He} (xe8)	R_{burn}	3rd Filter (μm)	4th CR-39 ID	Y_{D3He} (xe8)	R_{burn}
34683	0.18	1000 3-9	2	5 Ta	CC166	1060			none	CC167		
34684	0.22	1000 3-8	2	10 Ta	CC170	1066	1.89	75.0	none	CC168		
34685	0.28	sum	2	sum	sum	sum	sum	sum	sum	sum	sum	sum
34686	2.56	1000 3-3	2	5 Ta	CC175	1065	4.47	177.0	none	CC169		
34688	3.95	2000 4-10	2	5 Ta	CC177	1075	14.4	175.0	none	CC173		
34689	3.03	sum	2	sum	sum	sum	sum	sum	sum	sum	sum	sum
34690	0.88	1000 3-2	2	5 Ta	CC187	1074			none	CC172		
34691	0.63	sum	2	sum	sum	sum	sum	sum	sum	sum	sum	sum
34692	0.71	sum	2	sum	sum	sum	sum	sum	sum	sum	sum	sum
36509	--	2012 T2-19	2	10 Al	P61	1021			50 Al	P74		
36731	--	2002 T2-61	2	10 Al	P58	1045		--	50 Al	P64		--
		2007 T2-62	3	10 Al	P59	1049		--	50 Al	P65		--
		2005 T2-63	4	10 Al	P8	1083		--	50 Al	P66		--
36732	--	sum	2	sum	sum	sum	sum	sum	sum	sum	sum	sum
		sum	3	sum	sum	sum	sum	sum	sum	sum	sum	sum
		sum	4	sum	sum	sum	sum	sum	sum	sum	sum	sum
37134	3.30	2004 T2-39	6	12.5 Al	3P37	1008			50 Al	3P80	1.8	~27.5

37135	13.20	2008 T2-40	6	50 Al	3A3	492		--	100 Al	3P28		--
37229	0.25	1996 T2-58	6	50 Al	3A8	483		--	100 Al	3P15		--
37230	0.06	2003 T2-59	6	100 Al	3P61	986		--	100 Al	3P20		--
37231	0.38	2004 T2-60	6	150 Al	3P73	993		--	100 Al	3P26		--
37232	21.00	2000 T2-56	6	100 Al	3P22	1101		--	100 Al	3P24		--
37233	0.60	2007 T2-50	6	50 Al	3A4	459		--	100 Al	3P1		--

37988	3.35	1997 T2-23b	3	200 Al	1P64	1016	--	--	10 Al	1P146	--	--
37989	3.36	2001 T2-24b	3	200 Al	1P78	1026	--	--	10 Al	1P43	--	--
		2004 T2-31b	4	50 Al	1P9	1048	--	--	150 Al	1P96	--	--
37990	3.54	2008 T2-26b	4	200 Al	1P71	1036	--	--	10 Al	1P22	--	--
37991	4.76	2005 T2-27b	4	200 Al	1P84	1037	--	--	10 Al	1P155	--	--
37992	1.19	2006 T2-28b	4	200 Al	1P109	1040	--	--	10 Al	1P119	--	--
37993	1.15	2005 T2-30b	4	200 Al	1P54	1041	--	--	10 Al	1P7	--	--
37994	1.44	2005 T2-32b	4	200 Al	1P83	1030	--	--	10 Al	1P11	--	--
37995	5.53	2014 T2-16b	3	200 Al	3P90	1040	--	--	10 Al	3P108	--	--
		2001 T2-18b	4	200 Al	3P102	1055	--	--	10 Al	3P56	--	--
37996	1.80	2007 T2-29b	4	200 Al	1P77	1029	--	--	10 Al	1P39	--	--

Date	Shot #	Capsule parameters: Gas (atm), shell wall (μm), diameter (μm)	Laser Pulse Shape	Laser Energy (kJ)	Geo. Mag	CR-39 to TCC (cm)	nTOF Y_{DD} (xe10)	nTOF T_i (keV)
Asymmetrically driven implosions (SG4 phase plates)								
02/12/04	35005	D2(6)3He(12)CH[19.6] 880.2 100 micron capsule offset (TIM 3 & 5 are at ~79?)	sg1018	23.0	9 9 5.2	36.8 36.8 39.5	0.86	4.8
02/12/04	35006	D2(6.7)3He(13.3)CH[17.2] 855 Prolate with TIM 4 as a pole (TIM 3 & 5 are at ~79?)	sg1018	18.7	9 9 5.2	36.8 36.8 39.5	0.16	5.7
02/23/04	35172	D2(6.7)3He(13.3)CH[16.9] 857 Prolate with TIM 4 as a pole (TIM 3 & 5 are at ~79?)	sg1018	17.5	10 10 10	36.5 36.5 36.5	0.37	3.4
02/23/04	35173	D2(6.7)3He(13.3)CH[16.7] 852 Prolate with TIM 4 as a pole (TIM 3 & 5 are at ~79?)	sg1018	17.4	10 10 10	36.5 36.5 36.5	0.37	4.9
02/23/04	35174	D2(6.7)3He(13.3)CH[16.9] 854 Oblate	sg1018	18.3	10 10 10	36.5 36.5 36.5	0.74	5.1
02/23/04	35175	D2(6)3He(12)CH[19.5] 874 150 micron capsule offset (TIM 3 & 5 are at ~79?)	sg1018	21.9	10 10 10	36.5 36.5 36.5	0.28	4.3
05/06/04	36023	D2(6.6)3He(13.4)CH[16.9] 849 Prolate with TIM 4 as a pole (TIM 3 & 5 are at ~79?)	sg1018	18.0	12.5 12.5 12.5	39.6 39.6 39.6	0.32	3.5
05/06/04	36025	D2(6.6)3He(13.4)CH[17.2] 855 Prolate with TIM 4 as a pole (TIM 3 & 5 are at ~79?)	sg1018	18.5	12.5 12.5 12.5	39.6 39.6 39.6	0.32	4.4
05/06/04	36026	D2(6.6)3He(13.4)CH[17.1] 850 Prolate with TIM 4 as a pole (TIM 3 & 5 are at ~79?)	sg1018	18.4	12.5 12.5 12.5	39.6 39.6 39.6	0.35	4.3
05/06/04	36028	D2(6.6)3He(13.4)CH[16.9] 851 Oblate	sg1018	18.7	12.5 12.5 12.5	39.6 39.6 39.6	0.57	4.2
01/11/05	38535	D2(6.7)3He(13.3)CH[16.2] 853 Prolate with TIM 4 as a pole	sg1018	18.3	12.5 12.5 12.5	39.6 39.6 39.6	0.51	3.8
01/11/05	38537	D2(6.7)3He(13.3)CH[16.4] 848 Prolate with TIM 4 as a pole	sg1018	18.6	12.5 12.5 12.5	39.6 39.6 39.6	0.58	5.2
01/11/05	38538	D2(6.7)3He(13.3)CH[16.4] 844 1/2 prolate TIM 4 as a pole	sg1018	--	12.5 12.5 12.5	39.6 39.6 39.6	1.00	5.0

Shot #	WRF Y_{D3He} (xE8)	Aperture Diameter & ID (μm)	port #	1st Filter (μm)	2nd CR-39 ID	CR39 width (μm)	$Y_{DD\ or}$ Y_{D3He} (xe8)	R_{burn}	3rd Filter (μm)	4th CR-39 ID	Y_{D3He} (xe8)	R_{burn}
35005	11.90	2002 T2-7	3	104 Al	PD15	1056		--	20 Ta	PD52		--
		2002 T2-8	4	104 Al	PD20	1052		--	20 Ta	PD47		--
		2000 T2-9	5	104 Al	PD24	1050		--	20 Ta	PD43		--
35006	1.41	2000 4-7	3	104 Al	PD27	1049		--	20 Ta	PD42		--
		2000 4-8	4	104 Al	PD28	1048		--	20 Ta	PD37		--
		2000 4-9	5	104 Al	PD1	1046		--	20 Ta	PD35		--
35172	0.93	2000 4-1	3	200 Al	PD40	1048		--	50 Al	PD32		--
		2000 4-2	4	200 Al	PD45	1061		--	50 Al	PD41		--
		2000 4-4	5	200 Al	PD25	1040		--	50 Al	PD36		--
35173	1.34	sum	3	sum	sum	sum	sum	sum	sum	sum	sum	sum
		sum	4	sum	sum	sum	sum	sum	sum	sum	sum	sum
		sum	5	sum	sum	sum	sum	sum	sum	sum	sum	sum
35174	3.66	2000 T2-16	3	200 Al	PD56	1033		--	50 Al	PD46		--
		2000 T2-17	4	200 Al	CC244	1046		--	50 Al	PD39		--
		2000 T2-18	5	200 Al	PD29	1040		--	50 Al	PD22		--
35175	1.50	2000 T2-23	3	200 Al	PD8	1058		--	50 Al	PD55		--
		2000 T2-26	4	200 Al	PD21	1053		--	50 Al	PD34		--
		2000 T2-27	5	200 Al	PD7	1058		--	50 Al	PD17		--
36023	1.95	1993 T2-20	3	250 Al	P41	1035		--	25 Al	P22		--
		2000 T2-21	4	250 Al	P43	1018		--	25 Al	P23		--
		1996 T2-22	5	250 Al	P44	1061		--	25 Al	P24		--
36025	1.69	1998 T2-28	3	250 Al	P46	1019		--	25 Al	P25		--
		1993 T2-29	4	250 Al	P47	1054		--	25 Al	P26		--
		1997 T2-31	5	250 Al	P48	1049		--	25 Al	P35		--
36026	1.95	sum	3	sum	sum	sum	sum	sum	sum	sum	sum	sum
		sum	4	sum	sum	sum	sum	sum	sum	sum	sum	sum
		sum	5	sum	sum	sum	sum	sum	sum	sum	sum	sum
36028	4.21	1997 T2-32	3	250 Al	P49	1051		--	25 Al	P37		--
		2008 T2-33	4	250 Al	P52	1059		--	25 Al	P40		--
		1996 T2-34	5	250 Al	P12	1061		--	25 Al	P51		--
38535		2000 T2-26c	1	275 Al	1P70	1031		--	12.5 Al	1P150		--
		2000 T2-27c	2	275 Al	1P131	1018		--	12.5 Al	1P102		--
		2000 T2-30c	4	275 Al	1P158	1082		--	12.5 Al	1P87		--
38537		1998 T2-31c	1	275 Al	1P65	1015		--	12.5 Al	1P106		--
		2001 T2-32c	2	275 Al	1P118	1049		--	12.5 Al	1P6		--
		2002 T2-33c	4	275 Al	1P126	1011		--	12.5 Al	1P27		--
38538		1998 T2-34c	1	275 Al	1P132	1024		--	12.5 Al	1P91		--
		1990 T2-35c	2	275 Al	1P44	1009		--	12.5 Al	1P92		--
		2004 T2-37c	4	275 Al	1P76	1027		--	12.5 Al	1P1		--

Date	Shot #	Capsule parameters: Gas (atm), shell wall (μm), diameter (μm)	Laser Pulse Shape	Laser Energy (kJ)	Geo. Mag	CR-39 to TCC (cm)	nTOF Y_{DD} (xe10)	nTOF T_i (keV)
Glass shell implosions (SG4 phase plates)								
10/26/04	37845	D2(6.3)3He(13.7)SiO2[9] 815	sg1018	23.2	12.5 12.5	39.6 39.6	0.32	3.7
11/09/04	37984	D2(6)3He(12)SiO2[2.5] 868 miss pointed	sg1018	9.1	18 18 18	61.8 61.8 61.8	0.67	7.3
11/09/04	37985	D2(6)3He(12)SiO2[2.5] 876 miss pointed	sg1018	9.3	18 18 18	61.8 61.8 61.8	0.64	8.2
11/09/04	37986	D2(6)3He(12)SiO2[2.6] 877.2 miss pointed	sg1018	9.1	18 18 18	61.8 61.8 61.8	7.17	7.0
01/11/05	38539	D2(6)3He(12)SiO2[2] 861 grids for TIM1 and 2 20 beams	sg1018	8.9	16 16 16	39.6 39.6 39.6	0.53	12.3
02/17/05	38928	D3He(18)SiO2[2.8] 856	sg1018	10.0	16 16	49.8 49.8	0.24	7.9
Glass shell implosions (SG3 phase plates)								
01/30/02	26081	D2(6)3He(12)SiO2[1.9] 926.8	sg1018	23.0	11	36.2	3.63	10.8
01/31/02	26105	D2(6)3He(12)SiO2[2] 929	sg1018	22.2	11	36.2	3.96	12.8
01/31/02	26106	D2(6)3He(12)SiO2[2.2] 940.4	sg1018	22.4	11	36.2	5.30	13.6
05/22/02	27456	D2(6)3He(12)SiO2[1.8] 942.6	sg1018	12.0	8	37.3	5.88	9.8
05/22/02	27488	D2(6)3He(12)SiO2[2.3] 941.6	sg1018	5.3	8	37.3	0.50	3.9
06/27/02	27814	D2(6)3He(12)SiO2[2.3] 947.6	sg1018	8.4	10	36.5	2.24	6.0
06/27/02	27815	D2(6)3He(12)SiO2[2.1] 915.2	sg1018	6.1	10	36.5	0.87	7.1
06/27/02	27817	D2(15)SiO2[2.1] 904.2	sg1018	21.5	10	36.5	19.10	8.4
06/27/02	27819	D2(15)SiO2[2.1] 924.2	sg1018	21.7	10	36.5	19.40	10.7
12/05/02	29827	D2(6)3He(12)SiO2 [2.7] 928.4	ps400	8.8	11	36.2	0.58	7.2
12/05/02	29828	D2(6)3He(12)SiO2 [2.6] 917.2	ps400	9.4	11	36.2	1.17	7.3
12/05/02	29830	D2(6)3He(12)SiO2 [2.7] 911.4	ps400	10.4	11	36.2	1.69	5.4

Shot #	WRF Y_{D3He} (xE8)	Aperture Diameter & ID (μm)	port #	1st Filter (μm)	2nd CR-39 ID	CR39 width (μm)	$Y_{DD\ or}$ Y_{D3He} (xe8)	R_{burn}	3rd Filter (μm)	4th CR-39 ID	Y_{D3He} (xe8)	R_{burn}
37845	0.71	2000 T2-7b	3	200 Al	1P85	1037			25 Al	1P30		--
		2000 T2-9b	6	200 Al	1P74	1025			25 Al	1P35	0.67	27.3
37984	19.00	5x600 #14	2	5 Ta	3P23	1087	34.4	66.9	300 Al	3P7	21.5	36.2
		2000 T2-5b	3	5 Ta	3P42	1029	--	--	300 Al	3P74	--	--
		2005 T2-10b	4	7.5 Ta	3P79	1045	--	--	300 Al	3P49	--	--
37985		2000 T2-11b	2	5 Ta	3P44	1016	--	--	300 Al	3P32	--	--
		2002 T2-12b	3	5 Ta	3P54	1037	--	--	300 Al	3P3	--	--
		1999 T2-13b	4	9 Ta	3P45	1000	--	--	300 Al	3P65	--	--
37986		2001 T2-17b	2	5 Ta	3P43	1028	--	--	300 Al	3P75	--	--
		2000 T2-19b	3	7.5 Ta	3P8	1004	--	--	300 Al	3P64	--	--
		2008 T2-21b	4	5 Ta	3P82	1059	--	--	300 Al	3P62	--	--
38539		grid	1	900&950 Al		--	--	--	--	1P41	--	--
		grid & T2-11b	2	5 Ta	RM243	1500	--	--	35 Al	1P86	--	--
		T2-28c 2008	4	5 Ta	3P77	1018	295	126.0	350 Al	3P19	58	62.3
					3P77	alphas	220	93.0				
38928		reused	2	900&950 Al		--	--	--	--	3P29	--	--
		T2-40c 2000	4	5 Ta	3P51	1011			300 Al	3P6		37.8

26081	230.00	600 2-1	1	3 Al	C5	1150	--	--	300Al	C134	289	76.3
26105	267.00	25 #1	1	3 Al	C6	1140	--	--	150 Al	C195	--	--
26106	345.00	25 #2	1	3 Al	C13	1155	--	--	150 Al	C198	--	--
27456	162.00	4x600 1-12	1	10 Al	BB485	1135	290	126.0	300Al	BB484	235	50.6
					BB485	alphas	228	95.0				
27488	1.79	4x600 1-13	1	10 Al	BB490	1125	605	51.0	360 Al	BB486	1.7	34.4
27814	12.90	4x600 2.9	1	10 Al	BB615	1159	560	~50	360 Al	BB638	12.4	35.2
27815	3.00	4x600 2.11	1	10 Al	BB673	1161		~45.2	364 Al	BB682	2.32	31.1
27817	0.30	4x600 2.12	1	20 Al	BB523	1149			364 Al	BB697		--
27819	0.31	4x600 2.15	1	20 Al	BB677	1158			364 Al	BB687		--
29827	11.70	5x600 2-7-b	1	25 Al	BB547	1149	33	53.1	360 Al	BB772	9.07	52.4
29828	33.50	5x600 2-9-b	1	25 Al	BB544	1154			360 Al	BB773	17.5	57.9
29830	40.30	2000 4-3	1	25 Al	BB549	1143	71	~60	360 Al	BB786	23.7	47.3

Date	Shot #	Capsule parameters: Gas (atm), shell wall (μm), diameter (μm)	Laser Pulse Shape	Laser Energy (kJ)	Geo. Mag	CR-39 to TCC (cm)	nTOF Y_{DD} (xe10)	nTOF T_i (keV)
20 μm CH shells (SG3 phase plates)								
12/11/01	25599	D2(6)3He(12)CH[19.5] 941.8	sg1018	22.8	11	36.2	2.37	3.5
12/11/01	25600	D2(6)3He(12)CH[19.5] 934.8	sg1018	22.9	8	37.3	2.21	3.9
12/12/01	25610	D2(6)3He(12)CH[19.4] 935	sg1018	23.5	3	44.2	2.17	3.2
12/12/01	25612	D2(6)3He(12)CH[19.6] 935.2	sg1018	23.1	3	44.2	1.81	3.3
12/13/01	25634	D2(6)3He(12)CH[19.5] 934.2	sg1018	23.9	8	37.3	2.29	3.9
12/13/01	25635	D2(6)3He(12)CH[19.3] 932.2	sg1018	23.5	8	37.3	2.31	3.7
12/18/01	25664	D2(6)3He(12)CH[19.8] 938.6	sg1018	21.4	8	37.3	1.06	3.9
12/18/01	25665	D2(6)3He(12)CH[20.0] 940	sg1018	22.8	8	37.3	2.10	3.4
12/20/01	25697	D2(6)3He(12)CH[20] 942.2	sg1018	22.1	11	36.2	1.64	4.3
12/20/01	25698	D2(6)3He(12)CH[20] 933.6	sg1018	21.0	11	36.2	0.93	4.7
12/20/01	25708	D2(6)3He(12)CH[20] 932.6	sg1018	22.6	11	36.2	1.25	3.5
12/20/01	25709	D2(6)3He(12)CH[20] 934	sg1018	22.3	11	36.2	1.74	3.3
02/05/02	26157	D2(6)3He(12)CH[19] 930	sg1018	20.8	11	36.2	1.03	3.5
02/05/02	26167	D2(6)3He(12)CH[19.9] 936.8	sg1018	21.3	5	39.8	1.02	3.1
02/05/02	26168	D2(6)3He(12)CH[20.1] 934.2	sg1018	20.9	5	39.8	0.22	--
03/14/02	26624	D2(6)3He(12)Ch[19.3] 934.6	sg1018	5.2	11	36.2	dud	dud
03/14/02	26633	D2(6)3He(12)CH[19.6] 929.2	sg1018	21.6	11	36.2	1.09	4.2
06/27/02	27806	D2(6)3He(12)CH[20.1] 947.2	sg1018	22.5	10	36.5	1.58	4.2
06/27/02	27807	D2(6)3He(12)CH[20.1] 938.2	sg1018	21.8	10	36.5	1.27	4.1
06/27/02	27808	D2(6)3He(12)CH[19.9] 950.8	sg1018	22.1	10	36.5	1.32	4.3
06/27/02	27810	D2(6)3He(12)CH[20] 941	sg1018	21.8	10	36.5	1.22	4.6
06/27/02	27811	D2(6)3He(12)CH[20.4] 930.8	sg1018	22.1	10	36.5	1.42	4.5
06/27/02	27812	D2(6)3He(12)CH[19.9] 944.8	sg1018	21.9	10	36.5	1.32	4.9
06/27/02	27820	D2(6)3He(12)CH[20.2] 935.4	sg1018	21.6	10	36.5	1.32	3.9
06/27/02	27821	D2(6)3He(12)CH[19.6] 944.2	sg1018	21.1	10	36.5	1.19	4.0
09/25/02	28915	D2(6)3He(12)CH[19.7] 940.4	sg1018	19.6	10	36.5	1.33	4.1
09/25/02	28916	D2(6)3He(12)CH[20.1] 936.2	sg1018	19.4	10	36.5	1.17	2.8
09/25/02	28918	D2(6)3He(12)CH[20] 937	sg1018	19.4	10	36.5	1.07	4.4
09/25/02	28925	D2(6)3He(12)CH[19.7] 937.4	alpha501p	19.8	10	36.5	0.84	3.8
09/25/02	28929	D2(6)3He(12)CH[19.6] 933.2	alpha501p	19.7	10	36.5	0.92	4.1
09/25/02	28931	D2(6)3He(12)CH[19.6] 932.2	alpha501p	19.9	10	36.5	0.79	4.0
09/25/02	28935	D2(6)3He(12)CH[19.8] 937.6	alpha501	16.6	10	36.5	0.37	2.4
09/25/02	28936	D2(6)3He(12)CH[19.9] 943.8	alpha501	16.7	10	36.5	0.40	4.0
12/05/02	29834	D2(6)3He(12)CH[20.6] 943.2	sg1018	22.7	11	36.2	1.01	4.6
12/05/02	29835	D2(6)3He(12)CH[20.6] 935.2	sg1018	23.1	11	36.2	1.35	4.3
12/05/02	29836	D2(6)3He(12)CH[20] 945	sg1018	22.9	8	37.3	1.17	4.9
12/17/02	29954	D2(6)3He(12)CH[19.2] 943.4	sg1018	21.4	11	36.2	0.83	3.4
12/17/02	29957	D2(6)3He(12)CH[19.2] 949.4	sg1018	21.2	11	36.2	0.84	4.8
03/12/03	30956	D2(6)3He(12)CH[19.4] 942.8	sg1018	20.2	11 11	36.2 36.2	0.81	4.5
03/13/03	30977	D2(6)3He(12)CH[19.3] 946.6	sg1018	24.0	11 11	36.2 36.2	1.24	4.9

Shot #	WRF Y_{D3He} (xE8)	Aperture Diameter & ID (μm)	port #	1st Filter (μm)	2nd CR-39 ID	CR39 width (μm)	$Y_{DD\ or}$ Y_{D3He} (xe8)	R_{burn}	3rd Filter (μm)	4th CR-39 ID	Y_{D3He} (xe8)	R_{burn}
25599	7.20	1000 B	1	1.5 My	C62	1120			104 Al	C63		
25600	8.78	1000 B	1	3 Al	C68	1080			104 Al	C67		
25610	4.51	600 A	1	3 Al	C72	1140	--	--	CR-39	mulitple	--	--
25612	4.54	600 B	1	6Al	C74	1154	--	--	CR-39	C73	--	--
25634	5.50	1000 C	1	6Al	C82	1164			CR-39	C81		
25635	6.51	166	1	3 Al	C64	1130			104 Al	C61		
25664	3.39	600 C	1	3 Al	C94	1180			104 Al	C95	2.72	33.6
25665	7.97	82 600C	1	3 Al	C97	1150			104 Al	C96		
25697	--	22	1	3 Al	C106	1175			104 Al	C105		
25698	1.79	82	1	3 Al	C108	1130			104 Al	C107		
25708	5.40	163	1	3 Al	C109	1105			104 Al	C110		
25709	3.14	300	1	3 Al	C111	1157			104 Al	C112		
26157	--	600 2-2	1	3 Al	C17	1155			104 Al	C199		
26167	1.85	4x600 1-2	1	1.5 My	C58	1155			104 Al	C206		
26168	1.62	600 2-3	1	1.5 My	C143	1140			104 Al	C210		
26624	--	6002-5	1	3 Al	C144			--	104 Al	B900		--
26633	2.74	4x600 1-10	1	3 Al	C146				104 Al	B910		
27806	7.67	4x600 2.2	1	10 Al	BB613	1153			104 Al	BB611		~39.2
27807	7.00	4x600 2.5	1	10 Al	BB644	1148			104 Al	BB618		~38.2
27808	5.00	4x600 2.6	1	10 Al	BB647	1150			104 Al	BB621		~34
27810	4.00	4x600 2.7	1	10 Al	BB649	1162			104 Al	BB624		~37.8
27811	4.50	4x600 2.8	1	10 Al	BB652	1161			104 Al	BB631		~37.7
27812	3.90	sum	1	sum	sum	sum	sum	sum	sum	sum	sum	sum
27820	5.17	4x600 2.1	1	20 Al	BB532	1152			104 Al	BB653	5.47	38.9
27821	4.75	sum	1	sum	sum	sum	sum	sum	sum	sum	sum	sum
28915	4.90	4x600+ 2-14	1	25 Al	BB522	1131			104 Al	BB727	6.33	36.3
28916	4.34	sum	1	sum	sum	sum	sum	sum	sum	sum	sum	sum
28918	3.53	sum	1	sum	sum	sum	sum	sum	sum	sum	sum	sum
28925	2.60	4x600+ 2-13	1	25 Al	BB524	1132			104 Al	BB728	4.47	41.9
28929	3.35	sum	1	sum	sum	sum	sum	sum	sum	sum	sum	sum
28931	2.73	sum	1	sum	sum	sum	sum	sum	sum	sum	sum	sum
28935	0.80	4x600+ 2-4	1	25 Al	BB531	1116			104 Al	BB733	0.92	39.0
28936	1.00	sum	1	sum	sum	sum			sum	sum	sum	sum
29834	10.00	5x600 2-11-b	1	25 Al	BB571	1143			360 Al	BB791	--	--
29835	9.65	5x600 2-12-b	1	25 Al	BB580	1143			360 Al	BB796	--	--
29836	10.00	2000 4-5	1	25 Al	BB560	1146			104 Al	BB803	6.16	34.4
29954	7.00	5x600 2-3-b	1		BB552	1153			104 Al	BB805	2.86	38.3
29957	6.00	5x600 2-5-b	1		BB561	1149			104 Al	BB806	2.67	32.9
30956	7.22	5x600 s1-1	2	25 Al	BB548	1168			104 Al	BB850	2.32	31.8
		5x600 s1-10	4	25 Al	BB554	1165			104 Al	BB862	3.24	32.7
30977	15.70	5x600 s2-6	2	104 Al	BB865	1138			25 Al	BB868	5.26	31.8
		5x600 s2-10	4	25 Al	BB871	1160			104 Al	BB869	5.7	32.3

Date	Shot #	Capsule parameters: Gas (atm), shell wall (μm), diameter (μm)	Laser Pulse Shape	Laser Energy (kJ)	Geo. Mag	CR-39 to TCC (cm)	nTOF Y_{DD} (xe10)	nTOF T_i (keV)
Ti layered shells (SG3 phase plates)								
02/05/02	26158	D2(6)3He(12)CHTi[19.4]	sg1018	20.4	11	36.2	0.66	3.1
02/05/02	26161	D2(6)3He(12)CHTi[19.4] 954	sg1018	21.8	11	36.2	1.30	4.0
02/05/02	26162	D2(6)3He(12)CHTi19.5] 952.2	sg1018	22.0	11	36.2	1.58	4.3
03/14/02	26625	D2(6)3He(12)CHTi[20.2] 941.6	sg1018	22.5	11	36.2	1.24	2.7
03/14/02	26626	D2(6)3He(12)CHTi[20.1] 948.2	sg1018	22.2	11	36.2	1.49	3.4
03/14/02	26630	D2(6)3He(12)CHTi[19.8] 961.4	sg1018	22.4	11	36.2	1.66	3.4
03/14/02	26631	D2(6)3He(12)CHTi[19.7] 953.4	sg1018	21.9	11	36.2	1.57	3.4
03/14/02	26632	D2(6)3He(12)CHTi[19.1] 956.2	sg1018	22.1	11	36.2	1.68	3.8
03/14/02	26634	D2(6)3He(12)CHTi[19.5] 951	sg1018	21.4	11	36.2	1.22	4.3
03/14/02	26635	D2(6)3He(12)CHTi[19.6] 955.2	sg1018	21.7	11	36.2	1.41	4.0
03/14/02	26636	D2(6)3He(12)CHTi[20] 953	sg1018	21.2	11	36.2	1.03	4.3
03/15/02	26647	D2(6)3He(12)CHTi[19.1] 954.4	sg1018	22.1	11	36.2	1.51	4.0
03/15/02	26648	D2(6)3He(12)CHTi[19.6] 944.2	sg1018	22.3	11	36.2	1.49	3.7
03/15/02	26649	D2(6)3He(12)CHTi[19.4] 956	sg1018	22.0	11	36.2	1.29	4.1
24 and 27 μm CH shells (SG3 phase plates)								
12/12/01	25614	D2(6)3He(12)CH[24] 932	sg1018	22.9	3	44.2	0.45	3.9
12/13/01	25636	D2(6)3He(12)CH[23.7] 949.4	sg1018	23.5	8	37.3	0.79	3.3
12/13/01	25637	D2(6)3He(12)CH[23.9] 947.8	sg1018	23.4	8	37.3	0.71	3.5
12/19/01	25686	D2(8)3He(16)CH[27] 861	sg1018	13.8	8	37.3	0.08	1.7
12/19/01	25687	D2(8)3He(16)CH[27] 940.6	sg1018	18.7	8	37.3	0.17	2.2
12/19/01	25688	D2(8)3He(16)CH[27] 1053	sg1018	22.6	8	37.3	0.22	2.5
D2 fills (SG3 phase plates)								
12/11/01	25601	D2(15)CH[19.4] 934.8	alpha501	20.0	8	37.3	5.03	3.7
12/19/01	25686	D2(8)3He(16)CH[27] 861	sg1018	13.8	8	37.3	0.08	1.7
12/11/01	25605	D2(15)CH[19] 935.2	alpha501	19.4	8	37.3	3.73	3.7

Shot #	WRF Y_{D3He} (xE8)	Aperture Diameter & ID (μm)	port #	1st Filter (μm)	2nd CR-39 ID	CR39 width (μm)	$Y_{DD\ or}$ Y_{D3He} (xe8)	R_{burn}	3rd Filter (μm)	4th CR-39 ID	Y_{D3He} (xe8)	R_{burn}
26158	--	1000 3-1	1	3 Al	C22	1155			104 Al	C200		
26161	2.15	4x600 1-1	1	3 Al	C31	1140			104 Al	C204		
26162	--	4x325	1	3 Al	C52	1160			104 Al	C205		
26625	4.33	600 2-1	1	3 Al	C145				104 Al	B905		
26626	3.66	600 2-6	1	3 Al	sum	sum	sum	sum	104 Al	sum	sum	sum
26630	4.42	600 2-7	1	3 Al	sum	sum	sum	sum	104 Al	sum	sum	sum
26631	4.15	600 2-8	1	3 Al	sum	sum	sum	sum	104 Al	sum	sum	sum
26632	5.06	600 2-9	1	3 Al	sum	sum	sum	sum	104 Al	sum	sum	sum
26634	4.09	1000 3-4	1	3 Al	C153				104 Al	B914		
26635	3.44	1000 3-5	1	3 Al	sum	sum	sum	sum	104 Al	sum	sum	sum
26636	2.22	1000 3-6	1	3 Al	sum	sum	sum	sum	104 Al	sum	sum	sum
26647	5.88	600 2-10	1	3 Al	C154				104 Al	B915		~32.4
26648	5.67	4x300 1-4	1	3 Al	C155				104 Al	B916		
26649	4.64	4x600 1-11	1	3 Al	C156				104 Al	B917		

25614	1.17	1000 C	1	3 Al	C80	1130	--	--	CR-39	C78	--	--
25636	--	1000 B	1	3 Al	C88	1120			104 Al	C86	1.76	40-60
25637	--	2000 A	1	3 Al	C91	1154			104 Al	C90		
25686	--	1000	1	3 Al	C100	1135			104 Al	C99		
25687	--	1000	1	3 Al	C101	1155			104 Al	C98		
25688	0.15	1000	1	3 Al	C104	1185			104 Al	C103		

25601	very low	2000 B	1	3 Al	C69	1051	--	--	104 Al	C70	--	--
25686	--	1000	1	3 Al	C100	1135			104 Al	C99		
25605	very low	sum	1	sum	sum	sum	sum	sum	sum	sum	sum	sum

Appendix F. Representative penumbral images

Representative analyses are presented here for the various implosion types and species of detected particles. These include

D^3He gas filled capsules:

Shell thickness and type	Shot #	Particles detected	Other
17 μm thick CH shell	36730	D^3He protons	
18 μm thick CH shell	37839	D^3He protons	
19 μm thick CH shell	36584	D^3He protons	
20 μm thick CH shell	38036	D^3He protons	
20 μm thick CH shell	36876	D^3He protons	3.6 atm gas fill
20 μm thick CH shell	30977	D^3He protons	SG3
24 μm thick CH shell	37643	D^3He protons	
27 μm thick CH shell	36888-90	D^3He protons	30 kJ
18 μm thick CH shell	37839	DD shock protons	
9 μm thick SiO_2 shell	37845	D^3He protons	
2 μm thick SiO_2 shell	38539	D^3He alphas DD protons D^3He protons	
2 μm thick SiO_2 shell	27456	D^3He protons	SG3

DD gas filled capsules:

Shell thickness and type	Shot #	Particles detected	Other
20 μm thick CH shell	37134	DD shock protons Secondary D^3He protons	

DT gas filled capsules:

Shell thickness and type	Shot #	Particles detected	Other
19 μm thick CH shell	37232	DT knock-on protons	

Included with each example is the penumbral image. If the quality of the image was good, the corresponding fit to the data (dN/dR) and the reconstructed burn profile are included. For the penumbral images obtained using secondary D^3He protons and DT knock-on protons, the shape of the source profile was not well determined. In these cases, two possible profiles are shown.

Definition of headings

Shot #	OMEGA shot number
Capsule	Gas fill (pressure in atm), shell type [thickness in μm], and capsule diameter (μm)
Laser pulse shape	Nominal shape of the laser pulse sg1018 is a 1-ns square pulse 60 beams total, unless noted otherwise
Laser energy	Total measured laser energy delivered to the capsule (kJ)
Geo. Mag	Magnification of the source (from camera geometry)
WRF Y_{D3HE}	The D^3He yield (x 10^8), measured by proton spectrometers
Aperture Diameter	Aperture diameter (μm)
Diagnostic port	Location of the camera on the OMEGA target chamber
CR-39 ID	The CR-39 identification number
Filtering	The total filtering placed in front of the CR-39 (Up to three filters were used. The width is given in μm.)
Bin Size	The size of the bins used in the analysis (μm)
Observed Magnification	The magnification determined be examining location of the penumbra center (see Appendix D)
PCIS Y_{D3HE}	Yield (x 10^8) obtained from the reconstructed burn profile (and from the proton detection density)
R_{burn}	D^3He R_{burn} extracted from the penumbral image

The penumbral image presented here contain three parts: a signal area, an area of background, and sometimes an area on the CR-39 that was not scanned. The figure below refers to these three parts. Also shown is a rectangular area, from which an average proton detection density was determined. The density and the CR-39 distance from TCC were used to determine a second measurement for the proton yield.

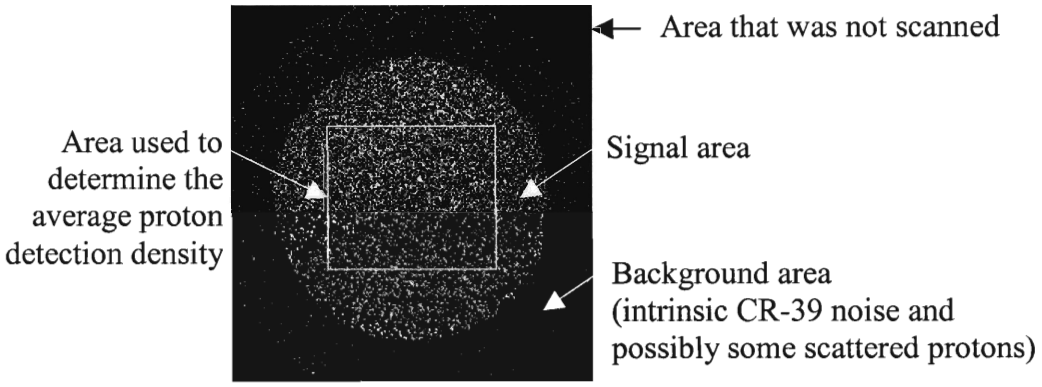

Shot #	Capsule	Laser Pulse Shape	Laser Energy (kJ)	Geo. Mag.	WRF Y_{D3He} (xE8)	Aperture Diameter (μm)
36730	D2(6)3He(12)CH[16.8]	sg1018	22.0	20	NA	2000

D^3He protons

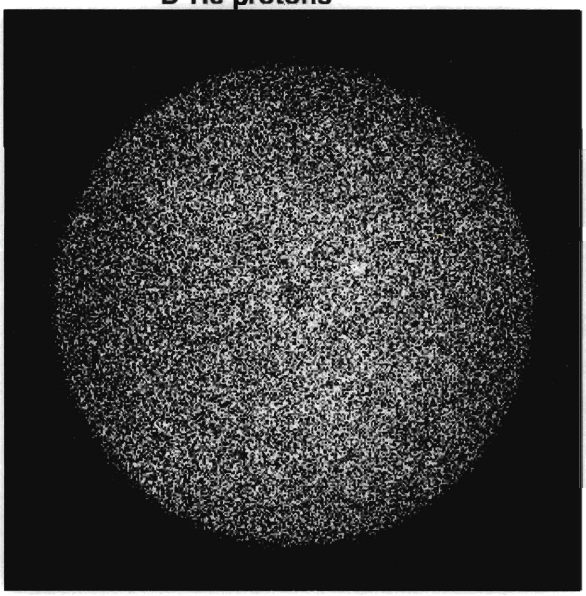

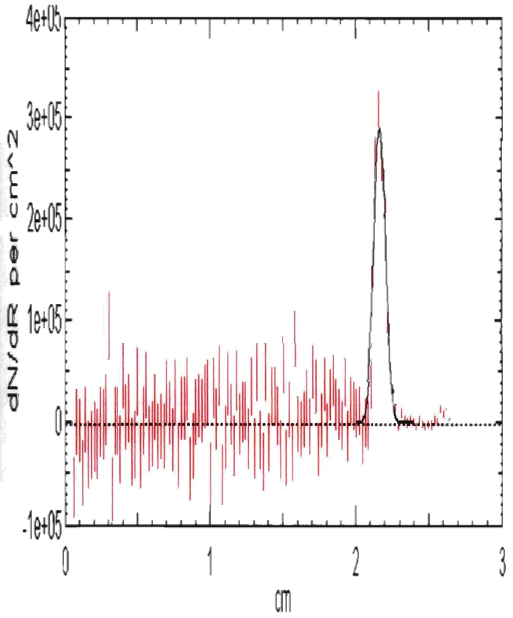

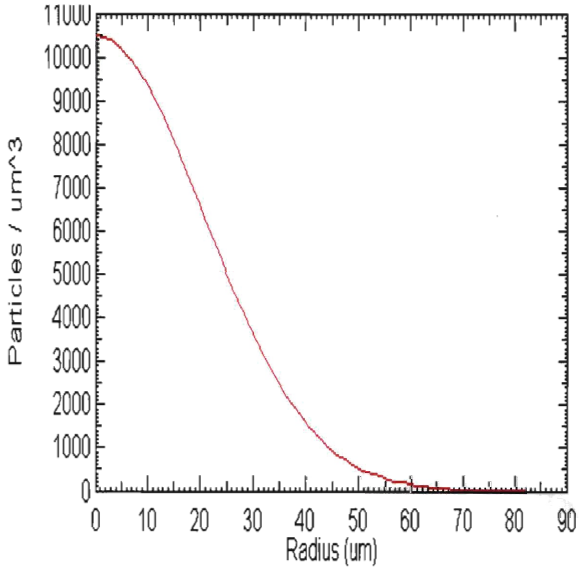

Diagnostic port:		TIM4
CR-39 ID		P57
Filtering:	first layer	200 Al
	second layer	1084 CR-39
	third layer	25 Al
Bin size (μm)		10
Observed Magnification:		20.7
PCIS Y_{D3He} (xE8)		14.1 (19.8)
R_{burn} (μm)		28.2

Note: The center of the penumbral image shows a slight decrease in the proton detection density.

Shot #	Capsule	Laser Pulse Shape	Laser Energy (kJ)	Geo. Mag.	WRF Y_{D3He} (xE8)	Aperture Diameter (μm)
37839	D2(6.3)3He(13.7)CH[18.4]	sg1018	20.8	16	4.75	2007

D^3He protons

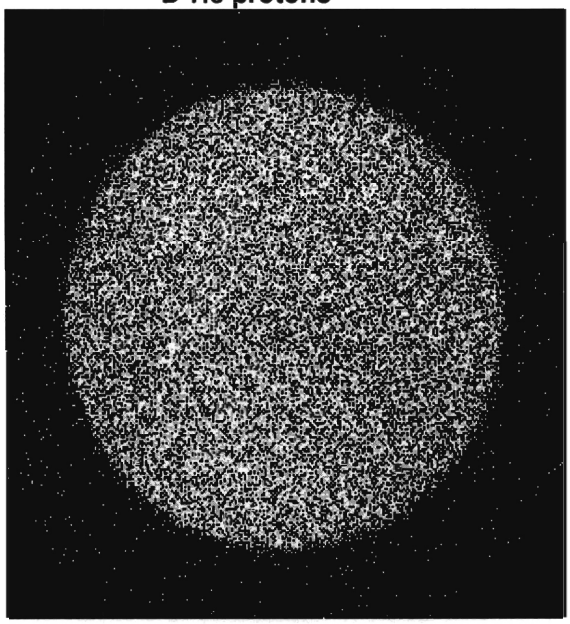

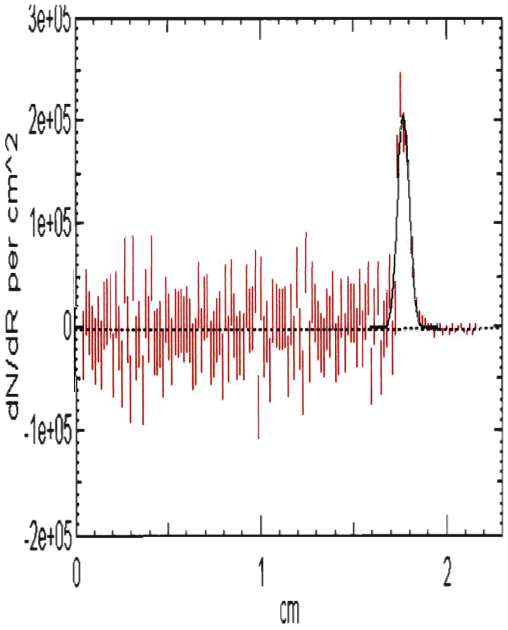

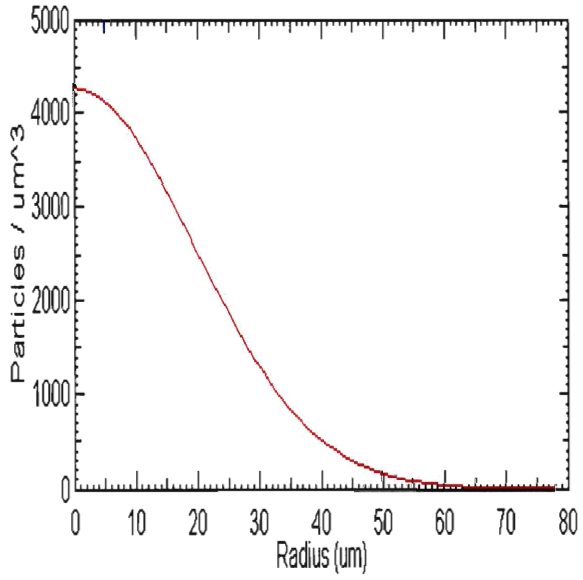

Diagnostic port:		TIM3
CR-39 ID		3P36
Filtering:	first layer	7.5 Ta
	second layer	1092 CR-39
	third layer	200 Al
Bin size (μm)		10
Observed Magnification:		16.7
PCIS Y_{D3He} (xE8)		5.0 (5.8)
R_{burn} (μm)		26.8

Shot #	Capsule	Laser Pulse Shape	Laser Energy (kJ)	Geo. Mag.	WRF Y_{D3He} (xE8)	Aperture Diameter (μm)
36584	D2(10.5)3He(6)CH[19.4]	sg1018	22.7	12.5	9.98	1995

D^3He protons

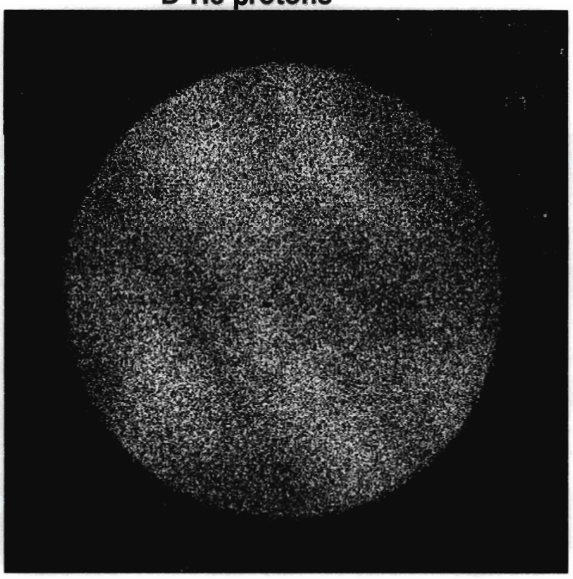

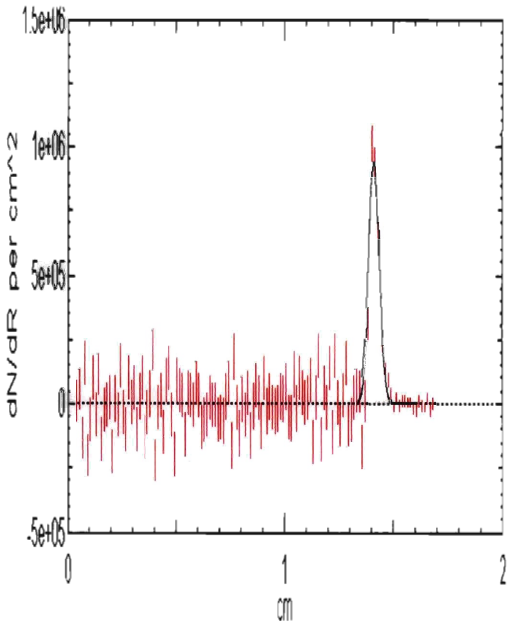

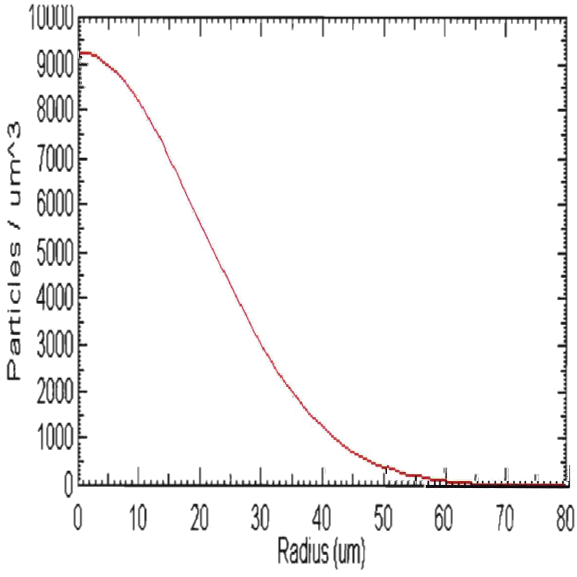

Diagnostic port:		TIM1
CR-39 ID		P19
Filtering:	first layer	200 Al
	second layer	1079 CR-39
	third layer	none
Bin size (μm)		10
Observed Magnification:		13.1
PCIS Y_{D3He} (xE8)		11.4 (12.9)
R_{burn} (μm)		27.4

Note: Some yield non-uniformities are present in this image. The uniformities are not artifacts of the scanning process.

Shot #	Capsule	Laser Pulse Shape	Beam Energy (kJ)	Geo. Mag.	WRF Y_{D3He} (xE8)	Aperture Diameter (μm)
38036	D2(6)3He(12)CH[20.4]	sg1018	23.0	12.5	8.1	2001

D^3He protons

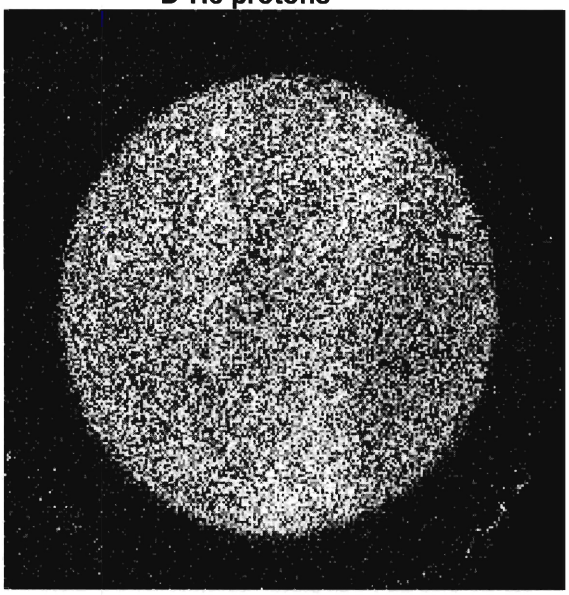

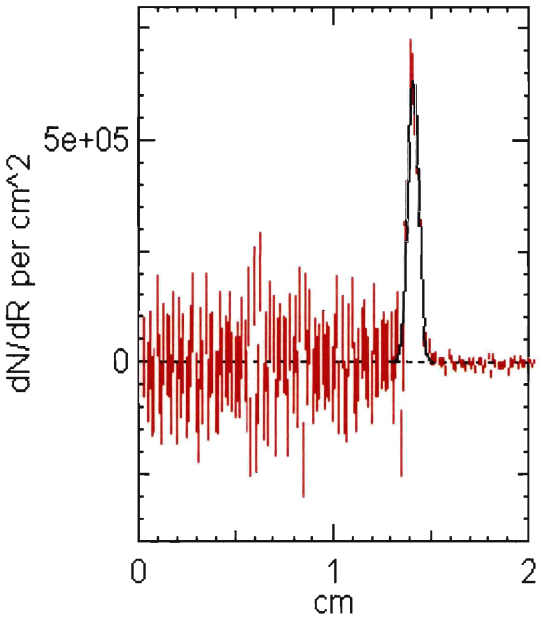

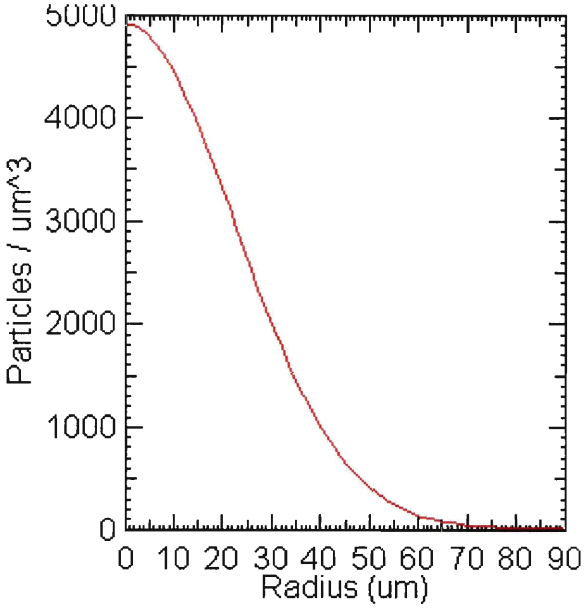

Diagnostic port:		TIM2
CR-39 ID		1P42
Filtering:	first layer	200 Al
	second layer	1081 CR-39
	third layer	10 Al
Bin size (μm)		10
Observed Magnification:		13.2 (8.3)
PCIS Y_{D3HE} (xE8)		8.0
R_{burn} (μm)		31

Shot #	Capsule	Laser Pulse Shape	Laser Energy (kJ)	Geo. Mag.	WRF Y_{D3He} (xE8)	Aperture Diameter (μm)
36876	D2(1.2)3He(2.4)CH[20]	sg1018	22.8	12.5	3.12	1998

D^3He protons

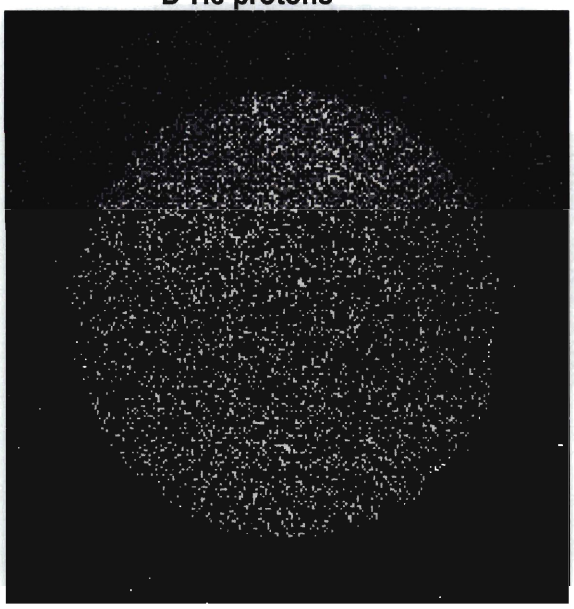

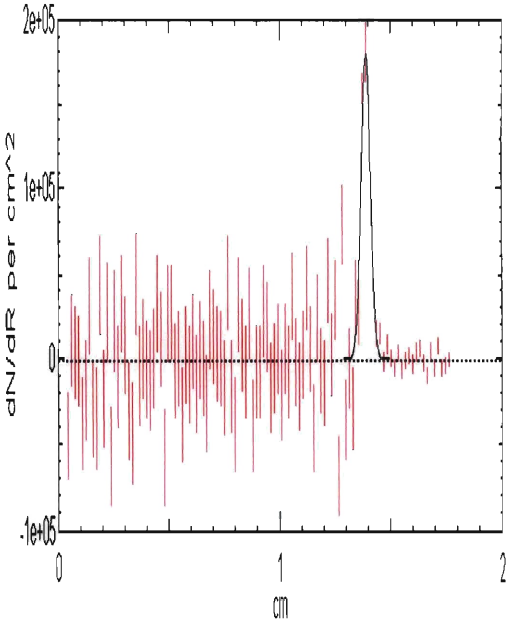

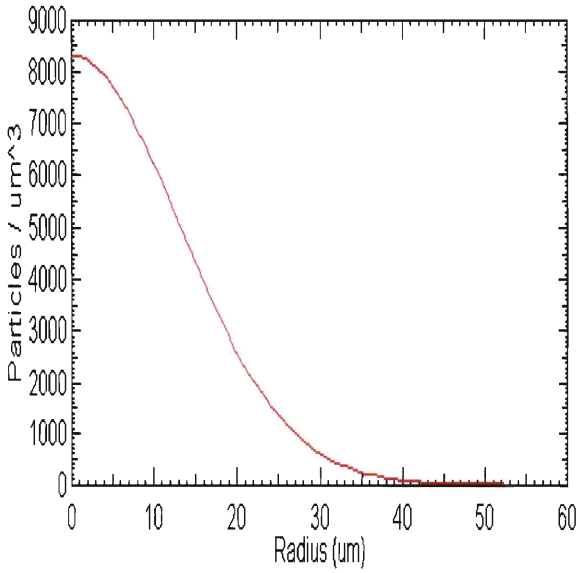

Diagnostic port:		TIM4
CR-39 ID		3P5
Filtering:	first layer	200 Al
	second layer	1016 CR-39
	third layer	none
Bin size (μm)		10
Observed Magnification:		12.9
PCIS Y_{D3He} (xE8)		2.9 (3.4)
R_{burn} (μm)		17.4

Shot #	Capsule	Laser Pulse Shape	Laser Energy (kJ)	Geo. Mag.	WRF Y_{D3He} (xE8)	Aperture Diameter (μm)
30977	D2(6)3He(12)CH[19.3]	sg1018	24.0	11	15.7	5x600

D^3He protons

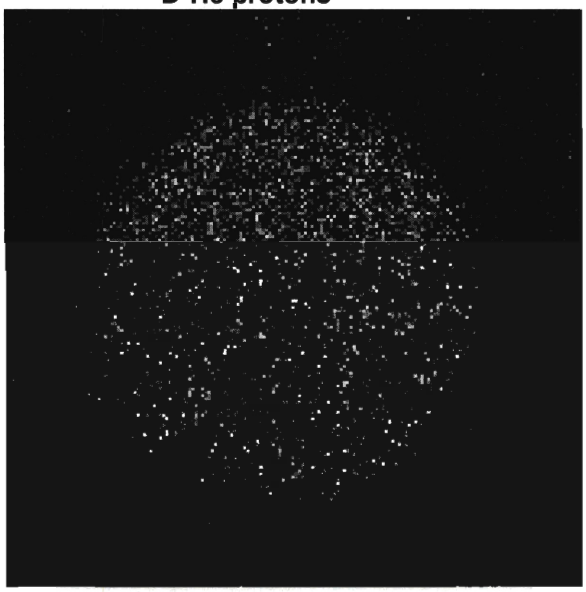

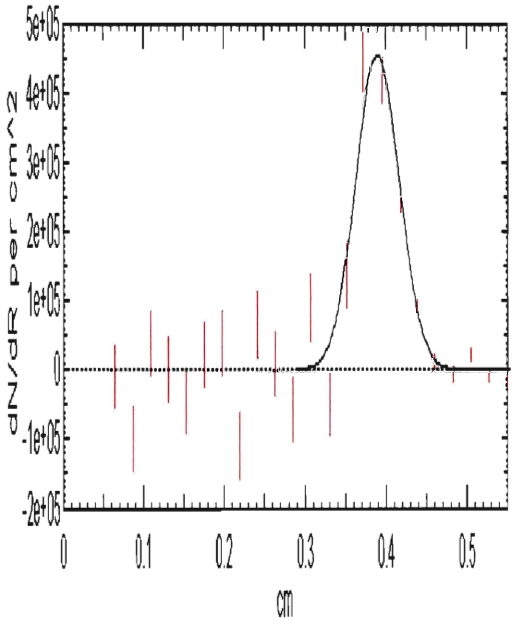

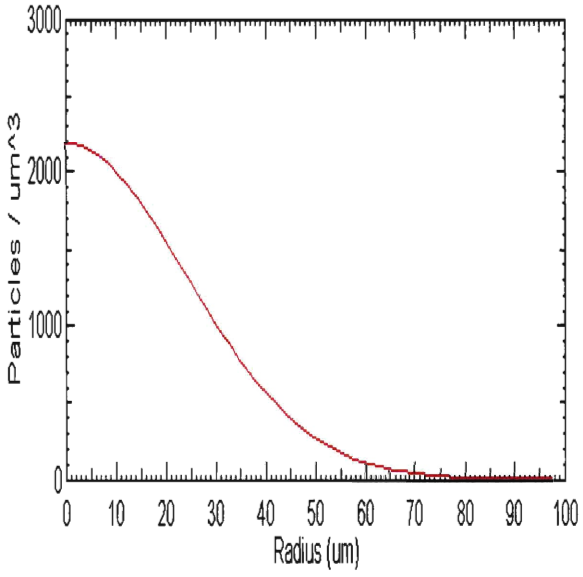

Diagnostic port:		TIM2
CR-39 ID		BB868
Filtering:	first layer	104 Al
	second layer	1165 CR-39
	third layer	25 Al
Bin size (μm)		20
Observed Magnification:		12.0
PCIS Y_{D3He} (xE8)		5 (4.8)
R_{burn} (μm)		32

NOTE: This image was taken from the top left aperture.

Shot #	Capsule	Laser Pulse Shape	Laser Energy (kJ)	Geo. Mag.	WRF Y_{D3He} (xE8)	Aperture Diameter (μm)
37643	D2(6)3He(12)CH[23.9]	sg1018	23.0	12.5	1.89	2005

D^3He protons

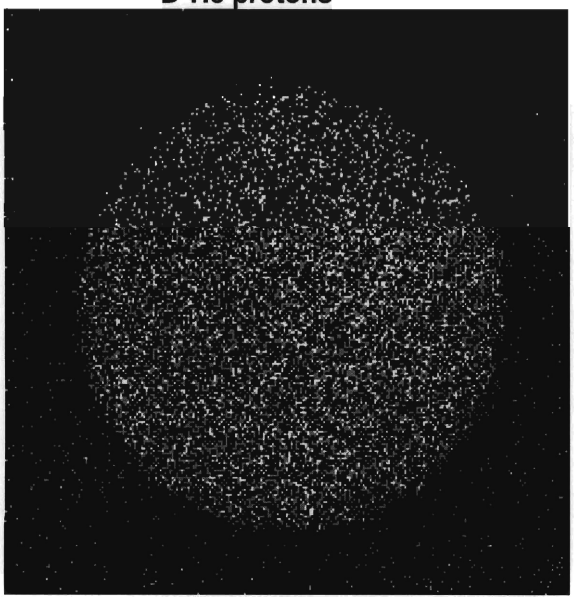

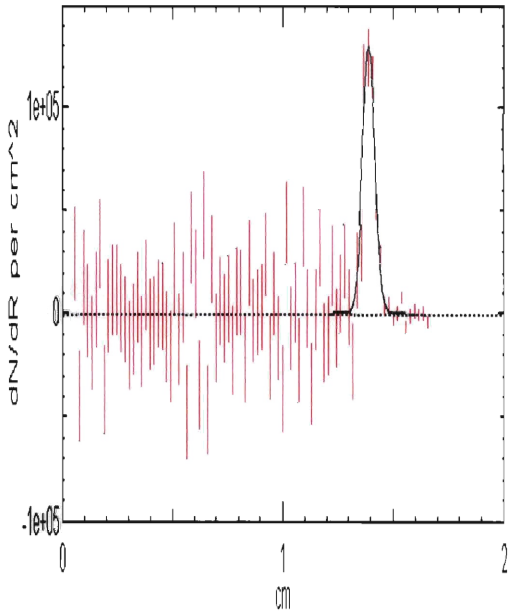

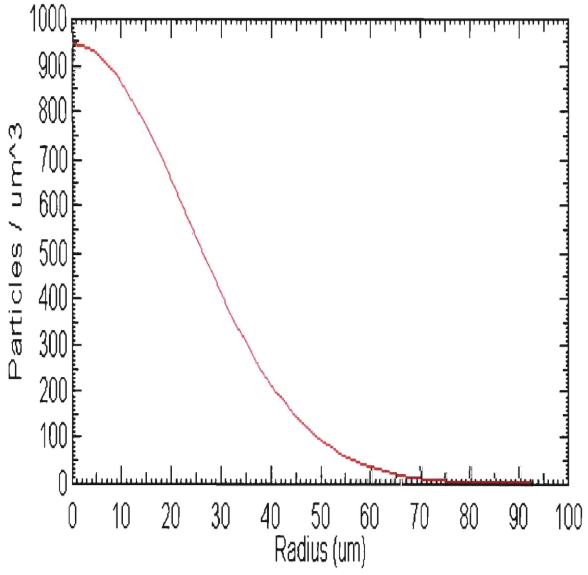

Diagnostic port:		TIM4
CR-39 ID		3P14
Filtering:	first layer	150 Al
	second layer	1084 CR-39
	third layer	25 Al
Bin size (μm)		15
Observed Magnification:		12.9
PCIS Y_{D3He} (xE8)		1.8 (2.1)
R_{burn} (μm)		31.3

Shot #	Capsule	Laser Pulse Shape	Laser Energy (kJ)	Geo. Mag.	WRF Y_{D3He} (xE8)	Aperture Diameter (μm)
36888	D2(6)3He(12)CH[27.1]	sg1018	30.2	12.5	1.3	1992
36889	D2(6)3He(12)CH[27]	sg1018	29.3		0.9	
36890	D2(6)3He(12)CH[27.1]	sg1018	30.0		1.4	

D^3He protons

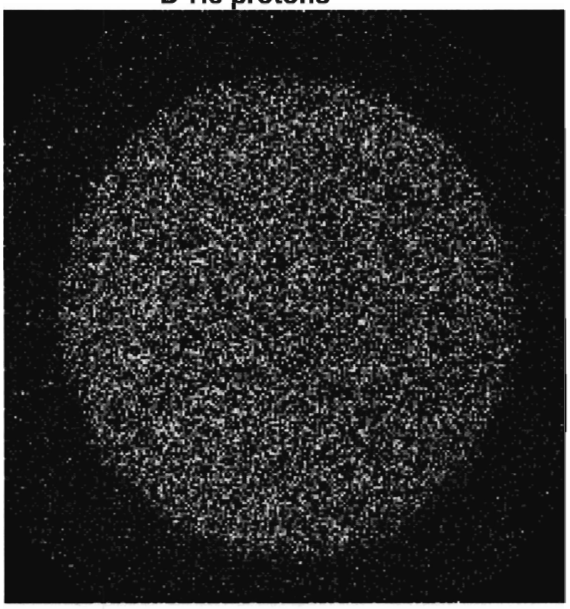

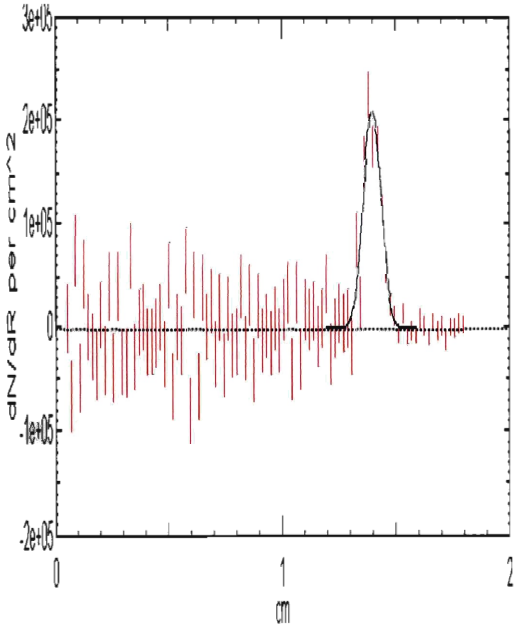

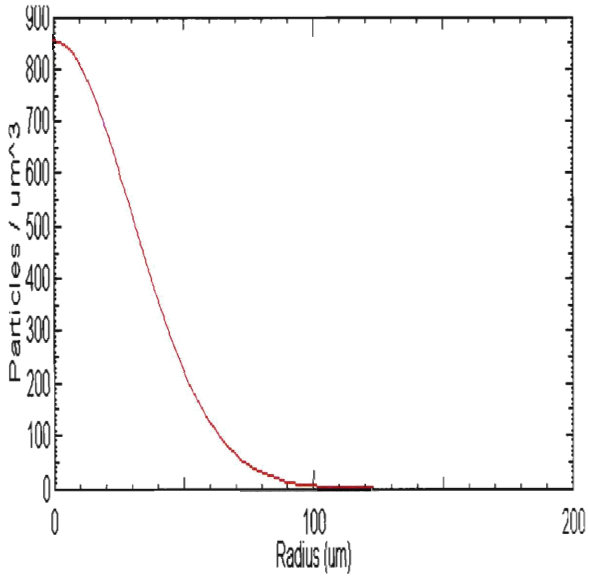

Diagnostic port:		TIM4
CR-39 ID		P94
Filtering:	first layer	150 Al
	second layer	1033 CR-39
	third layer	none
Bin size (μm)		15
Observed Magnification:		13.0
PCIS Y_{D3He} (xE8)		4.0 (4.3)
R_{burn} (μm)		42.5

NOTE: The penumbral image was obtained by summing 3 consecutive implosions

Shot #	Capsule	Laser Pulse Shape	Laser Energy (kJ)	Geo. Mag.	nTOF Y_{DD} (xe10)	Aperture Diameter (μm)
37839	D2(6.3)3He(13.7)CH[18.4]	sg1018	20.8	16	1.3	2007

DD shock protons

Diagnostic port:		TIM3
CR-39 ID		3P18
Filtering:	first layer	7.5 Ta
	second layer	--
	third layer	--
Bin size (μm)		NA
Observed Magnification:		NA
PCIS Y_{DD} (xE8)		NA (0.9)
R_{burn} (μm)		NA

Shot #	Capsule	Laser Pulse Shape	Laser Energy (kJ)	Geo. Mag.	WRF Y_{D3He} (xE8)	Aperture Diameter (μm)
37845	D2(6.3)3He(13.7)SiO2[9]	sg1018	23.2	12.5	0.7	2000

D^3He protons

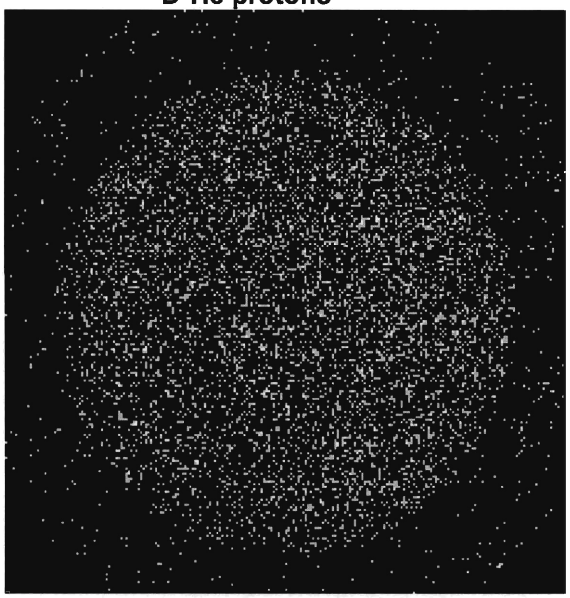

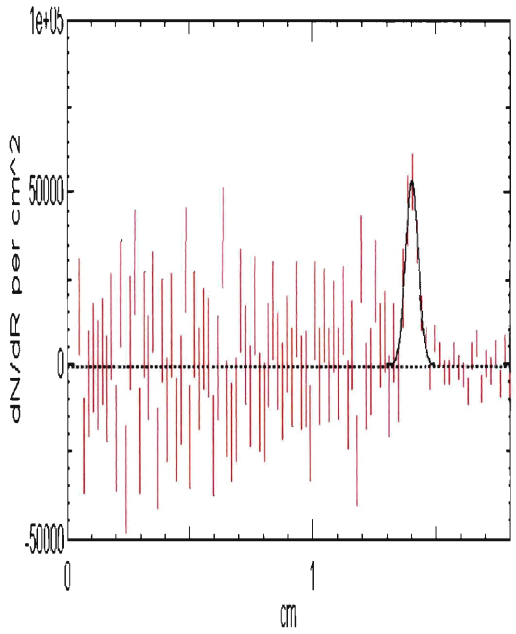

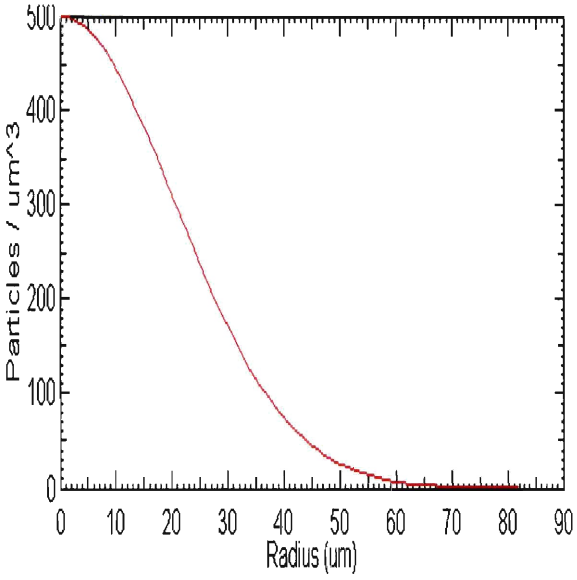

Diagnostic port:		TIM6
CR-39 ID		1P35
Filtering:	first layer	200 Al
	second layer	1025 CR-39
	third layer	25 Al
Bin size (μm)		10
Observed Magnification:		13.0
PCIS Y_{D3He} (xE8)		0.7 (1.0)
R_{burn} (μm)		27.3

Shot #	Capsule	Laser Pulse Shape	Laser Energy (kJ)	Geo. Mag.	WRF Y_{D3He} (xE8)	Aperture Diameter (μm)
38539	D2(6)3He(12)SiO2[2]	sg1018 20 beams	8.9	16		2008

D^3He alphas

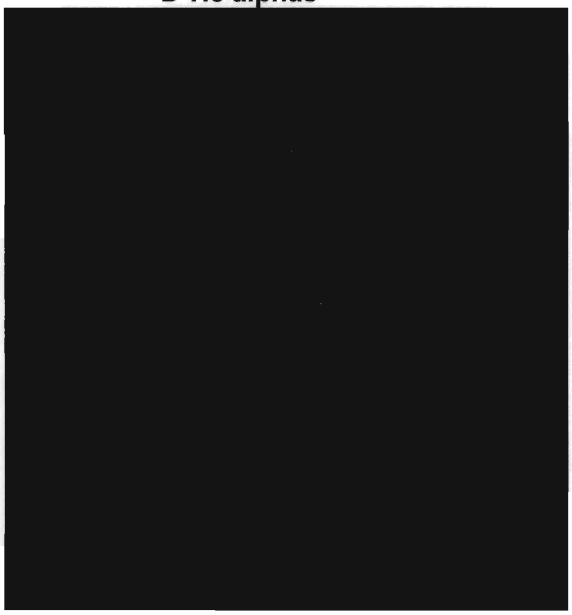

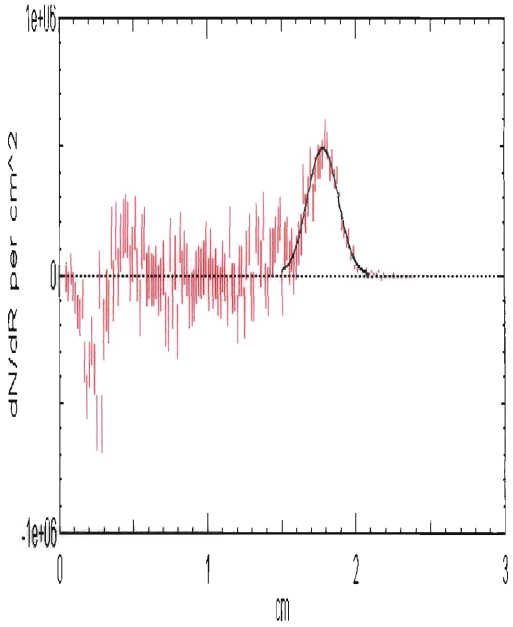

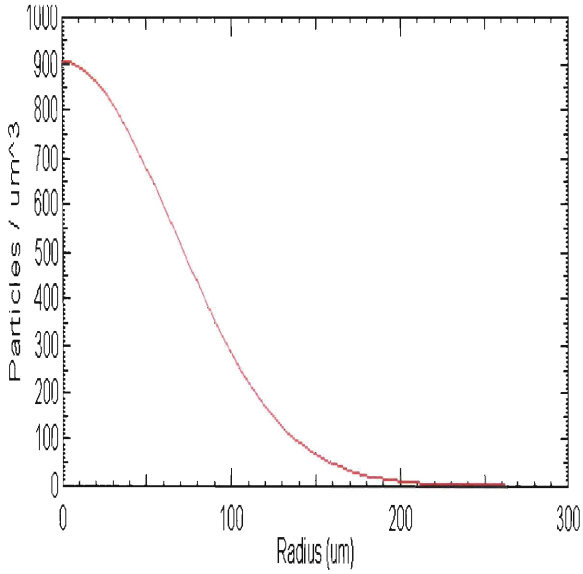

Diagnostic port:		TIM4
CR-39 ID		3P77
Filtering:	first layer	5 Ta
	second layer	--
	third layer	--
Bin size (μm)		10
Observed Magnification:		16.7
PCIS Y_{D3He} (xE8)		40.2 (58.3)
R_{burn} (μm)		92.6

Shot #	Capsule	Laser Pulse Shape	Laser Energy (kJ)	Geo. Mag.	nTOF Y_{DD} (xe10)	Aperture Diameter (μm)
38539	D2(6)3He(12)SiO2[2]	sg1018 20 beams	8.9	16	0.5	2008

DD protons

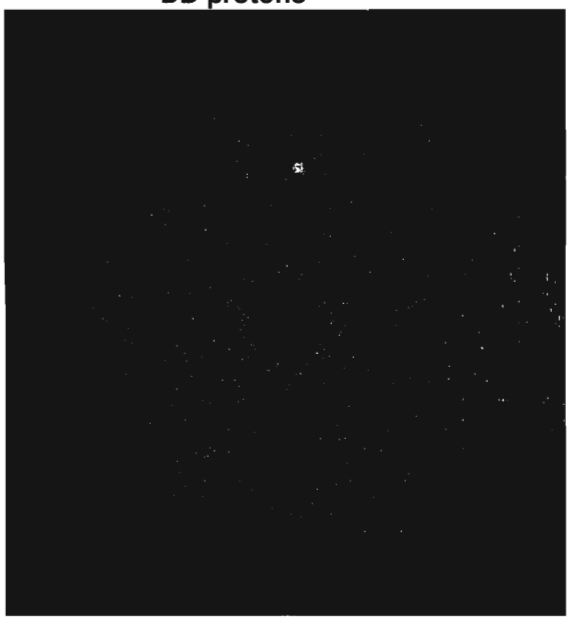

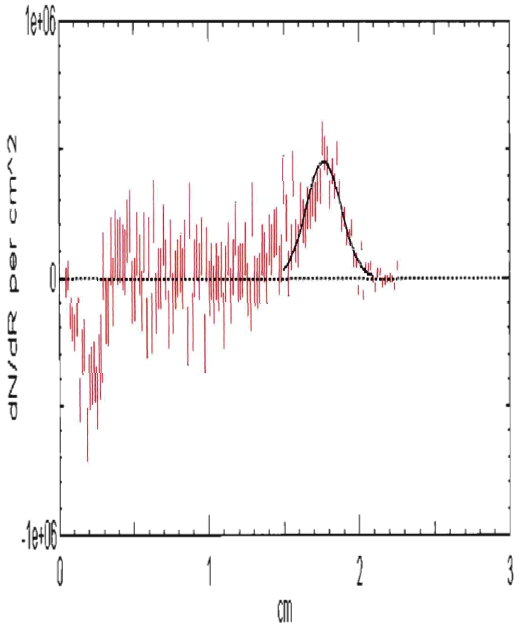

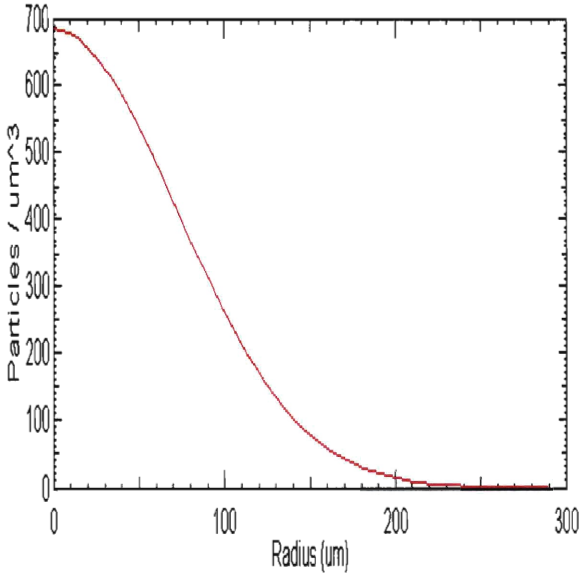

Diagnostic port:		TIM4
CR-39 ID		3P77
Filtering:	first layer	5 Ta
	second layer	--
	third layer	--
Bin size (μm)		10
Observed Magnification:		16.6
PCIS Y_{DD} (xE8)		34 (48.5)
R_{burn} (μm)		99.0

Shot #	Capsule	Laser Pulse Shape	Laser Energy (kJ)	Geo. Mag.	WRF Y_{D3He} (xE8)	Aperture Diameter (μm)
38539	D2(6)3He(12)SiO2[2]	sg1018 20 beams	8.9	16		2008

D^3He protons

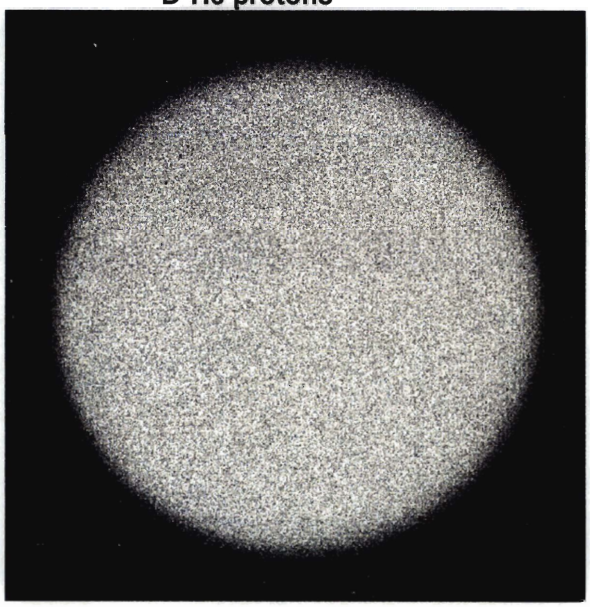

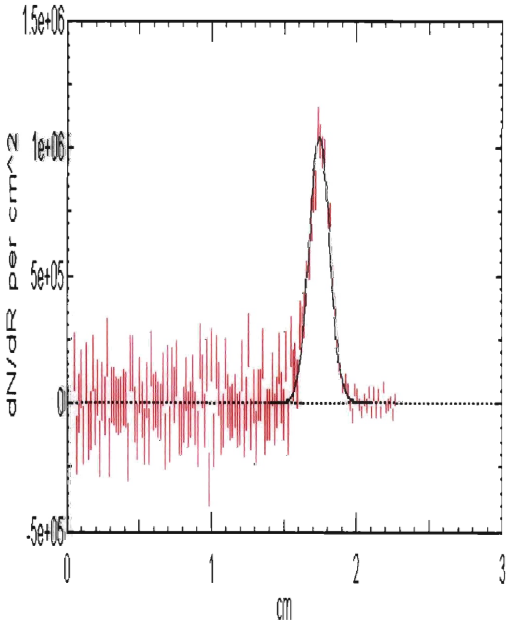

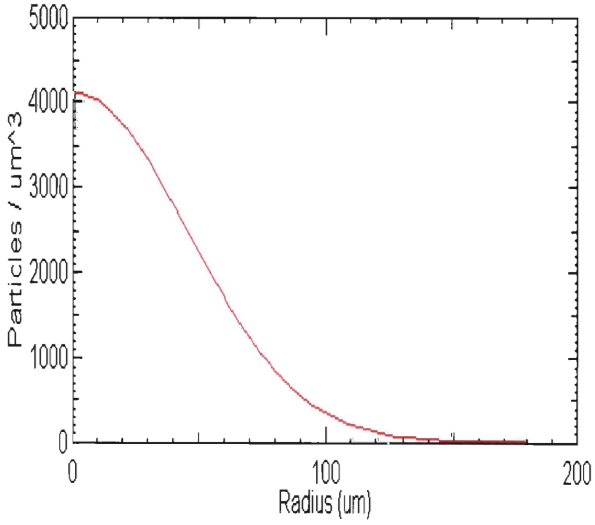

Diagnostic port:		TIM4
CR-39 ID		3P19
Filtering:	first layer	5 Ta
	second layer	1018 CR-39
	third layer	350 Al
Bin size (μm)		10
Observed Magnification:		16.3
PCIS Y_{D3He} (xE8)		58.0 (63.5)
R_{burn} (μm)		62.3

Shot #	Capsule	Laser Pulse Shape	Laser Energy (kJ)	Geo. Mag.	WRF Y_{D3He} (xE8)	Aperture Diameter (μm)
27456	D2(6)3He(12)SiO2[1.8]	sg1018	12.0	8	162	4x600

D^3He protons

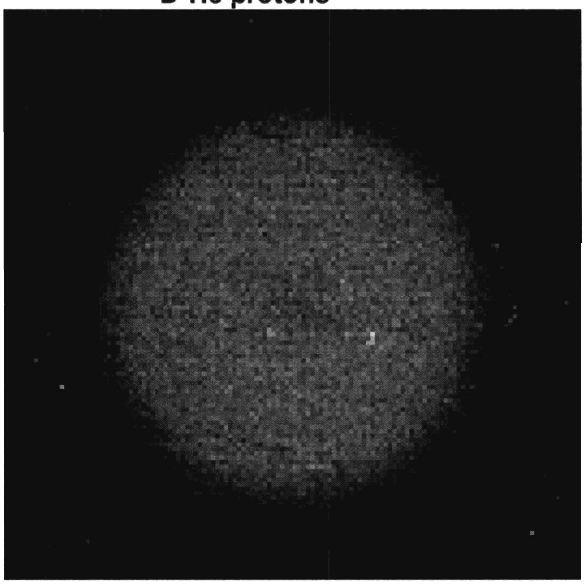

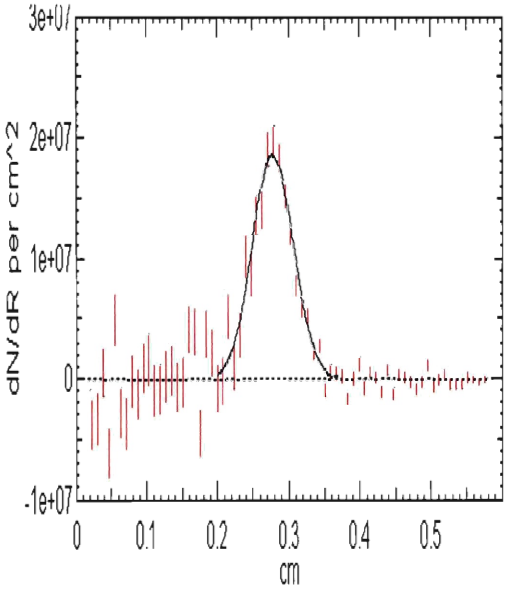

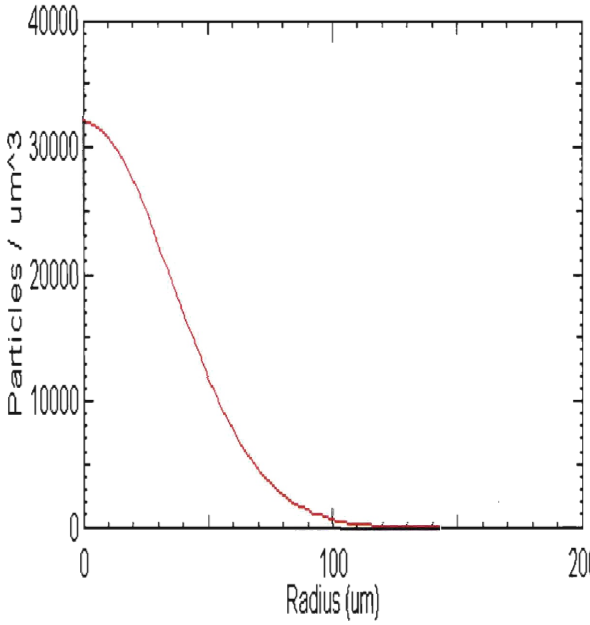

Diagnostic port:		TIM1
CR-39 ID		BB484
Filtering:	first layer	10 Al
	second layer	1135 CR-39
	third layer	300 Al
Bin size (μm)		25
Observed Magnification:		8.3
PCIS Y_{D3He} (xE8)		233 (244)
R_{burn} (μm)		48.1

NOTE: This image was taken from the center aperture.

Shot #	Capsule	Laser Pulse Shape	Laser Energy (kJ)	Geo. Mag.	nTOF Y_{DD} (xe10)	Aperture Diameter (μm)
37134	DD(15)CH[19.6]	sg1018	23.4	12.5	16.2	2004

DD shock protons

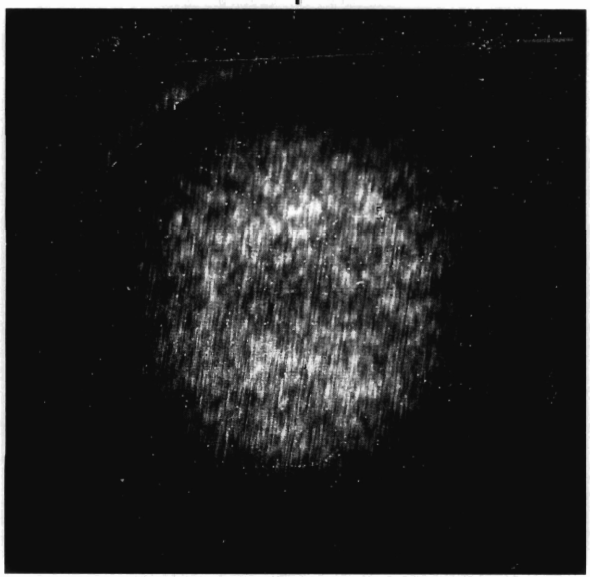

Diagnostic port:		TIM6
CR-39 ID		3P37
Filtering:	first layer	12.5 Al
	second layer	--
	third layer	--
Bin size (μm)		
Observed Magnification:		
PCIS Y_{DD}		NA (750)
R_{burn} (μm)		

Shot #	Capsule	Laser Pulse Shape	Laser Energy (kJ)	Geo. Mag.	WRF Y_{D3He} (xE8)	Aperture Diameter (μm)
37134	DD(15)CH[19.6]	sg1018	23.4	12.5	3.3	2004

Secondary D^3He protons

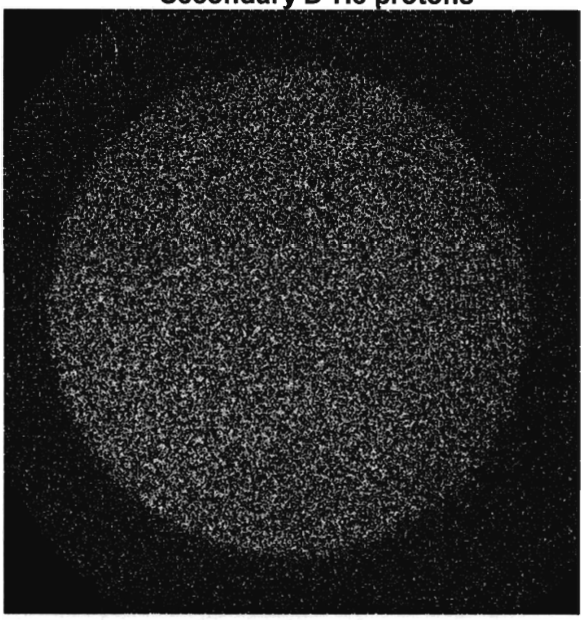

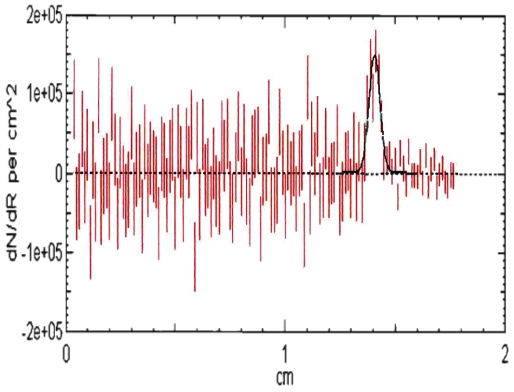

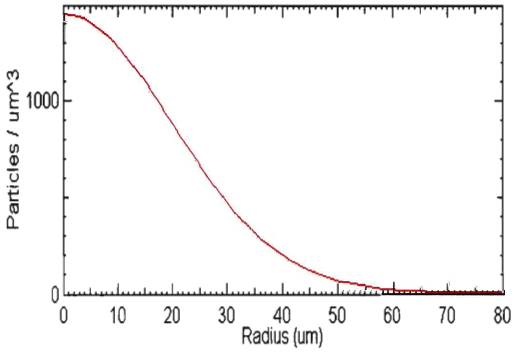

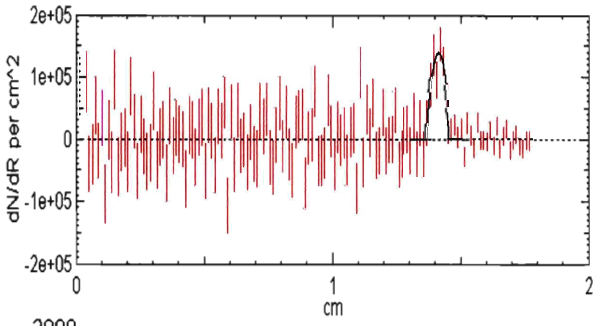

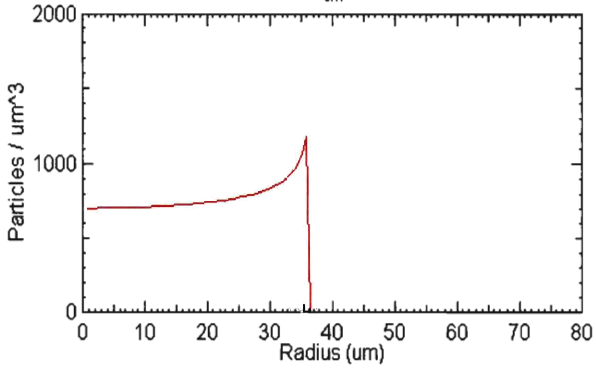

Diagnostic port:		TIM6
CR-39 ID		3P80
Filtering:	first layer	12.5 Al
	second layer	1008 CR-39
	third layer	50 Al
Bin size (μm)		10.0
Observed Magnification:		13.1
PCIS Y_{D3He} (xE8)		1.8 (2.3)
R_{burn} (μm) (Gaussian)		27.5*

*NOTE: For these secondary D^3He protons, the shape of the profile is not well determined. A Gaussian profile and a hollow profile are shown. The Gaussian profile corresponds to a reduced chi squared of 0.78, and the hollow profile corresponds to 0.77.

Shot #	Capsule	Laser Pulse Shape	Laser Energy (kJ)	Geo. Mag.	WRF Y_{D3He} (xE8)	Aperture Diameter (μm)
37232	DT(15)CH[19]	sg1018	23.3	19	21	2000

DT knock-on protons

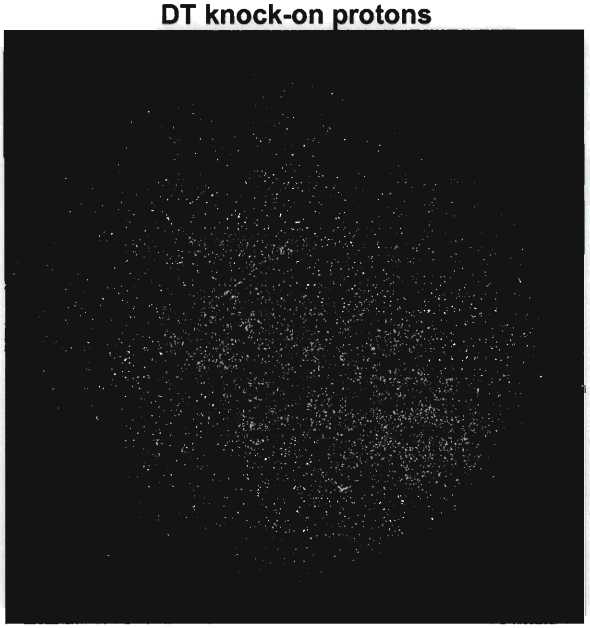

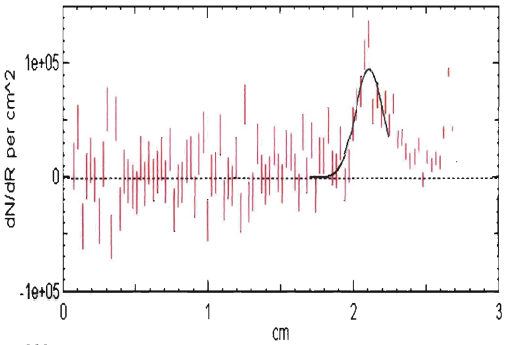

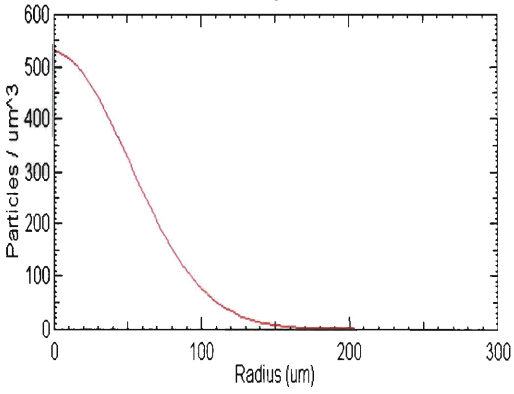

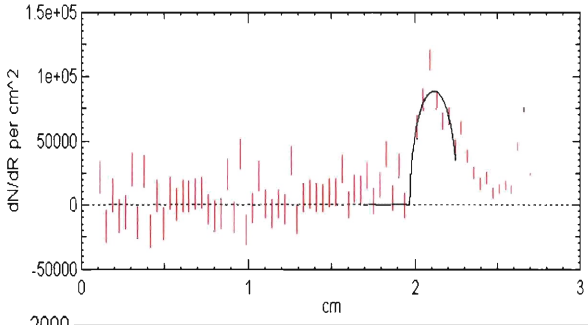

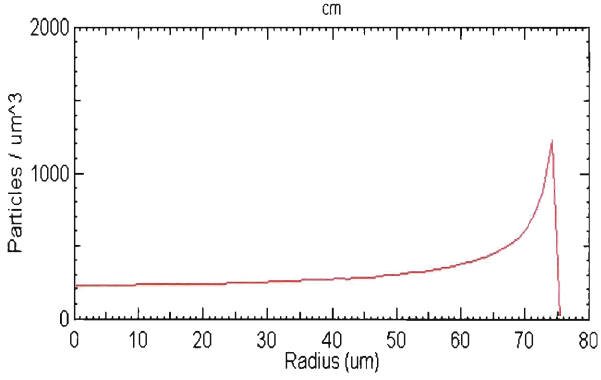

Diagnostic port:		TIM6
CR-39 ID		3P22
Filtering:	first layer	100 Al
	second layer	--
	third layer	--
Bin size (μm)		15 & 20
Observed Magnification:		20.1
PCIS $Y_{knock-on}$ (xE8)		10 (20)
$R_{burn,\ knock-on}$ (μm)		~70

NOTE: The data indicates the possibility of a hollow shaped source. Unfortunately, the far left edge of the image was not captured on the CR-39 and only the data with radii less than 2.25 cm was included in the fits. In the future, a more thorough treatment of the data may reduce the uncertainty in the shape of the source.

Appendix G. Filter assignments for standard implosions

Standard filtering for burn imaging of various types of implosions are summarized in this section. These figures are meant to serve as a guide to select proper filtering for future experiments.

For each type of implosion, results from a standard implosion are presented. Included are:

The type of implosion (in bold)
Shot number

Capsule specifics:
- The type and amount of gas fill (atm),
  - D - deuterium
  - 3He - 3-helium
  - T – tritium
- The shell type and thickness (μm)
  - CH – plastic shell
  - SiO2 - glass shell

PCIS setup specifics:
Diagnostic port on which the imaging camera was mounted
CR-39 identification that corresponds to the contour plot
Filtering (in μm) placed in front of the CR-39 (up to three layers)
- Al – Aluminum
- Ta – Tantalum
- CR-39 – thickness of a preceding sheet of CR-39

Also included for each implosion type are two figures:

The first figure is a representative spectrum taken from the implosion, presented as particle yield as a function of energy. The filtering was selected for efficient detection of the entire spectrum.

The second figure is a contour plot of the number of tracks vs. optical contrast and track diameter for the PCIS data. The low diameter tracks with high optical contrast typically correspond to the intrinsic CR-39 background.

The first example is included to illustrate the result of insufficient filtering; the majority of the signal tracks are < 4 μm in diameter with high optical contrast. There is not a clear separation between the signal tracks and the intrinsic CR-39 background. In contrast, proper filtering of the remaining examples resulted in a more clear separation of signal tracks from the CR-39 intrinsic background. (Representative penumbral images were presented in Appendix F.)

Improper filtering

Shot 35004

Capsule:

	Gas fill	D2(6)3He(12)
	shell	CH[19.6]

PCIS setup

Diagnostic port:	TIM3
CR-39 ID	PD52

Filtering:

first layer	104 Al
second layer	1056 CR-39
third layer	20 Ta

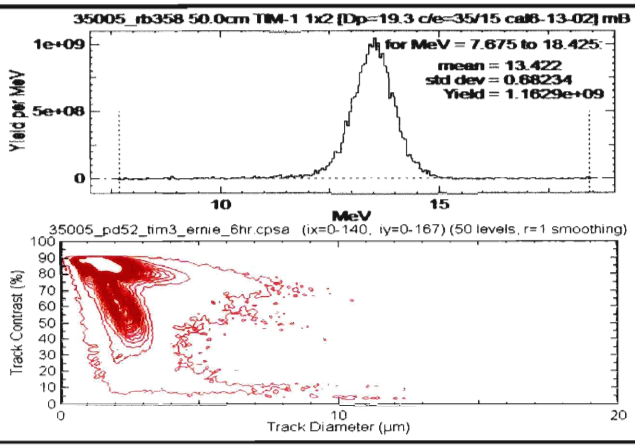

17 µm thick CH shell

Shot 36020

Capsule:

	Gas fill	D3He(20)
	shell	CH[17.1]

PCIS setup

Diagnostic port:	TIM3
CR-39 ID	P11

Filtering:

first layer	200 Al
second layer	1062 CR-39
third layer	50 Al

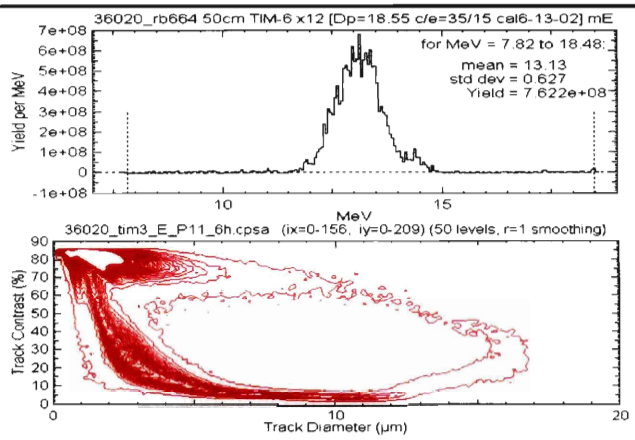

18 µm thick CH shell

Shot 37840

Capsule:

	Gas fill	D3He(20)
	shell	CH[18]

PCIS setup

Diagnostic port:	TIM3
CR-39 ID	3P84

Filtering:

first layer	200 Al
second layer	1092 CR-39
third layer	12.5 Al

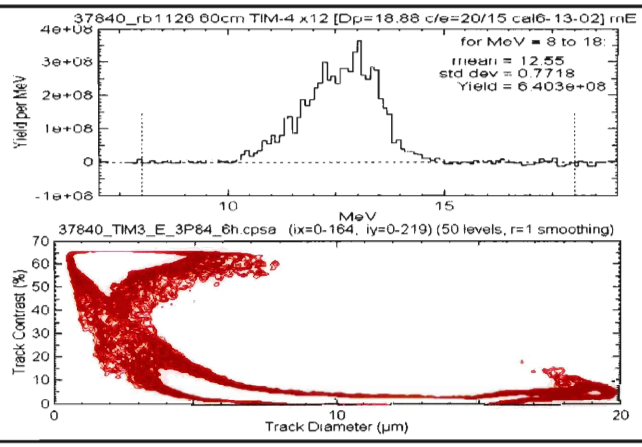

19 μm thick CH shell

Shot	36586	
Capsule:		
	Gas fill	D2(11)3He(6)
	shell	CH[19.2]
PCIS setup		
Diagnostic port:		TIM1
CR-39 ID		P75
Filtering:		
	first layer	200 Al
	second layer	1090 CR-39
	third layer	none

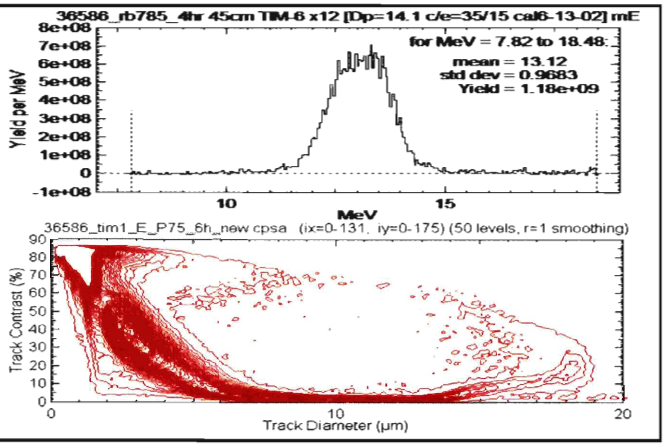

20 μm thick CH shell

Shot	38036	
Capsule:		
	Gas fill	D2(6)3He(12)
	shell	CH[20.4]
PCIS setup		
Diagnostic port:		TIM2
CR-39 ID		1P42
Filtering:		
	first layer	200 Al
	second layer	1081 CR-39
	third layer	10 Al

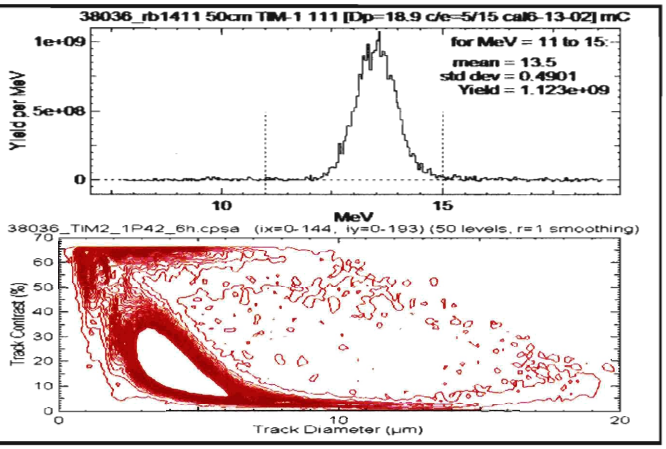

20 μm thick CH shell, low fill

Shot	38030	
Capsule:		
	Gas fill	D3He(3.6)
	shell	CH[20.1]
PCIS setup		
Diagnostic port:		TIM2
CR-39 ID		1P160
Filtering:		
	first layer	200 Al
	second layer	1077 CR-39
	third layer	10 Al

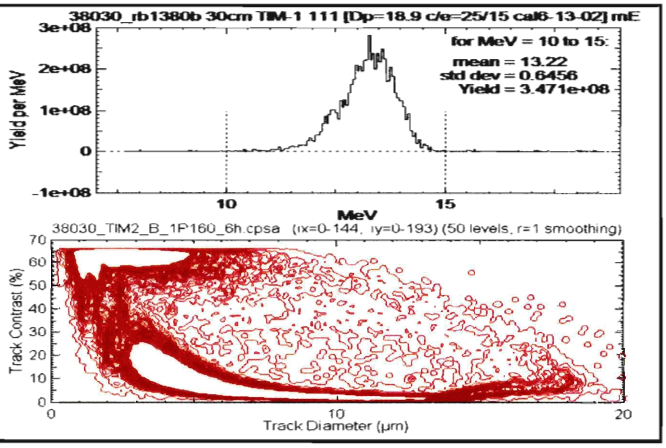

24 μm thick CH shell

Shot 38033

Capsule:

Gas fill	D2(6)3He(12)
shell	CH[23.7]

PCIS setup

Diagnostic port:	TIM2
CR-39 ID	1P51
Filtering:	
first layer	150 Al
second layer	1066 CR-39
third layer	10 Al

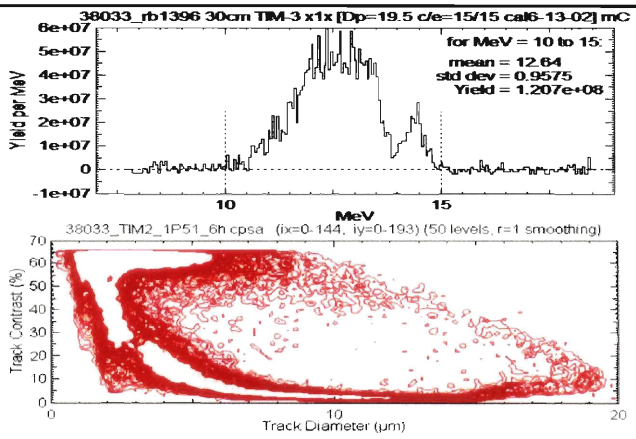

24 μm thick CH shell

Shot 37645

Capsule:

Gas fill	D2(6)3He(12)
shell	CH[23.8]

PCIS setup

Diagnostic port:	TIM2
CR-39 ID	3P9
Filtering:	
first layer	150 Al
second layer	1079 CR-39
third layer	10 Al

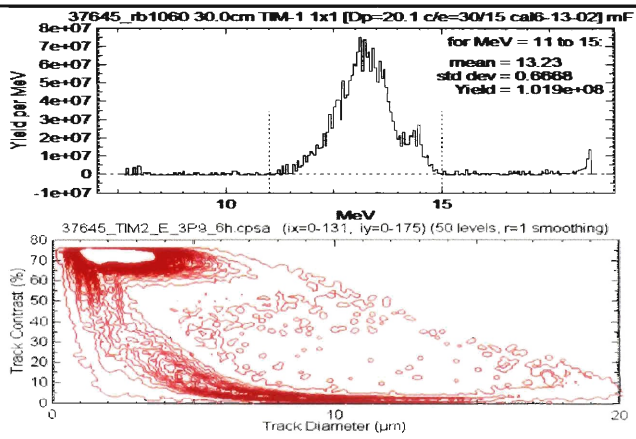

27 μm thick CH shell

Shot 37646

Capsule:

Gas fill	D2(6)3He(12)
shell	CH[26.6]

PCIS setup

Diagnostic port:	TIM4
CR-39 ID	3P52
Filtering:	
first layer	150 Al
second layer	1027 CR-39
third layer	25 Al

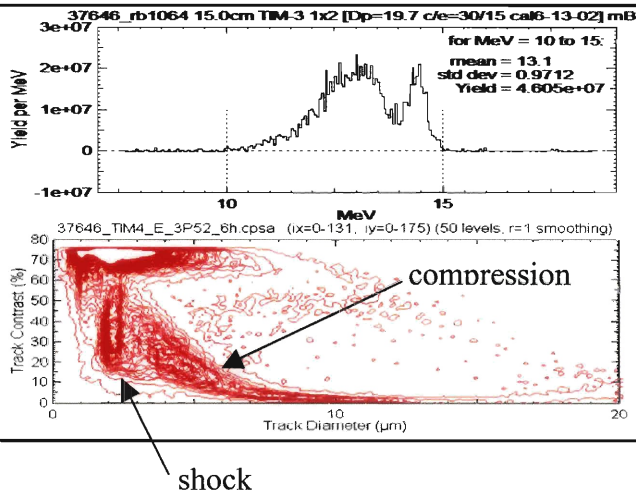

Secondary D^3He protons, 20 μm shell

Shot	37134	
Capsule:		
	Gas fill	DD(15)
	shell	CH[19.6]
PCIS setup		
Diagnostic port:		TIM6
CR-39 ID		3P80
Filtering:		
	first layer	12.5 Al
	second layer	1008 CR-39
	third layer	50 Al

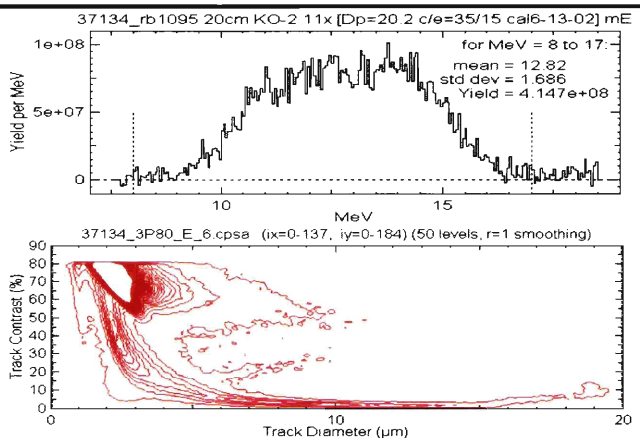

Thin glass (DD protons and D^3He alphas)

Shot	38539	
Capsule:		
	Gas fill	D2(6)3He(12)
	shell	SiO2[2]
PCIS setup		
Diagnostic port:		TIM4
CR-39 ID		3P77
Filtering:		
	first layer	5 Ta
	second layer	--
	third layer	--

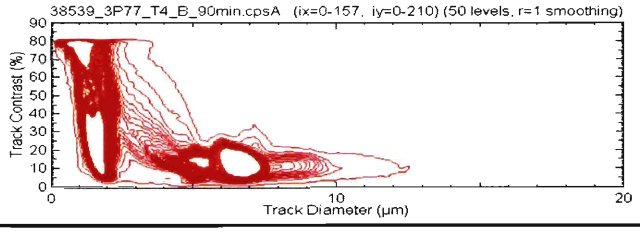

Thin glass, D^3He protons

Shot	38539	
Capsule:		
	Gas fill	D2(6)3He(12)
	shell	SiO2[2]
PCIS setup		
Diagnostic port:		TIM4
CR-39 ID		3P19
Filtering:		
	first layer	5 Ta
	second layer	1018 CR-39
	third layer	350 Al

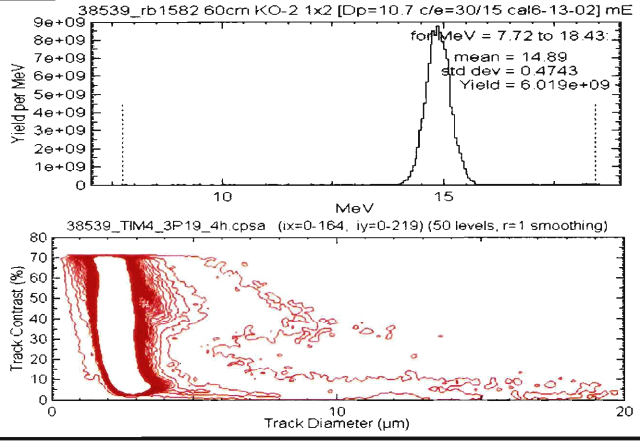

Appendix H. Hardware

Technical drawings are included here for future reference. A schematic of an assembled camera is shown in Fig. H1; each part has been identified and called out by its drawing number. (The drawing number is included in the lower right corner of each page.) Each filter pack includes a series of three separate drawings (a, b, and c), corresponding to the three separate magnification slots (20x, 16x, and 12.5x).

The camera front-end, or nosecone, has not been redesigned. We typically use the standard 12x framing camera nosecone assembly, supplied by the Laboratory for Laser Energetics.

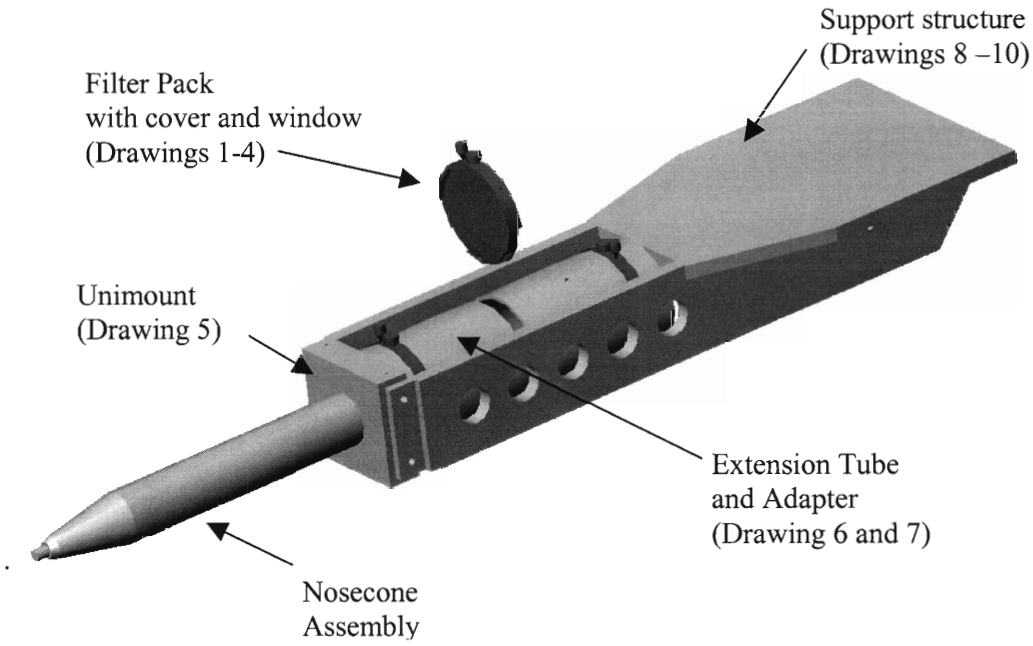

Figure H1 Schematic of camera hardware

FIG. H1. The proton-emission imaging cameras consist of five main parts: the filter pack, unimount, extension tube (and adapter), support structure, and the nosecone assembly.

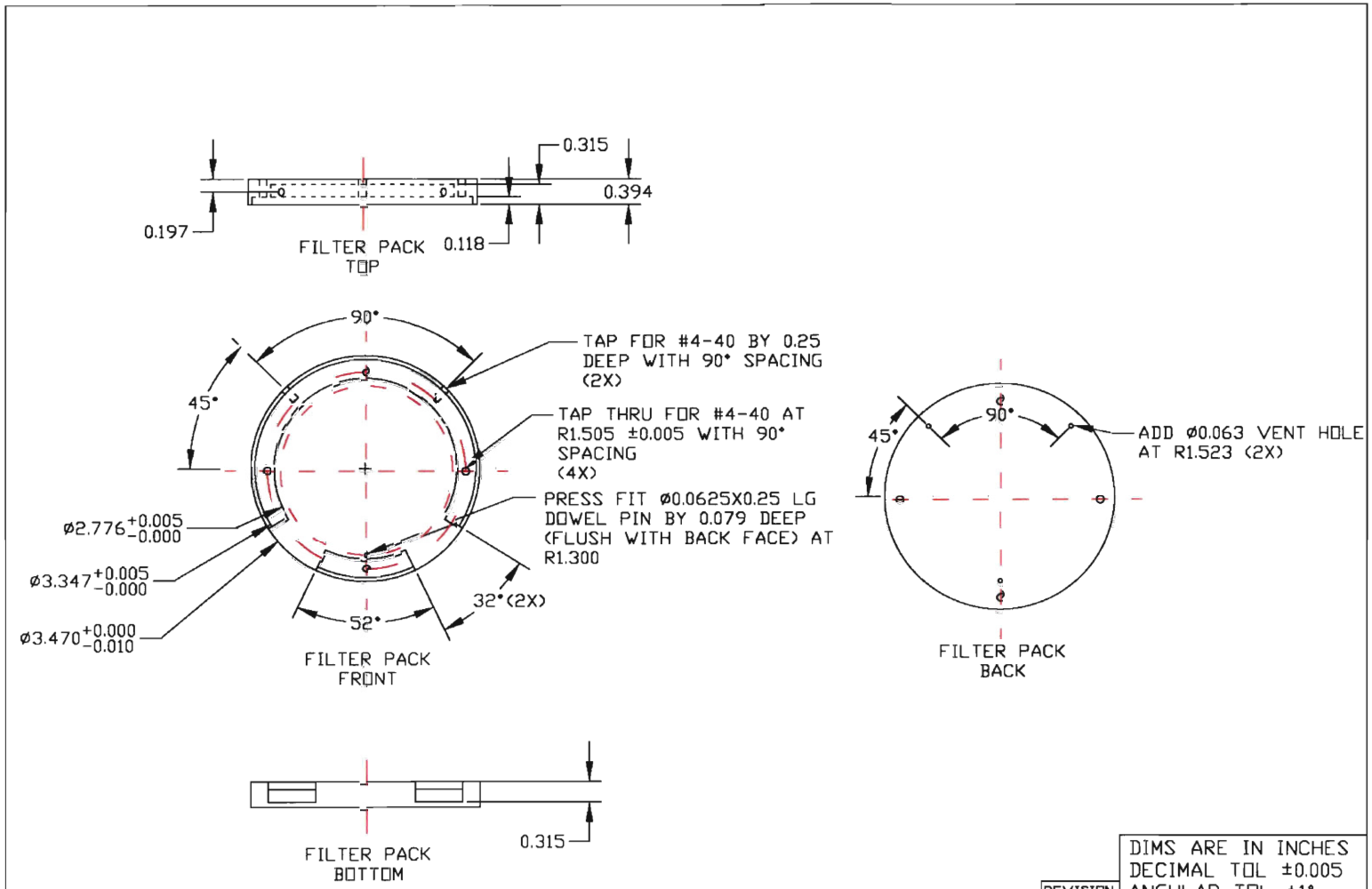

ITEM	QTY	PART NO.	DESCRIPTION	NOTES
1	1	98381A415	DOWEL PIN Ø.063X.25 LG	McMASTER

DEVIATIONS FROM INTENDED SHAPE (FLATNESS, ROUNDNESS, ECT.) MUST BE WITHIN STATED DIMENSIONAL TOLERANCES PER ANSI Y14.5M-1982

REVISION	4
DATE	03/23/04
DWG No	1

DIMS ARE IN INCHES
DECIMAL TOL ±0.005
ANGULAR TOL ±1°
BREAK ALL EDGES
MATERIAL: Al 6061-T6
SCALE 2.00
DETAIL
FILTER PACK

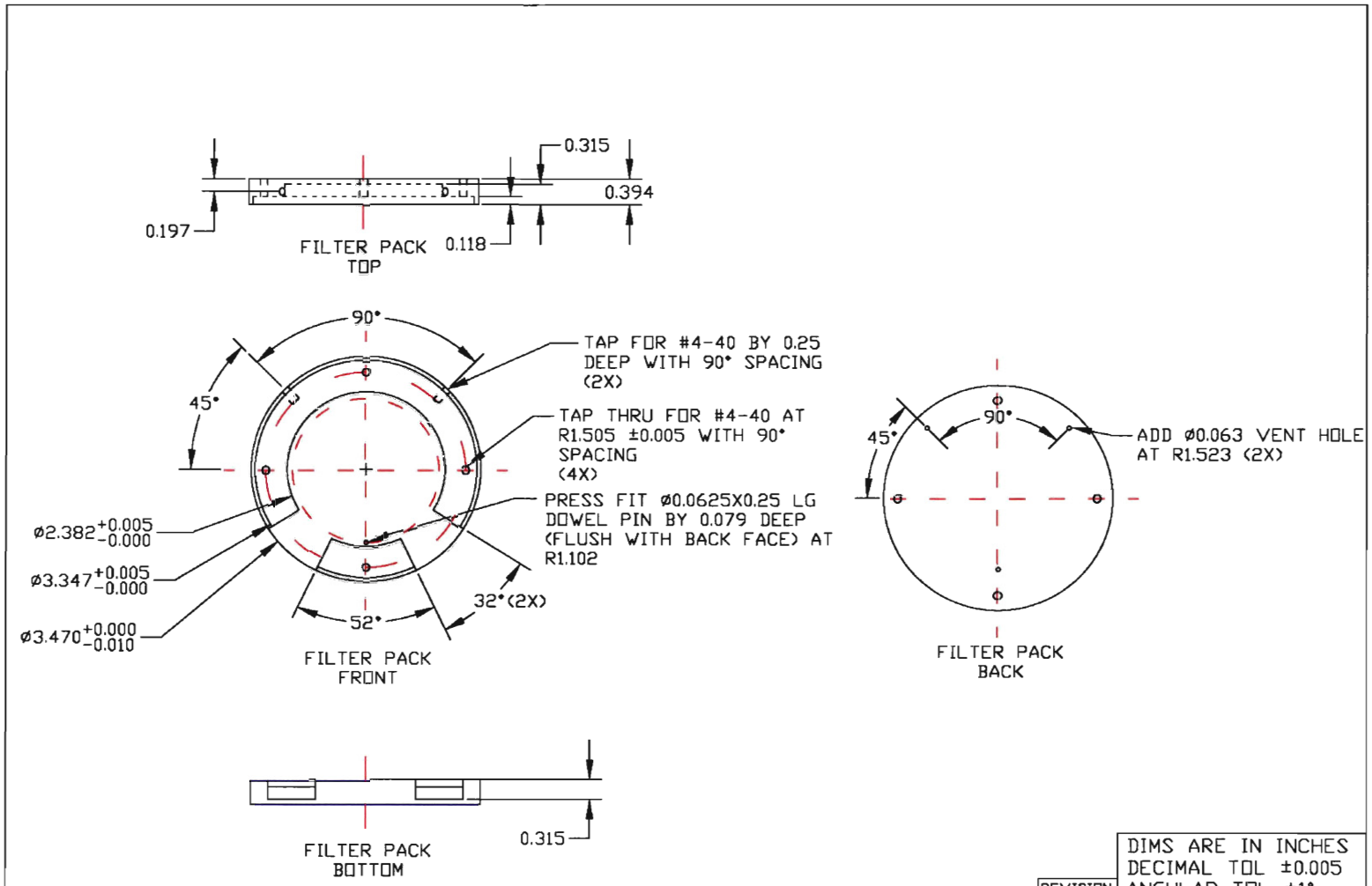

ITEM	QTY	PART NO.	DESCRIPTION	NOTES
1	1	98381A415	DOWEL PIN Ø.063X.25 LG	McMASTER

DEVIATIONS FROM INTENDED SHAPE (FLATNESS, ROUNDNESS, ECT.) MUST BE WITHIN STATED DIMENSIONAL TOLERANCES PER ANSI Y14.5M-1982

REVISION	1
DATE	03/23/04
DWG No	1b

DIMS ARE IN INCHES
DECIMAL TOL ±0.005
ANGULAR TOL ±1°
BREAK ALL EDGES
MATERIAL: Al 6061-T6
SCALE 2.00
DETAIL
FILTER PACK 60 mm

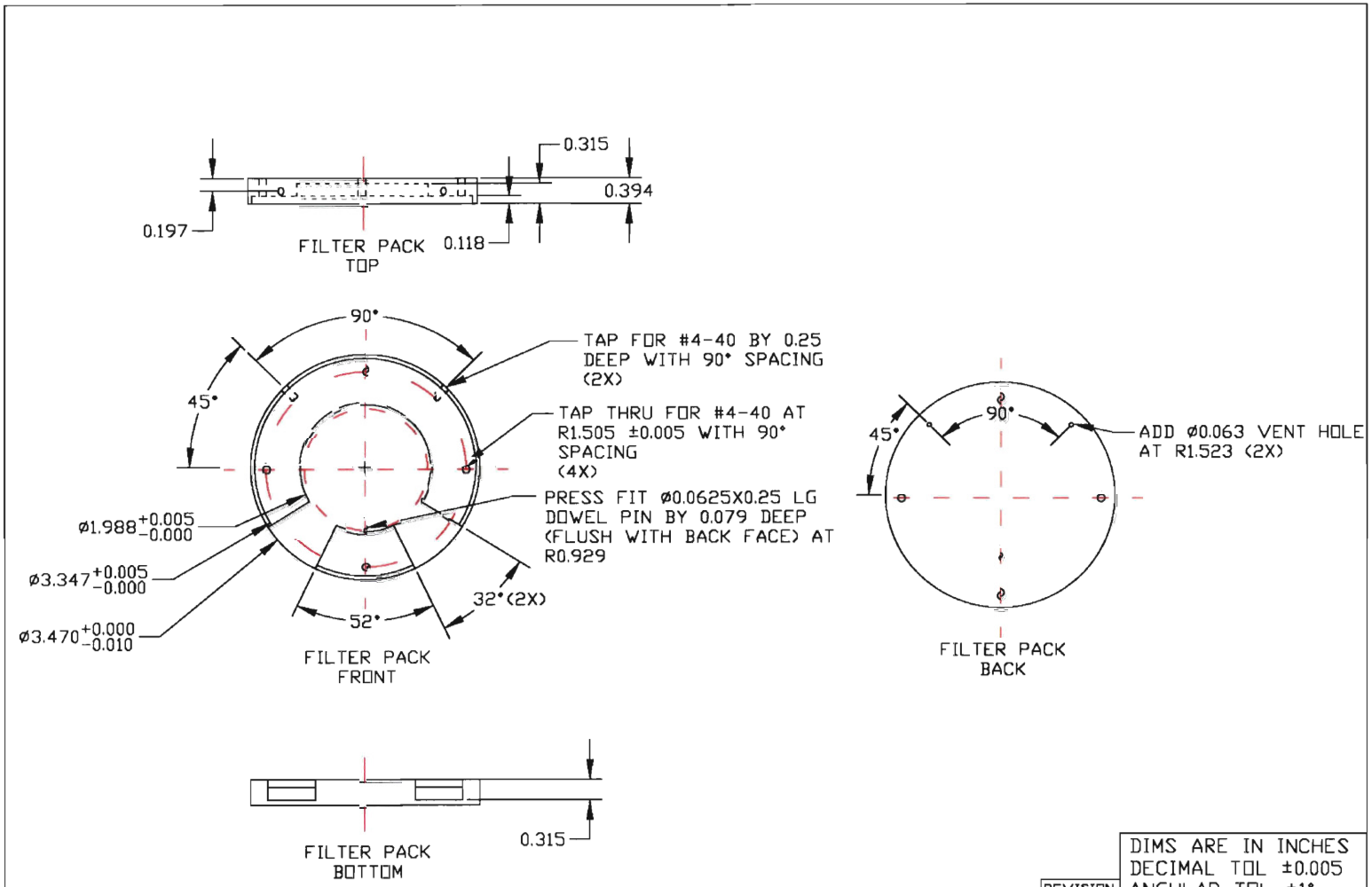

ITEM	QTY	PART NO.	DESCRIPTION	NOTES
1	1	98381A415	DOWEL PIN Ø.063X.25 LG	McMASTER

DEVIATIONS FROM INTENDED SHAPE (FLATNESS, ROUNDNESS, ECT.) MUST BE WITHIN STATED DIMENSIONAL TOLERANCES PER ANSI Y14.5M-1982

REVISION	1
DATE	03/23/04
DWG No	1c

DIMS ARE IN INCHES
DECIMAL TOL ±0.005
ANGULAR TOL ±1°
BREAK ALL EDGES
MATERIAL: Al 6061-T6
SCALE 2.00
DETAIL
FILTER PACK 50 mm

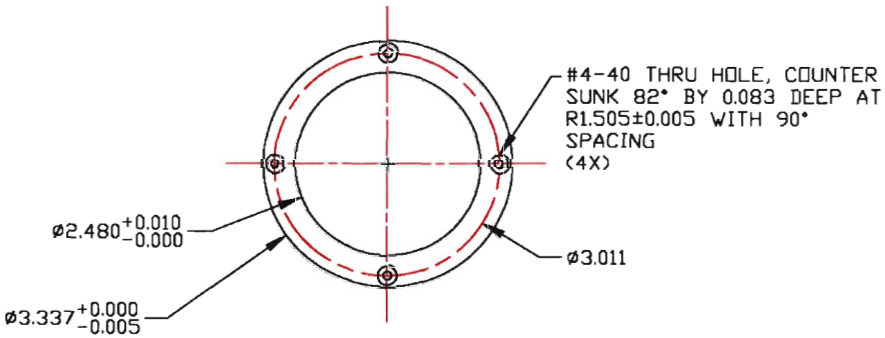

FILTER PACK WINDOW
FRONT

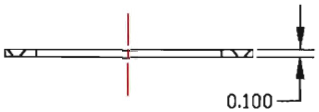

FILTER PACK WINDOW
BOTTOM

	DIMS ARE IN INCHES DECIMAL TOL ±0.005 ANGULAR TOL ±1°
REVISION 2	BREAK ALL EDGES
DATE 01/19/04	MATERIAL: AL 6061-T6
	SCALE 2.00
DWG No 2	DETAIL FILTER PACK WINDOW

DEVIATIONS FROM INTENDED SHAPE (FLATNESS, ROUNDNESS, ECT.) MUST BE WITHIN STATED DIMENSIONAL TOLERANCES PER ANSI Y14.5M-1982

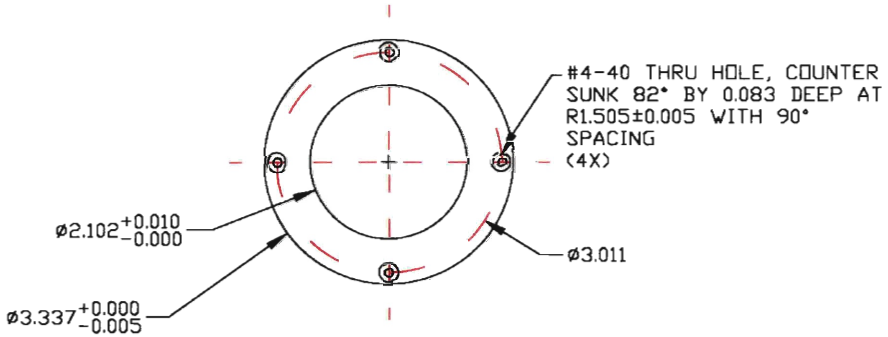

FILTER PACK WINDOW
FRONT

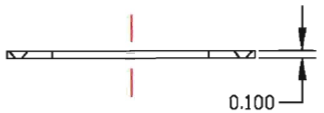

FILTER PACK WINDOW
BOTTOM

	DIMS ARE IN INCHES DECIMAL TOL ±0.005 ANGULAR TOL ±1°
REVISION 1	BREAK ALL EDGES
DATE 03/23/04	MATERIAL: AL 6061-T6
	SCALE 2.00
DWG No 2b	DETAIL FILTER PACK WINDOW 60 mm

DEVIATIONS FROM INTENDED SHAPE (FLATNESS, ROUNDNESS, ECT.) MUST BE WITHIN STATED DIMENSIONAL TOLERANCES PER ANSI Y14.5M-1982

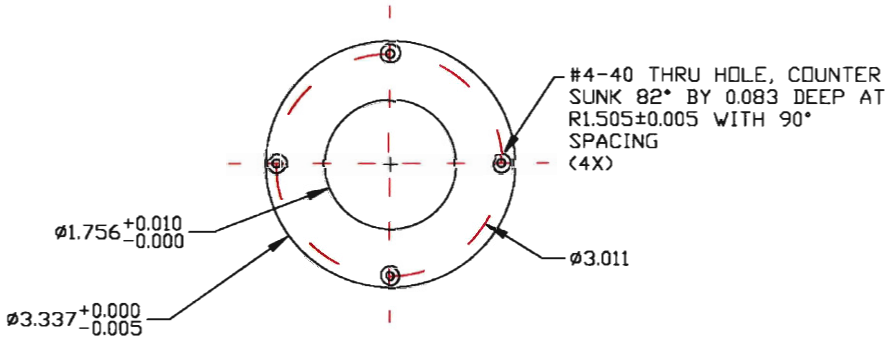

FILTER PACK WINDOW
FRONT

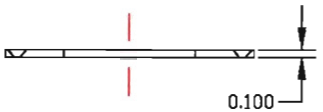

FILTER PACK WINDOW
BOTTOM

	DIMS ARE IN INCHES DECIMAL TOL ±0.005 ANGULAR TOL ±1°
REVISION 1	BREAK ALL EDGES
DATE 03/23/04	MATERIAL: AL 6061-T6
	SCALE 2.00
DWG No 2c	DETAIL FILTER PACK WINDOW 50 mm

DEVIATIONS FROM INTENDED SHAPE (FLATNESS, ROUNDNESS, ECT.) MUST BE WITHIN STATED DIMENSIONAL TOLERANCES PER ANSI Y14.5M-1982

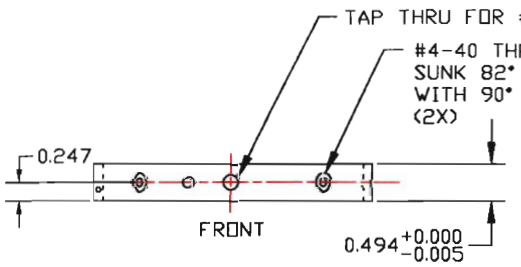

FILTER PACK COVER
TOP

NOTE:
TO BE MACHINED FROM STOCK PROVIDED

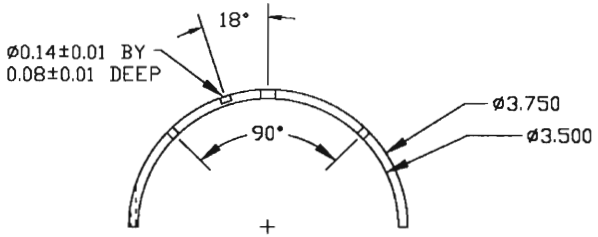

FILTER PACK COVER
FRONT

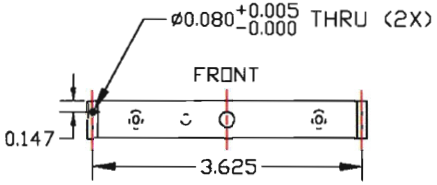

FILTER PACK COVER
BOTTOM

	DIMS ARE IN INCHES DECIMAL TOL ±0.005 ANGULAR TOL ±1°
REVISION 2	BREAK ALL EDGES
DATE 01/22/04	MATERIAL: AL 6061-T6
	SCALE 2.00
DWG No 3a	DETAIL FILTER PACK COVER

DEVIATIONS FROM INTENDED SHAPE (FLATNESS, ROUNDNESS, ECT.) MUST BE WITHIN STATED DIMENSIONAL TOLERANCES PER ANSI Y14.5M-1982

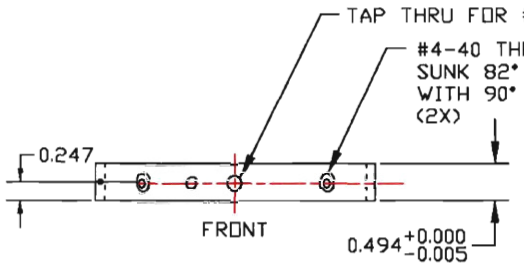

FILTER PACK COVER
TOP

NOTE:
TO BE MACHINED FROM STOCK PROVIDED

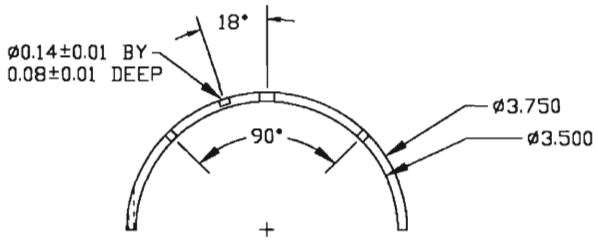

FILTER PACK COVER
FRONT

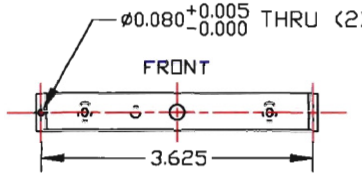

FILTER PACK COVER
BOTTOM

	DIMS ARE IN INCHES DECIMAL TOL ±0.005 ANGULAR TOL ±1°
REVISION 2	BREAK ALL EDGES
DATE 01/22/04	MATERIAL: AL 6061-T6
	SCALE 2.00
DWG No 3b	DETAIL FILTER PACK COVER

DEVIATIONS FROM INTENDED SHAPE (FLATNESS, ROUNDNESS, ECT.) MUST BE WITHIN STATED DIMENSIONAL TOLERANCES PER ANSI Y14.5M-1982

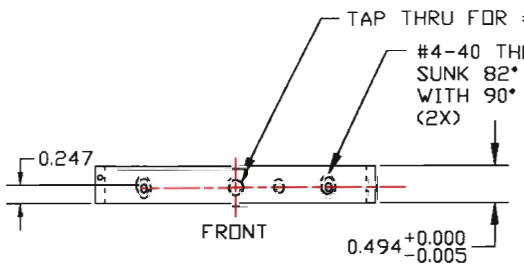

FILTER PACK COVER
TOP

NOTE:
TO BE MACHINED FROM STOCK PROVIDED

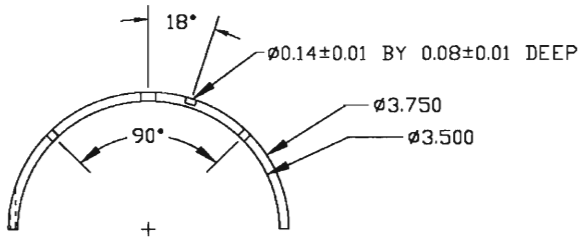

FILTER PACK COVER
FRONT

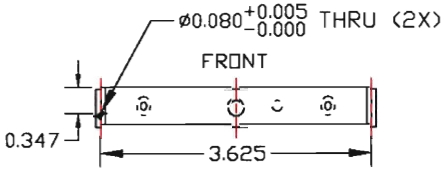

FILTER PACK COVER
BOTTOM

	DIMS ARE IN INCHES DECIMAL TOL ±0.005 ANGULAR TOL ±1°
REVISION 2	BREAK ALL EDGES
DATE 01/22/04	MATERIAL: AL 6061-T6
	SCALE 2.00
DWG No 3c	DETAIL FILTER PACK COVER

DEVIATIONS FROM INTENDED SHAPE (FLATNESS, ROUNDNESS, ECT.) MUST BE WITHIN STATED DIMENSIONAL TOLERANCES PER ANSI Y14.5M-1982

NOTE:
TO BE MACHINED FROM
STOCK PROVIDED

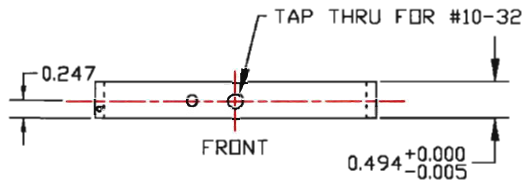

FILTER PACK COVER
TOP

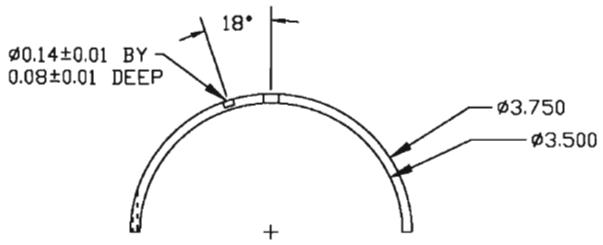

FILTER PACK COVER
FRONT

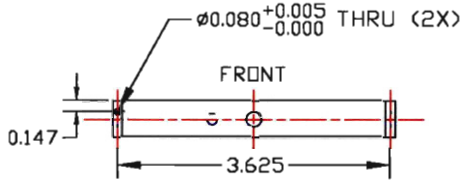

FILTER PACK COVER
BOTTOM

	DIMS ARE IN INCHES DECIMAL TOL ±0.005 ANGULAR TOL ±1°
REVISION 2	BREAK ALL EDGES
DATE 01/22/04	MATERIAL: AL 6061-T6
	SCALE 2.00
DWG No 4a	DETAIL FILTER PACK COVER

DEVIATIONS FROM INTENDED SHAPE (FLATNESS, ROUNDNESS, ECT.) MUST BE WITHIN STATED DIMENSIONAL TOLERANCES PER ANSI Y14.5M-1982

NOTE:
TO BE MACHINED FROM
STOCK PROVIDED

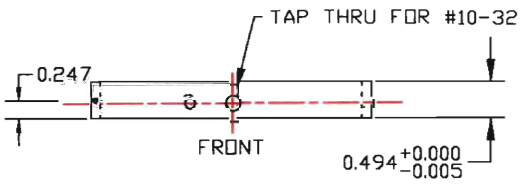

FILTER PACK COVER
TOP

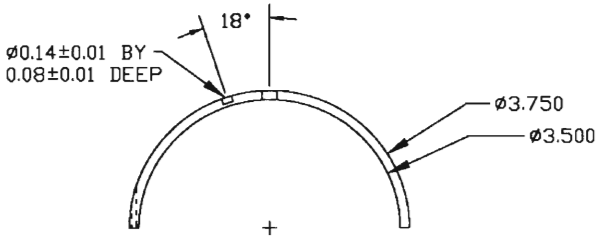

FILTER PACK COVER
FRONT

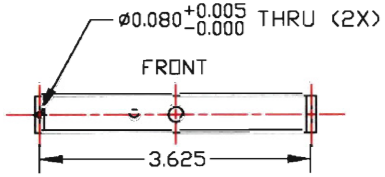

FILTER PACK COVER
BOTTOM

	DIMS ARE IN INCHES DECIMAL TOL ±0.005 ANGULAR TOL ±1°
REVISION 2	BREAK ALL EDGES
DATE 01/22/04	MATERIAL: AL 6061-T6 SCALE 2.00
DWG No 4b	DETAIL FILTER PACK COVER

DEVIATIONS FROM INTENDED SHAPE (FLATNESS, ROUNDNESS, ECT.) MUST BE WITHIN STATED DIMENSIONAL TOLERANCES PER ANSI Y14.5M-1982

NOTE:
TO BE MACHINED FROM
STOCK PROVIDED

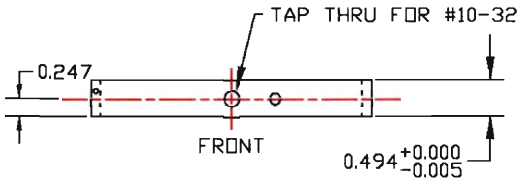

FILTER PACK COVER
TOP

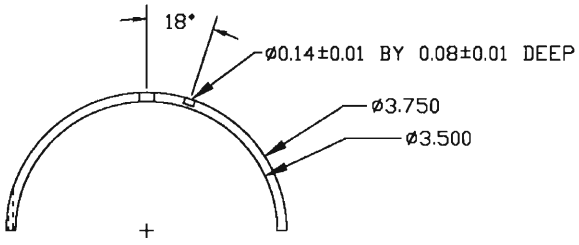

FILTER PACK COVER
FRONT

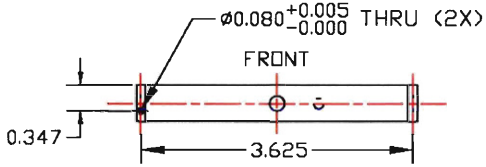

FILTER PACK COVER
BOTTOM

	DIMS ARE IN INCHES DECIMAL TOL ±0.005 ANGULAR TOL ±1°
REVISION 2	BREAK ALL EDGES
DATE 01/22/04	MATERIAL: AL 6061-T6
	SCALE 2.00
DWG No 4c	DETAIL FILTER PACK COVER

DEVIATIONS FROM INTENDED SHAPE (FLATNESS, ROUNDNESS, ECT.) MUST BE WITHIN STATED DIMENSIONAL TOLERANCES PER ANSI Y14.5M-1982

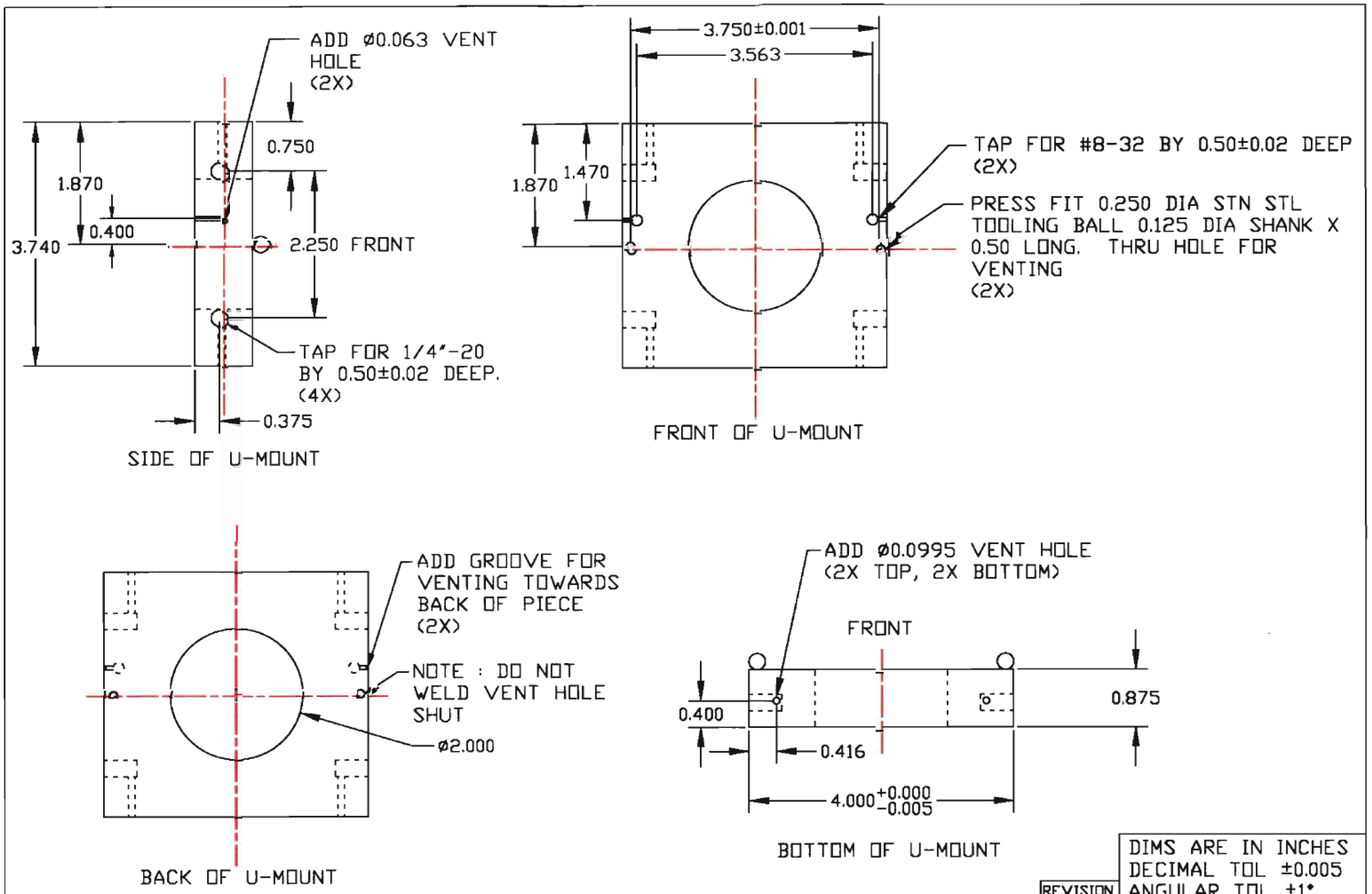

ITEM	QTY	PART NO.	DESCRIPTION	NOTES
2	2	TCB-26706	ø1/4 X 1/8 LG TOOLING BALL	REID

DEVIATIONS FROM INTENDED SHAPE (FLATNESS, ROUNDNESS, ECT.) MUST BE WITHIN STATED DIMENSIONAL TOLERANCES PER ANSI Y14.5M-1982

REVISION	2
DATE	01/26/04
DWG No	5

DIMS ARE IN INCHES
DECIMAL TOL ±0.005
ANGULAR TOL ±1°
BREAK ALL EDGES
MATERIAL: AL 6061-T6
SCALE 2.00
DETAIL
UNIMOUNT

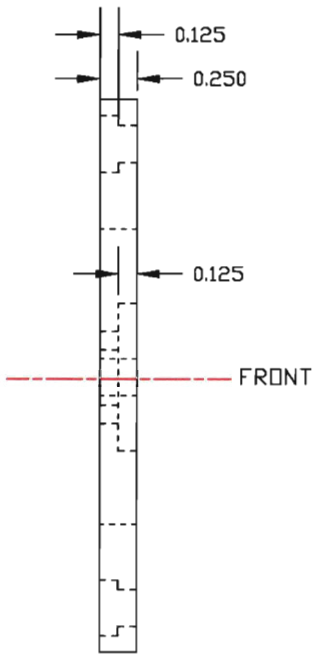

SIDE OF X-ADAPTER
SCALE 1:1

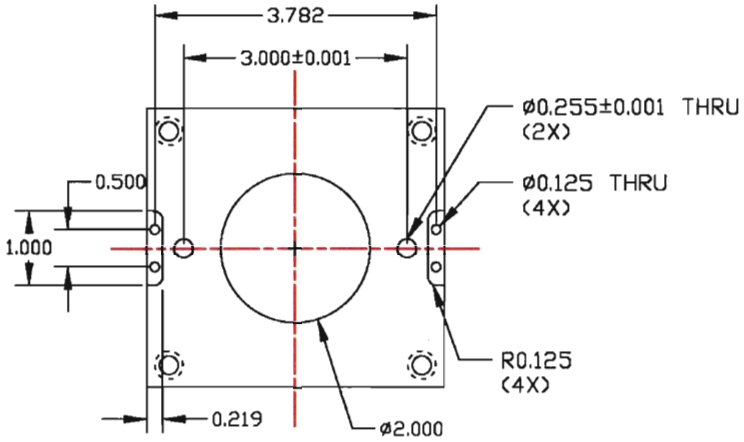

FRONT OF X-ADAPTER

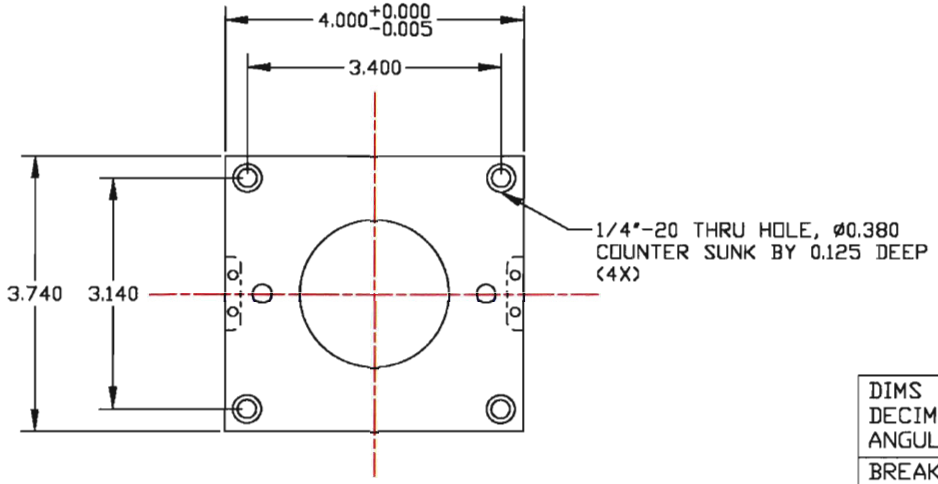

BACK OF X-ADAPTER

	DIMS ARE IN INCHES DECIMAL TOL ±0.005 ANGULAR TOL ±1°
	BREAK ALL EDGES
DATE 01/05/04	MATERIAL: ALUMINUM
	SCALE 2.00
DWG No 6	DETAIL X-ADAPTER

DEVIATIONS FROM INTENDED SHAPE (FLATNESS, ROUNDNESS, ECT.) MUST BE WITHIN STATED DIMENSIONAL TOLERANCES PER ANSI Y14.5M-1982

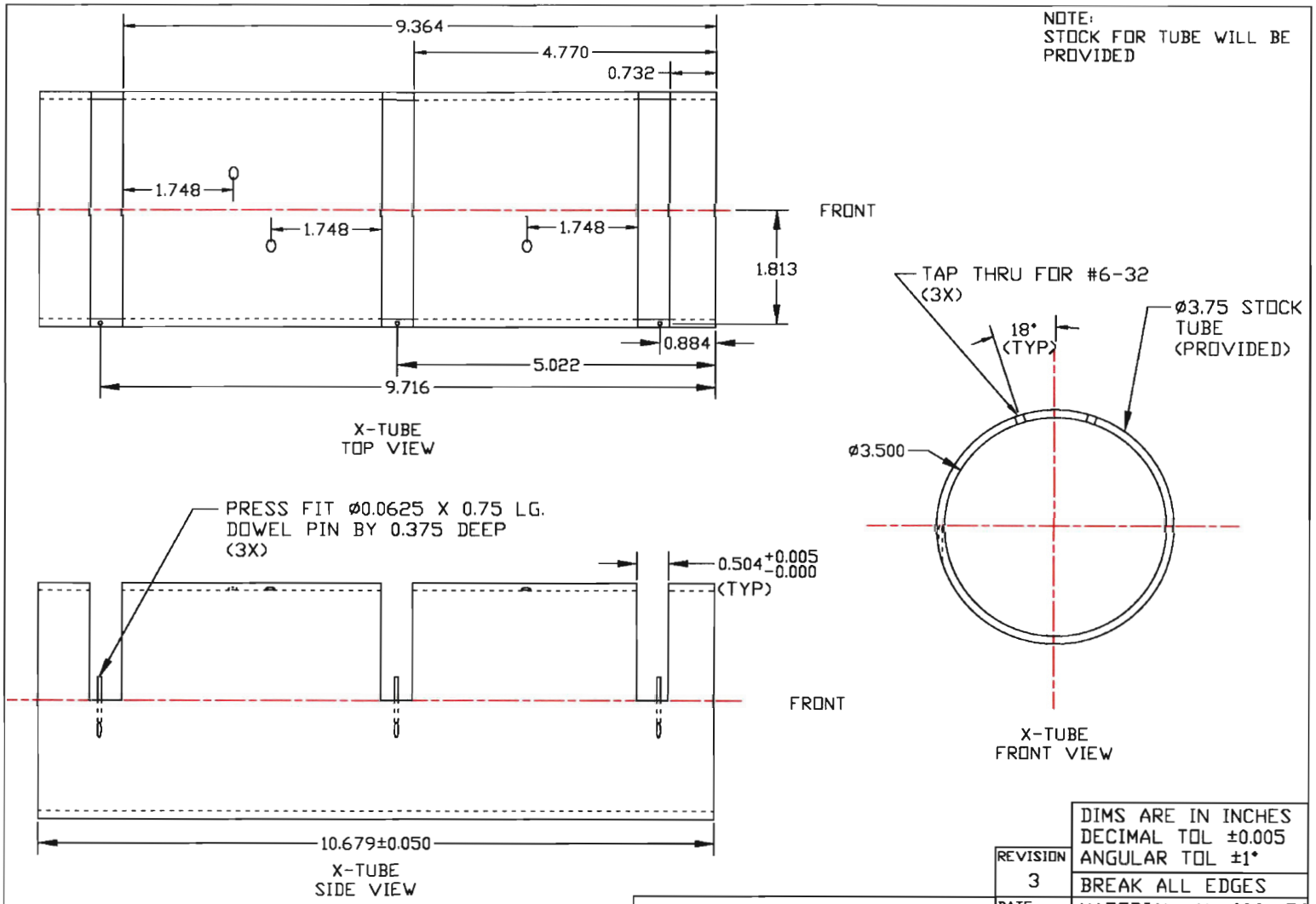

ITEM	QTY	PART NO.	DESCRIPTION	NOTES
3	3	98381A422	Ø.0625 X .75 LG DOWEL PIN	McMASTER

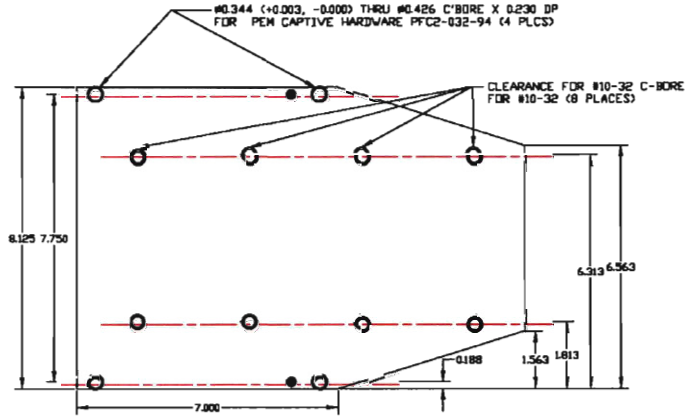

TOP VIEW

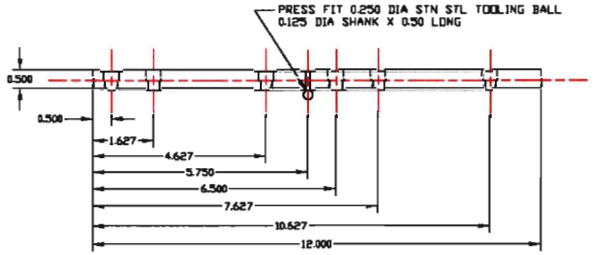

SIDE VIEW

1	2	TCB-26706	TOOLING BALLS	REID	DEVIATIONS FROM INTENDED SHAPE (FLATNESS, ROUNDNESS, ECT.) MUST BE WITHIN STATED DIMENSIONAL TOLERANCES PER ANSI Y14.5M-1982	REVISION 1
ITEM	QTY	PART NO.	DESCRIPTION	NOTES		DATE 02/14/03
						DWG No 8

DIMS ARE IN INCHES
DECIMAL TOL ±0.005
ANGULAR TOL ±1°
BREAK ALL EDGES
MATERIAL: 6061-T6 AL
SCALE: NA
DETAIL
WASHBOARD

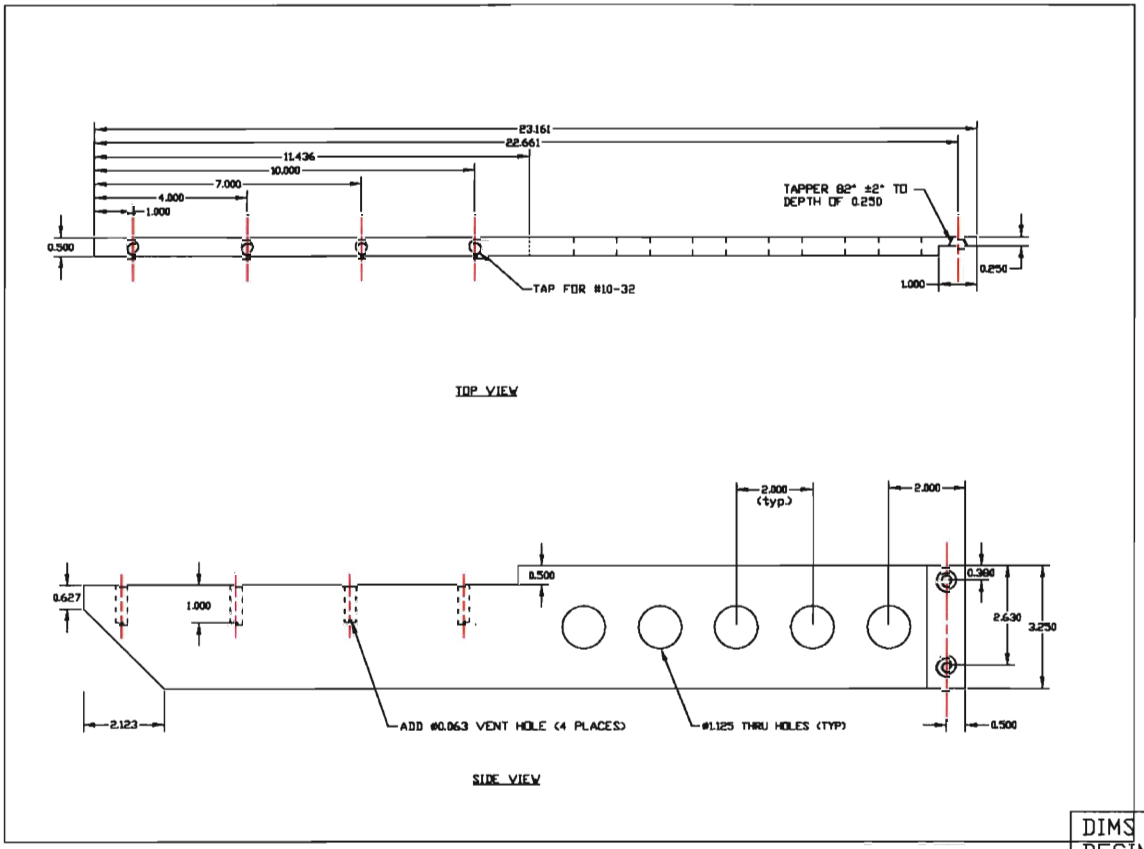

	DIMS ARE IN INCHES
	DECIMAL TOL ±0.005
REVISION 1	ANGULAR TOL ±1°
	BREAK ALL EDGES
DATE 02/14/03	MATERIAL: 6061-T6 AL
	SCALE: NA
DWG No 9	DETAIL RIGHT SUPPORT

DEVIATIONS FROM INTENDED SHAPE (FLATNESS, ROUNDNESS, ECT.) MUST BE WITHIN STATED DIMENSIONAL TOLERANCES PER ANSI Y14.5M-1982

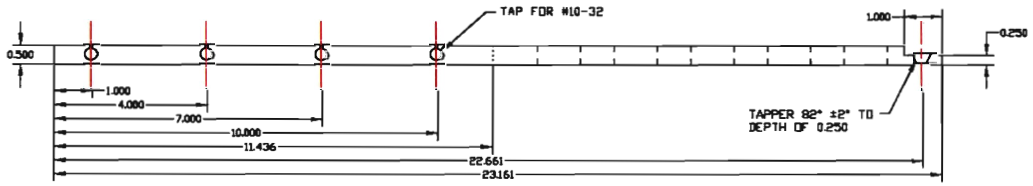

TOP VIEW

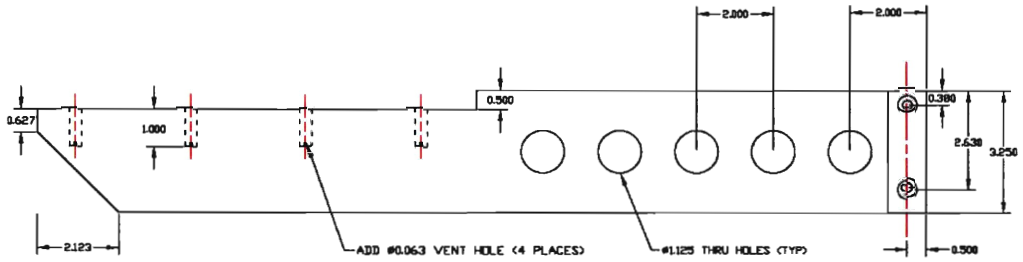

SIDE VIEW

	DIMS ARE IN INCHES DECIMAL TOL ±0.005 ANGULAR TOL ±1°
REVISION 1	BREAK ALL EDGES
DATE 02/14/03	MATERIAL: 6061-T6 AL
	SCALE: NA
DWG No 10	DETAIL LEFT SUPPORT

DEVIATIONS FROM INTENDED SHAPE (FLATNESS, ROUNDNESS, ECT.) MUST BE WITHIN STATED DIMENSIONAL TOLERANCES PER ANSI Y14.5M-1982

Bibliography

1. J. D. Lindl, *Inertial Confinement Fusion: The Quest for Ignition and Energy Gain Using Indirect Drive* (Springer-Verlag, New York, 1998).
2. S. Atzeni and J. Meyer-Ter-Vehn (2004). The Physics of Inertial Fusion. New York, NY: Oxford University Press Inc.
3. J. L. DeCiantis *et al.*, (submitted to Rev. Sci. Instrum.).
4. J. L. DeCiantis *et al.*, (submitted to Phys. Plasmas).
5. C. K. Li, F. H. Séguin, J. A. Frenje *et al.*, Phys. Rev. Lett. **89**, 165002 (2002).
6. B. E. Schwartz, MS Thesis, Massachusetts Institute of Technology (2004).
7. C. K. Li, F. H. Séguin, D. G. Hicks *et al.*, Phys. Plasmas **8** 4902 (2001).
8. F. H. Séguin, C. K. Li, J. A. Frenje *et al.*, Phys. Plasmas **9**, 3558 (2002).
9. F. H. Séguin, J. A. Frenje, C. K. Li *et al.*, Rev. Sci. Instrum. **74**, 975 (2003).
10. C. R. Christensen, D. C. Wilson, C. W. Barnes *et al.*, Phys. Plasmas **11**, 2771 (2004).
11. L. Disdier, R. A. Lerche, J. L. Bourgade *et al.*, Rev, Sci. Instrum. **75**, 2134 (2004).
12. J. A. Frenje, C. K. Li, F. H. Séguin *et al.*, Rev. Sci. Instrum. **73**, 2597 (2002).
13. F. H. Séguin *et al.*, (to be submitted to Phys. Plasmas).